Molecular imaging of inflammation in atherosclerosis: Preclinical study in Apolipoprotein E-Deficient mice and preliminary evaluation in human using positron emission tomography

Molekulare Bildgebung inflammatorischer Prozesse bei Atherosklerose: Präklinische Studie in Apolipoprotein-E Knockout-Mäusen sowie erste Evaluation humaner PET-Studien.

Doctoral thesis for a doctoral degree
at the Graduate School of Life Sciences,
Julius-Maximilians-Universität Würzburg,
Section Biomedicine

submitted by

Xiang Li
From China

Würzburg, 2014

Submitted on: ……

Members of the *Promotionskomitee*:

Chairperson:

Primary Supervisor: Prof. Dr.Dr. Wolfgang Bauer

Supervisor (Second): Prof. Dr. Samuel Samnick

Supervisor (Third): Prof. Dr. Peter Jakob

Date of Public Defence: ……

Date of Receipt of Certificates: ……..

Table of contents

1. SUMMARY

Motivation and Aim:

Cardiovascular disease has been the leading cause of mortality and morbidity throughout the world. In developed countries, cardiovascular diseases are already responsible for a majority of deaths and will become the pre-eminent health problem worldwide (1,2). Rupture of atherosclerotic plaque accounts for approximately 70% of fatal acute myocardial infarction and sudden heart deaths. Conventional criterias for the diagnosis of “vulnerable plaques” are calcified nodules, yellow appearance of plaque, a thin cap, a large lipid core, severe luminal stenosis, intraplaque hemorrhage, inflammation, thrombogenicity, and plaque injury (3-5).

Noninvasive diagnosis of vulnerable plaque still remains a great challenge and a huge research prospect, which triggered us to investigate the feasibility of PET imaging on the evaluation of atherosclerosis. Nuclear imaging of atherosclerosis， especially co-registered imaging modalities, could provide a promising diagnostic tool including both anatomy and activities to identify vulnerable atherosclerotic plaque or early detection of inflammatory endothelium at risk. Furthermore, the development of specific imaging tracers for clinical applications is also a challenging task. The aim of this work was to assess the potential of novel PET imaging probes associated with intra-plaque inflammation on animal models and in human respectively.

Methods

In this work, several molecular imaging modalities were employed for evaluation of atherosclerosis. They included Positron emission tomography / Computed tomography (PET/CT) for human studies, and micro-PET, autoradiography and high-resolution magnetic resonance imaging (MRI) for animal studies. Radiotracers for PET imaging included the glucose analogue ^{18}F-Fluorodeoxyglucose (^{18}F-FDG), the somatostatin receptor avide tracer ^{68}Ga-DOTATATE, and the Gallium-68 labeled fucoidan (^{68}Ga-Fucoidan), which was developed as a PET tracer to detect endothelial P-selectin, which overexpressed at early stage of atherosclerosis and endothelial overlying activated plaque. Tracer’s capabilities were firstly assessed on cellular level in vitro. Subsequently, Animal studies were conducted in two animal models: 1, Apolipoprotein E (ApoE-/-) mice having severe atherosclerotic plaque; 2, Lipopolysaccharide (LPS) -induced mice for receiving acute vascular inflammation.

Corresponding analyses on protein and histological level were conducted as well to confirm our results.

In human study, 16 patients with neuroendocrine tumors (NETs) were investigated on imaging vascular inflammation. These patients had undergone both ^{68}Ga-DOTATATE PET/CT and ^{18}F-FDG PET/CT for staging or restaging within 6 weeks. 16 patients were randomized into two groups: high-risk group and low-risk group. Uptake ratio of both tracers from two groups were compared and correlated with common cardiovascular risk factors.

Results and Conclusion

In murine study, the expression of somatostatin receptor 2, which is the main bio-target of ^{68}Ga-DOTATATE on macrophage/monocyte was confirmed by flow cytometry and immunohistochemistry. Prospectively, high specific accumulation of ^{68}Ga-DOTATATE to the macrophage within the plaques was observed in aorta lesions by autoradiography and by micro-PET. In study with ^{68}Ga-fucoidan, a strong expression of P-selectin on active endothelium overlying on inflamed plaque but weaker on inactive plaques was confirmed. Specific focal uptake of ^{68}Ga-fucoidan were detected at aorta segments by micro-PET, and correlated with high-resolution magnetic resonance imaging (MRI), which was used to characterize the morphology of plaques. ^{68}Ga-fucoidan also showed a greater affinity to active inflamed plaque in comparison of inactive fibrous plaque, which was assessed by autoradiography. Specificity of ^{68}Ga-DOTATATE and ^{68}Ga-fucoidan were confirmed by ex-vivo blocking autoradiography and in vivo blocking PET imaging respectively.

In human study, focal uptake of both ^{18}F-FDG and ^{68}Ga-DOTATATE was detected. Analyzing concordance of two tracers' uptake ratio, Out of the 37 sites with highest focal ^{68}Ga-DOTATATE uptake, 16 (43.2%) also had focal ^{18}F-FDG uptake. Of 39 sites with highest ^{18}F-FDG uptake, only 11 (28.2%) had a colocalized ^{68}Ga-DOTATATE accumulation. Correlated tracers' uptake and calcium burden and risk factors, Mean target-to-background ratio (TBR) of ^{68}Ga-DOTATATE correlated significantly with the presence of calcified plaques ($r=0.52$), hypertension ($r=0.60$), age ($r=0.56$) and uptake of ^{18}F-FDG ($r=0.64$). TBRmean of ^{18}F-FDG correlated significantly only with hypertension ($r=0.58$; $p<0.05$). Additionally, TBRmean of ^{68}Ga-DOTATATE is significant higher in the high risk group while TBRmean of ^{18}F-FDG is not.

In conclusion, we evaluated vascular inflammation of atherosclerosis non-invasively using the two PET tracers: ^{68}Ga-DOTATATE and ^{68}Ga-Fucoidan. ^{68}Ga-DOTATATE show specific affinity to infiltrated macrophage within the plaques. ^{68}Ga-Fucoidan may hold the potential to discriminate between active and inactive atherosclerotic plaques in terms of variant accumulation on different-types of plaques. PET as leading molecular imaging technique

provides superiority in assessing cellular activity, which is pivotal for understanding internal activity of atherosclerotic plaques. Since diagnosis of atherosclerosis is a complex and multi-dimensional task. More integrated imaging technology such as PET/MRI, faster imaging algorithm, more efficient radiotracer are required for further development of atherosclerosis imaging,

ZUSAMMENFASSUNG

Ziel:

Kardiovaskuläre Erkrankungen stellen die häufigste Todesursache der westlichen Industrieländer dar und führen zu einem zunehmenden Gesundheitsproblem weltweit. (1,2). Ca. 70 % aller akuten Myocardinfarkte sind auf die Ruptur atherosklerotischer Plaques zurück zuführen, deren typische Charakteristika ein kalzifizierter, lipidhaltiger Kern, überzogen von einer dünnen fibrösen Kappe, darstellt. Innerhalb der atherosklerotischer Plaques kommt es zu Makrophageneinlagerung und im weiteren Verlauf zu entzündlichen und angiogentischen Prozesse, die zu Einblutungen führen und die Instabilität der Plaques zur Folge hat (3-5). Die nichtinvasive Diagnostik rupturgefährdeter Plaques stellt immer noch eine große medizinische Herausforderung dar. Die nuklearmedizinische Bildgebung, kombiniert mit MRT/CT zur anatomischen Co-Registrierung, könnte eine verbesserte diagnostische Methode zur Darstellung rupturgefährdeter atherosklerotischen Plaques und frühzeitiger entzündlicher Prozesse darstellen. Ziel dieser Arbeit war es daher, atherosklerosische Plaques mittels Positronenemissionstomografie (PET) unter Verwendung neuer PET Tracer für die Darstellung von Entzündungsprozesse im Tiermodell und der humanen Anwendung zu untersuchen.

Material und Methoden:

Im Rahmen dieser Arbeit kamen verschiedene bildgebende Verfahren zur Anwendung. Im Einzelnen waren dies PET/CT bei humanen Studien sowie micro-PET, Autoradiografie und hochauflösende Magnetresonanztomografie (MRT) bei Untersuchungen im Tiermodell. Als PET-Tracer wurden das Glukosederivat ^{18}F-Flurodesoxyglukose (^{18}F-FDG), ^{68}Ga-DOTATATE, das an Somatostatin-Rezeptoren bindet sowie Gallium-68 markiertes Fucoidan (^{68}Ga-Fucoidan) verwendet. Bei ^{68}Ga-Fucoidan handelt es sich um einen neu entwickelten PET-Tracer zur Darstellung von P-Selectin, welches an aktivieren Plaques im frühen Stadium der Atherosklerose überexprimiert wird. Die Untersuchungen im Tiermodell fanden sowohl an Apolipoprotein E Knockout-Mäusen (ApoE-/-) als auch an Lipopolysaccharid- (LPS) induzierten Mäusen statt. Des Weiteren wurden uptake-Untersuchungen auf in Zellkulturexperimenten durchgeführt. Zur Bestätigung der der Untersuchungsergebnisse wurden zusätzlich histochemische Untersuchungen durchgeführt. Im Rahmen der humanen Studien wurden 16 Patienten mit neuroendokrinenen Tumoren (NET) hinsichtlich vaskulärer Entzündungsprozesse untersucht. Alle Patienten erhielten ein ^{68}Ga-DOTATATE PET/CT und 18F-FDG PET/CT zum Staging bzw. Restaging innerhalb von 6 Wochen. Die Einteilung der Patienten erfolgte in zwei Gruppen: hohes Risiko und geringes Risiko. Die uptake-Verhältnisse

beider Tracer in beiden Gruppen wurden mit einander verglichen und hinsichtlich bekannter cardiocaskulärer Risikofaktoren in Beziehung gesetzt.

Ergebnisse und Zusammenfassung:

Die Expression der Somatostatin-Rezeptor Subtyps 2, an den ^{68}Ga-DOTATATE an Makrophagen/Monocyten bindet, konnte mittels flow cytometrischer und immunhistochemischer Experimente im Mausmodell bestätigt werden. Mit Hilfe von micro-PET Untersuchungen und Autoradiografie wurde eine hohe spezifische Anreicherung von ^{68}Ga-DOTATATE an Makrophagen innerhalb der Plaques beobachtet.Im Rahmen der Untersuchungen mit ^{68}Ga-Fucoidan konnte eine hohe P-Selectin-Expression an aktiviertem Endothelium, welches die entzündlichen Plaques überlagert festgestellt werden. Bei inaktiven Plaques hingegen zeigte sich eine geringe P-Selectin-Expression. In micro-PET-Studien konnte ein spezifischer fokaler uptake von ^{68}Ga-Fucoidan in der Aorta nachgewiesen werden. Dieser korrelierte mit den zusätzlich durchgeführten MRT-Untersuchungen zur Charakterisierung der Plaquemorphologie. Mittels Autoradiografie konnte nachgewiesen werden, dass ^{68}Ga-Fucoidan eine höhere Affinität zu aktivierten entzündlichen Plaques im Vergleich zu inaktivieren fibrösen Plaques zeigt. Die spezifische Bindung von ^{68}Ga-DOTATATE und ^{68}Ga-Fucoidan wurde über Blockadeexperimente mittels Autoradiografie und PET bestätigt. In der humanen Anwendung wurde ein fokaler uptake von ^{18}F-FDG und ^{68}Ga-DOTATATE detektiert. Die Analyse der Übereinstimmung des uptakes beider Tracer ergab: Von 37 spots mit hohem ^{68}Ga-DOTATATE-uptake zeigten 16 (43,2 %) ebenfalls einen fokalen ^{18}F-FDG -uptake. Von 39 spots mit hohem ^{18}F-FDG -uptake zeigten nur 11(28,2%) eine ^{68}Ga-DOTATATE-Anreicherung. Betrachtet man den Tracer-uptake hinsichtlich des Calcium-burden und weiterer Risikofakoren, so ergeben sich folgende Korrelationskoeffizienten: TBRmean of ^{68}Ga-DOTATATE korreliert signifikant mit der Anwesenheit von kalzifizierten Plaques (r=0,52), Blutdruck (r=0,60), Alter (r=0,56) und ^{18}F-FDG uptake (r=0,64). Eine signifikante Korrelation von TBRmean ^{18}F-FDG konnte lediglich beim Risikofaktor Blutdruck (r=0,58, $p<0,05$) festgestellt werden. Weiterhin zeigte sich, dass der TBRmean von Ga-DOTATATE in der Hoch-Risiko-Gruppe signifikant höher, dies gilt jedoch nicht für TBRmean ^{18}F-FDG.

Zusammenfassung:

In dieser Arbeit wurden die vaskulären Entzündungsprozessen der Atherosklerose mittels der nichtinvasiven PET unter Verwendung von ^{68}Ga-DOTATATE und ^{68}Ga-Fucoidan untersucht und bewertet. ^{68}Ga-DOTATATE zeigte eine spezifische Affinität zu Makrophagen innerhalb der atherosklerotischen Plaques. Mit ^{68}Ga-Fucoidan konnt zwischen aktiven und inaktiven Plaques unterschieden werden.

Die molekulare Bildgebung mittels PET eignet sich hervorragend zur Darstellung und Untersuchung molekularer Prozesse innerhalb atheroskerotischer Plaques. Dennoch sind weiterführende Technologien wie PET/MR, schnellere Algorithmen, hoch spezifische Radiotracer zur Weiterentwicklung der PET-Bildgebung atherosklerotischer Plaques notwendig.

2. INTRODUCTION

Atherosclerosis is a continuously progressive disease. Atherosclerotic lesions are asymmetric thickenings of the inner layer of artery, the intima proliferation. Inflammatory cells constitute a pivotal part of atherosclerosis. The atherosclerotic lesions (plaques) principally occur in large and medium-sized arteries and are able to cause ischemia of the heart or brain (6-9).

2.1 Inflammatory features of atherosclerosis

Inflammation is increasingly recognized as the major pathogenic link between clinical cardiovascular risk factors and acute plaque events. Leukocyte subsets accumulate in atherosclerotic lesions at various stages and participate pathological alternation during formation of atherosclerosis.

2.1.1 Activation of early endothelial inflammatory processes

A large number of pathophysiologic founding on formation atherosclerosis suggested that endothelial dysfunction was the first step in atherosclerosis (10,11).

After activation of vascular endothelium, an increased plasma concentration of inflammatory mediators is characteristic of inflammatory processes during the formation of atherosclerosis. The activation can lead to up-regulation of adhesion molecules, such as intracellular adhesion molecule-1 (ICAM-1), vascular cell adhesion molecule-1 (VCAM-1), integrins, and selectins (L, E, and P) will lead to the rolling and adhesion of immune cells (monocytes, macrophages, platelets, and T lymphocytes) onto the endothelial wall. This activation of the endothelium leads to the release of pro-inflammatory cytokines, surface receptors, and proteinase enzymes including Tumor necrosis factors (TNF-α), interleukins, interferons, monocyte chemoattractant protein-1 (MCP-1) (3,12-14) (Fig.1).

2.1.2 Mechanisms of leukocyte

Previous studies have established that, once adherent to the endothelium, leukocytes subsequently enter the intima by diapedesis between endothelium at their gaps. This

phenomenon of directed migration of leukocytes through the endothelium has yielded to molecular analysis. Investigators have defined families of chemoattractant cytokines (chemokines) capable of recruiting leukocytes into the arterial intima. Such as MCP-1, which overexpressed in atheroma (15) (Fig.1).

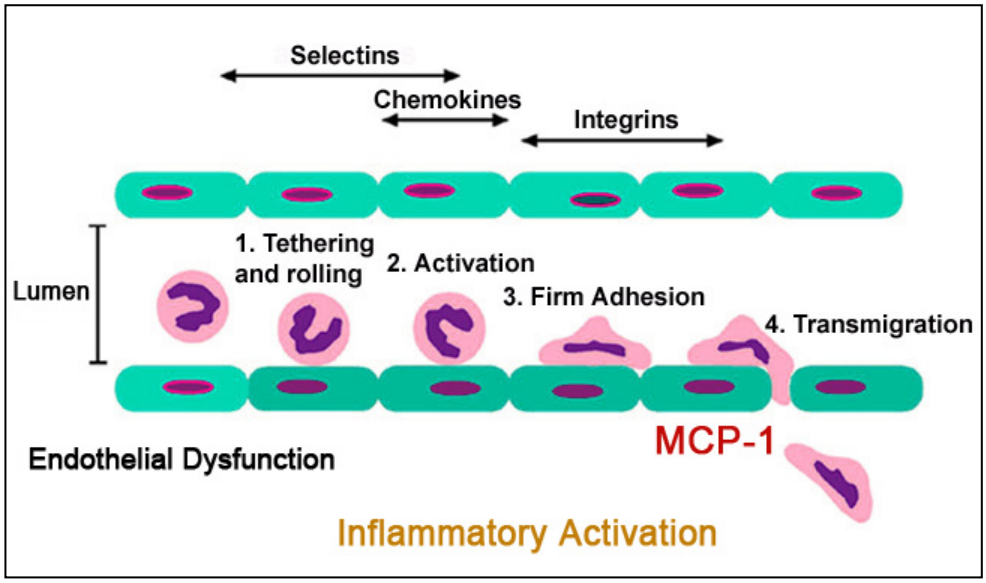

Figure 1: The endothelial dysfunction cascade after inflammatory activation at early atherosclerosis. Interactions between leukocytes and endothelium. Leukocyte - endothelial cell contacts are initiated by selectin-dependent tethering and rolling, followed by chemokine-mediated activation, firm adhesion and spreading by integrin, finally, extravasation into the subendothelial space.

Once resident in the arterial intima, monocytes differentiate to the macrophages morphologically, undergoing a series of changes subsequently lead to foam cell. The monocytes stimulated expression of scavenger receptors from modified lipoproteins such as the scavenger receptor A (SRA) and CD36, and internalize modified lipoproteins (16-19). These lipid-laden macrophages are known as foam cells, they characterize the early atherosclerotic lesion, so called “fatty streak”, which present commonly in infants (20,21).

2.1.3 Inflammation in atherosclerosis progression and complication

After formation of fatty streak, the initial atheroma normally evolves into a more advanced lesion, which can eventually cause severe clinical manifestations. During the progression, fatty streaks evolve into advanced atheroma through proliferation of smooth muscle cells, which accumulate in the atherosclerotic plaques and secrete extracellular matrix (22,23). Growth factors laid out by macrophages in the atherosclerotic plaque stimulated the smooth muscle

replication, involved in lesion growth. Following progressing of more complicated atheroma, the arterial lumen is continued narrowing until it hinders blood flow and cause clinical manifestations.

2.1.4 Inflammation associates plaque disruption

Current evidence demonstrates that disruption of plaques trigger thrombosis, which can cause expansion of atheroma. And inflammation is able to trigger various forms of plaque disruption. The main type of physical disruption and most common mechanism of plaque disruptions is the fracture of plaques' fibrous cap. The inflammation contributes to the fracture of plaques' fibrous cap. Since invasive coagulation factors in main pro-thrombotic stimulator, the function of fibrous cap is to insulate lipid-rich core of the plaque from bloodstream containing coagulation proteins. And gap from ruptured fibrous cap allows the coagulation proteins contact with lipid core, which lead to plaque disruption.

Additionally, there are two other forms of plaques disruption, superficial erosion of atherosclerotic plaques and disruption of the micro-vessels.

In superficial erosion of plaques, main two processes related to inflammation could cause endothelial desquamation. Firstly inflammatory mediators production or vascular injury from cytolysis by activated killer T cells lead to endothelial cell apoptosis. Moreover, oxidized lipoproteins are able to induce the expression of matrix metalloproteinases (MMPs), whose function is in degrading endothelial membrane. Therefore, activation of inflammation is able to induce the endothelial enzymes that degrade the extracellular matrix element leading promoted degradation of endothelium.

The inflammation is also related to formation of microvessel disruption. The plaque microvasculature contributes plaque lesion by two ways, promoting plaque growth and internal haemorrphage. The microvessel proceeding is similar to the formation of common angiogenesis. Apart from secreting growth factors for smooth muscle cells, inflammatory cells within the plaque, also produce antigenic mediators such as fibroblast growth factor and vascular endothelial growth factor (VEGF), which enhance atherosclerotic plaque progression (24-30).

Overall, as the understanding of the pathophysiology of lesion-instability is continuous developing, a coincident and normalized evaluation method regarding vulnerability is necessary. In histopathology, atherosclerosis is characterized by a progressive accumulation

of lipids, cells (smooth-muscle cells, macrophages, and T-lymphocytes) and extracellular matrix in the arterial wall (31). In the molecular level assessments, foam cells (lipid-laden macrophages) are seem to be the central role in the vicious circle of the atherosclerosis development; however, many other cells are involved in this process as well. Cell recruitment from the blood is followed by migration of cells such as T cells and massive other immune cells. On the vessel wall, smooth muscle cells are activated to a proliferative and secretory phenotype. A physiological cascade of signaling pathways such as endothelial activation, proliferation, angiogenesis, enzymatic reactions, and apoptosis causes evolution to the formation of an advanced atherosclerotic plaque.

2.2 Oxidative stress in plaque formation

Atherosclerosis is a continuously progressive disease visualized by the accumulation of cholesterol laden macrophages. It leads to a proliferation of endothelial and smooth muscle cells within the arterial wall. These early lesions in atherosclerosis called “fatty streak” (21,32,33). Fatty streaks are not clinically significant, but they are the precursors of more severe lesions advanced by the accumulation of lipid-rich necrotic debris (34). They are associated with an increased production of free species named reactive oxygen species (ROS) (35). Oxidative stress reflects increased production of ROS. Previous studies demonstrated that oxidative stress plays a pivotal role in the pathogenesis of atherosclerosis, especially vascular endothelial dysfunction (36,37); especially ROS is able to injure cell membranes, ROS trigger the formation of oxidized low-density lipoproteins (LDL), the main component of atherosclerotic plaque (38). The endothelium becomes more permeable to leucocytes and lipid molecules, subsequently leading increased macrophages uptaking oxidized LDL, then becoming foam cells. Foam cells in turn lead to an enhancement in inflammatory cytokine production (Fig. 2)

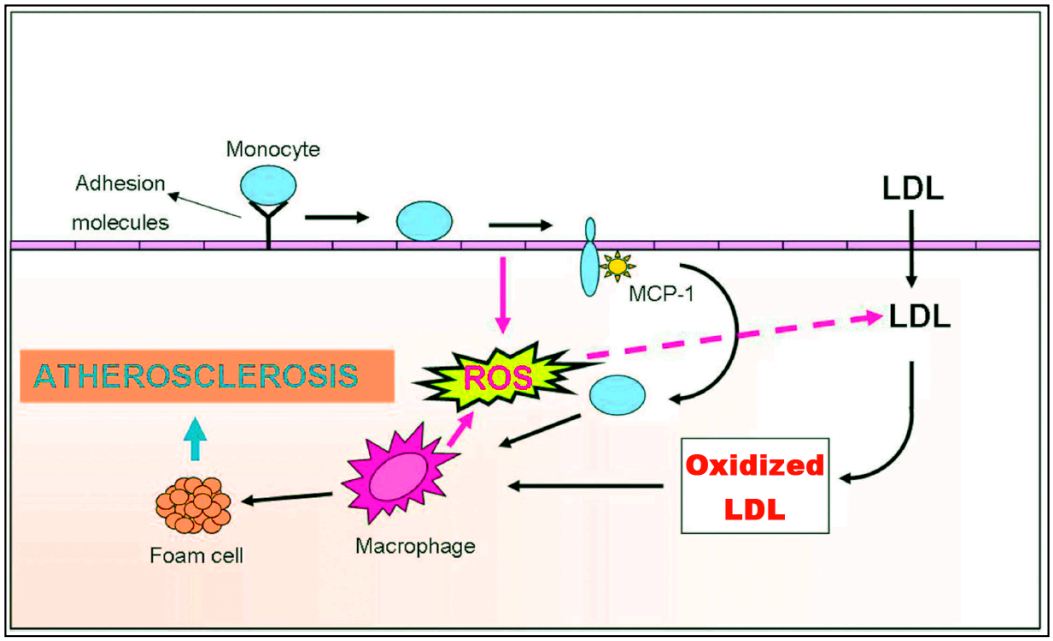

Figure 2: Oxidative stress in atherosclerosis. An increase of free radical production is associated with atherosclerosis progressing. It provoke an oxidative modification from low-density lipoprotein (LDL) to oxidized LDL. Circulating monocytes migrate to the injury site at attach to endothelium by adhesion molecules, and subsequently infiltrate into subendothelial space, which is stimulated by ox-LDL and under effect of Monocyte chemo attractant protein-1 (MCP-1). The ox-LDL can is taken up by macrophages, which become foam cells, leading to the formation of atherosclerotic plaque.

Overall, oxidative modifications on the arterial wall promote the development of atherosclerosis. Advanced atherosclerosis embodies itself morphologically as known as atherosclerotic plaques. Plaques contain a central lipid core developed from ox-LDL like macrophage, that is most often hypocellular and may even include cholesterol that have formed in the aftermath of necrotic foam cells. Macrophages accumulate and transform into necrotic cores characteristic of advanced, complicated lesions. Although Extension of plaque lesions can block blood flow, the most crucial clinical complication is an acute occlusion due to the formation of a thrombus, causing myocardial infarction if happen at coronary arteries, or stroke if happen at carotid arteries.

2.3 Molecular imaging in cardiovascular research

Molecular imaging (MI) is widely defined as the molecular characterization of biological processes in vivo. MI methods can visualize, characterize, and measure the biological progresses at molecular and cellular levels (39-41). It differs from conventional functional diagnostic imaging, which is used to examine the dysfunctional alternation on anatomic level rather than the cellular abnormalities that are more pivotal for disease assessment (42). Development of specific, sensitive and high-resolution molecular imaging technologies requires connection with basic medical or biological research, which can reveal new unique ligands, and imaging techniques by exploiting new imaging programming. These two aspects have a common interest in developing of state-of-the-art molecular imaging techniques. Several attempts have been undertaken to develop or to improve applications of MI in cardiovascular research. However, Sensitivity to imaging molecular alternations require optimize compensation for signal loss in dynamic motion, and improved co-registration of molecular and anatomical imaging is also required (43-45). Imaging of specific biomarkers will lead to early detection and characterization of disease, more accurate assessment of therapy response, and a better understanding of the disease process. Therefore, more and more significant advances in molecular imaging were noticed. The common molecular imaging modalities are listed (Table 1). They include magnetic resonance imaging (MRI), positron emission tomography (PET), single photon emission computed tomography (SPECT), optical imaging and ultrasound. Each technique has its own unique applications, advantages, and limitations. Vascular biology of atherosclerosis suggests several molecular processes that could serve as imaging targets (Table 2).

Table 1. Common Molecular Imaging Modalities

Imaging Modality	Spatial resolution [mm]	Sensitivity (mol/L) Probe	Advantages	Disadvantages
Optical Imaging	<1(FRI);1(FMT)	Likely 10^{-9} _- 10^{-12}	High sensitivity, numerou selections of probes preclinical study	Low depth, attenuation of signal, Limited clinical potential
PET	1-2 (μ-PET) 6-10 (clinical PET)	10^{-11}_10^{-12}	High sensitivity, clinical translation, functional quantitative. Higher spatial resolution than SPECT	Radioactive, Relatively low spatial resolution
SPECT	0.5-2 (μ-SPECT); 7-15 (clinical SPECT)	10^{-10}_10^{-11}	High sensitivity, clinical translation, functional quantitative	Radioactive, Relatively low spatial resolution
MRI	0.01-0.1 (high resolution MRI); 0.5-1.5 (clinical MRI)	10^{-3}_10^{-5}	High spatial resolution, Superb soft-tissue discrimination; anatomic and functional data	Low sensitivity, long scan and imaging processing time, limited probes quantitative
Ultrasound	0.04-0.1 (high frequency US);0.15-1 (clinical US)	Single micro-bubble	Real-time, superb blood imaging, low-cost, easy operation, portable	Low targeting contrast agent efficiency, low specificity

FRI: fluorescence reflectance imaging; FMT: fluorescence molecular tomography, PET: positron emission tomography; SPECT: single photon emission computed tomography; MRI: magnetic resonance imaging;

Table 2. Molecular targets in atherosclerosis

Targets	Examples
Endothelial activation(46)	Adhesion molecules, class II histocompatibility molecules (47,48)
Accumulation and activation of cells	White blood cells (especially monocytes), smooth muscle cells
Visualization of inflammatory mediators	Fractalkine, chemokine receptors (49-52)
Metabolic activity of cells within atherosclerotic plaque	Glucose transport (53-55)
Plaque procoagulant activity	Tissue factor, factor XIII (56)
Proteolytic enzymes	Cathepsin K, matrix-metalloproteinases (57-59): gelatinases and collagenases
Reactive oxygen species	Superoxide anion ($O2^-$) (60), hypochlorous acid
Angiogenesis markers	Integrin $a_V b_3$ (61)

2.3.1 Magnetic resonance imaging

Magnetic resonance imaging (MRI) is a well-established imaging method for different kinds of chronic and acute inflammation in numerous diseases. The current development in spatial resolution and constructive contrast agent make it a promising imaging technique for the characterization of inflammatory vessel walls and atherosclerotic plaque.

In the last twenty years, MRI was continuously developing by enhancing spatial resolution and reducing imaging acquisition time, thereby providing more detailed physiopathological information for diagnosis. The most outstanding advantage of MR imaging is its flexibility combining different sequences and modified contrast agents. For atherosclerosis investigation, novel advances in coil design binding with faster imaging acquisition technologies increased spatial resolution, enabling unstable atherosclerotic plaque to be non-invasive visualized with a high signal-to-noise ratio in patients.

Additionally, MRI is performed to detect atherosclerotic plaques by using multi-contrast acquisition methods with or without contrast agent administration. However, for the evaluation of unstable plaques among stable plaques, more specific, sensitive contrast agents required to be designed. The major drawback remains the selecting of biological target, multi-functional design of contrast agents to achieve this goal.

2.3.2 Optical imaging

Optical imaging (OI) is widely used preclinically based on the detection of light photons after their interaction with the disease lesions. Bioluminescence imaging (BI)(62-64) and fluorescence imaging (FI) are the major forms of optical imaging (65-67). FI is capable of detection of surface fluorescence signals. These fluorescent molecules could be inherently existed in animal, such as interacting with fluorescence protein as a reporter; or to use modified fluorescent nanoparticles known as quantum dots as a tracer to track interested biomarkers.

The inherent limitation of OI is imaging depth due to low penetration of light through the tissue. Although attenuation of fluorescence signal is a limitation for all optical imaging approaches, the superiority of FI methods including high sensitivity, high resolution, and the possibility of various design of tracers and signal amplification strategies make it as a promising imaging techniques in preclinical research.

2.3.3 Ultrasound Imaging

Ultrasound has potential advantages in cardiovascular molecular imaging development as well. It is widely available and portable. Blood flow can be visualized easily and non-invasively by Doppler methods. Achieving molecular targeted imaging mainly is contributed by the development of microbubble contrast agents. All the contrast agents have in common the feature that they are micro-sized particles, which produce an ultrasound signal in response to an ultrasound field. Most commonly, the microbubbles are composed of perfluorocarbon or nitrogen gas encapsulated by shells made of phospholipid, liposome, or biodegradable polymers the capability to image cellular activity and the possibility of molecular targeting using labeled microbubbles (68-73). The modified microbubble are targeted to specific molecules, which present on the cell/tissue surface of interest. For ultrasound molecular imaging of atherosclerosis, targeting strategies for microbubbles exploit either the shell characteristics for attachment to activated leukocytes within inflamed vessels, or specific targeting by conjugation to inflammatory molecules on the active endothelium overlying atherosclerosis plaque (74). However, ultrasound's poor resolution, inadequate quantitative data, and much reliance on operator experience limit its use in identifying vulnerable plaques.

2.3.4 Nuclear imaging

Currently, positron emission tomography (PET) and single photon emission computed tomography (SPECT) have been under evaluation for imaging vulnerable plaques by detecting inflammatory activity both in human and animal studies.

Especially PET imaging shows great superiority in cardiovascular molecular imaging, it is performed in terms of injection of radiolabeled imaging probes to assess the function and activity in different disease by assessing the radiotracer's accumulation. Unlike another conventional imaging (eg, radiography and computed tomography that characterizes the anatomy of disease-zone (eg, luminal diameter, plaque size), nuclear imaging techniques have been validated to visualize cellular-scale events (eg, protein regulation, molecular metabolism), which is able to reveal disease processes.

Numerous biomarkers correlated to metabolic or pathological progression in vulnerable plaque have been investigated as imaging target, such as matrix metalloproteinase (MMP) using MMP inhibitors; macrophage apoptosis with technetium-99m-labeled annexin-V, ^{18}F-galacto-RGD, which targets αvß3-integrin for evaluating angiogenesis within the plaque as well as

fluorodeoxyglucose (^{18}F-FDG) commonly used to evaluate inflammatory activity within the plaque (82). Although ^{18}F-FDG PET visualizes plaques inflammation nicely and a large number of studies demonstrated that ^{18}F-FDG accumulation in atherosclerosis correlates with the macrophage density in plaques, some questions still remain with respect to if and how this inflammatory signal can be employed for predicting plaque rupture. Moreover, ^{18}F-FDG-PET by detecting glucose uptake cannot reflect the inflammation directly and is less reproducible.

Compared with other conventional diagnostic imaging techniques, PET imaging shows conspicuous superiority. It features high sensitivity, which contributed by radiotracers and PET crystal scanner. Therefore, PET has become one of the most frequently used molecular imaging techniques clinically. The hybridization of PET with CT and MR provides additional anatomical details to the lesions, allowing both functional and anatomical imaging.

In the development of all cardiovascular nuclear imaging, the most crucial factor is the constructive design of sophisticated imaging tracers with high specificity for various molecular targets (Table 3) and sensitive for sensor detection.

Table 3. Currently potential biomarkers as targets for nuclear medical imaging of atherosclerosis

Biological process	Category	Specific biomarker and radiotracers
Angiogenesis	Endothelium	αvβ3_^{68}Ga-DOTA-RGD, ^{18}F-Galacto-RGD(61)
Apoptosis	Cell membrane	Annexin A5_^{99m}Tc-annexin(75)
Cell adhesion	Endothelial surface receptors	VCAM-1_^{18}F-4V
Macrophage/ Lymphocyte activity	Surface receptors	Somatostatin receptors_^{68}Ga-DOTATATE,Translocator protein (TSPO)_^{11}C-PBR28;
	Metabolism	Hexokinase, GLUT-1_^{18}F-FDG
	Proteases	MMP_^{124}I-HO-MIP (CGS 27023A)_ ^{18}F-MMPI
Thrombosis	Platelet glycoprotein IIb/IIa receptor fibrin	P-selectin_^{99m}Tc-Fucoidan,^{99m}Tc-apcitide

GLUT-1: glucose transporter-1, MMP: matrixmetalloproneinase, MMPI: matrixmetalloproneinase inhibitor, VCAM-1: vascular adhesion molecule-1, ^{18}F-FDG: 2-deoxy-2-18F-fluoro-D-glucose, DOTATATE: DOTA-(Tyr3)-octreotate, ^{11}C-PBR28: N-(2-methoxybenzyl)-N-(4-phenoxypyridin-3-yl)acetamide (72 – 80)

In our studies, three PET tracers were evaluated in inflammation of atherosclerosis. To examine macrophage density within the plaques, we used ^{68}Ga-DOTATATE and ^{18}F-FDG; to examine activity of plaque, we detected the inflammatory indicator, P-selectin, on the endothelium overlying plaques by ^{68}Ga-Fucoidan PET.

^{18}F-FDG PET

In cardiovascular disease, ^{18}F-FDG has proven to be useful in varied clinical fields including diagnosis, prediction and measurement of treatment effectiveness in myocardial infarction (76,77), and atherosclerosis (53,78-87) making it one of the most commonly used probes in cardiac PET imaging. Because ^{18}F-FDG is a glucose analogue, cells participating in the inflammatory process must use glucose as energy supplier. Macrophages can also metabolize free fatty acids, this needs oxygen to generate adenosine triphosphate, whereas glucose metabolism does not. Therefore glucose is the major substrate for macrophages resident in plaque (88,89). ^{18}F-FDG uptake is affected by several factors: the expression amount of GLUTs at the cell membrane, the hexokinase enzyme activity (90), and the rate of ^{18}F-FDG dephosphorylation. Uptake of ^{18}F-FDG in macrophages depends on the glucose concentration and the degree of macrophage activation (91). In ordinary monocytes, GLUT-3 expresses with higher concentrations than GLUT 1; but the insulin-sensitive GLUT 4 subtype is not detectable significantly. Activation of cells up-regulate both GLUT 1 and 3 expression. Furthuremore, macrophages produce a massive amount of hexokinase during inflammatory stimulation (92,93). However, ^{18}F-FDG also accumulate at other plaque cell types, including endothelial cells (94). For another important clinical trail, diabetic patients with high risk of the complications of atherosclerosis are related important, since the effect of hyperglycemia on plaque ^{18}F-FDG uptake should be considered. Theoretically, ^{18}F-FDG accumulation can be diminished by hyperglycemia, due to competitive uptake between ^{18}F-FDG and glucose. However, cell culture experiments and murine studies suggest that moderate hyperglycemia, does not adversely affect ^{18}F-FDG uptake in inflammatory cells (95-97). Reproducibility of atheroma imaging with ^{18}F-FDG still remains challenging, in those with high blood glucose at the time of imaging compared with hypoglycemic patients.

Animal models of atherosclerosis have been used to explore the basis of vascular focal ^{18}F-FDG uptake. The first article demonstrating that ^{18}F-FDG arterial uptake is related to atherosclerosis was reported in 1996. Tawakol et al (98) reported that although ^{18}F-FDG uptake correlated strongly with macrophage infiltration. The most inflamed areas of plaque accumulated almost 20 times more ^{18}F-FDG than control arteries. And there is no confirmed association between ^{18}F-FDG uptake and plaque size, luminal stenosis, or the density of

plaque smooth muscle cells. The related studies suggest that the metabolic signal in plaques is predominantly due to the presence of macrophages. Additionaly, an autoradiographic assessment demonstrated enhanced ^{18}F-FDG uptake after cholesterol feeding in both wild-type (75) and ApoE mice (95,99-101).

In clinical studies, first prospective ^{18}F-FDG -PET study to quantify atherosclerotic inflammation in atherosclerosis was from Rudd and colleagues (55). They found increased ^{18}F-FDG uptake at carotid artery lesions with severe symptom from patients with transient ischemic attack (Fig. 3). In corresponding ex vivo studies, accumulations of deoxyglucose within macrophage-rich areas of the excised carotid plaques were detected. They also showed enhanced focal ^{18}F-FDG uptake in the culprit vertebral arteries of patients with symptomatic posterior territory stroke(102). Nowadays, ^{18}F-FDG -PET has been investigated from the carotid and vertebral arteries to the aorta and iliac and femoral arteries (54,82,103,104). A significant correlation between ^{18}F-FDG uptake and plaque inflammation has been demonstrated in clinical investigations. Nevertheless, ^{18}F-FDG -PET imaging for coronary artery still remains changeling owing to significant myocardial uptake of ^{18}F-FDG. The major obstacles include the myocardium uptake ^{18}F-FDG actively under normal condition and considerable cardiac motion. In spite of challenges and inherent limitations, some groups have reported ^{18}F-FDG accumulation is correlated with symptomatic coronary lesions (86,105-108).

Consequently, increased ^{18}F-FDG PET is approved with capability to detected activated macrophage within the plaque. And since an abundance of invading macrophages causes inflammation that makes plaques vulnerable to rupture, thus, ^{18}F-FDG -PET imaging of macrophages is effective for diagnosing unstable plaques in murine atherosclerotic lesions. Since glucose metabolism is up regulated in activated macrophages, ^{18}F-FDG has been used widely for preclinical and clinical studies.

^{68}Ga-DOTATATE PET

Due to its ability to provide both structural and functional informations, ^{18}F-FDG PET/CT holds great potential in the evaluation of vulnerable plaques. As inflammation detection has become the major concept in atherosclerosis PET/CT imaging, a more specific tracer is still to be found. (1,4,7,10-tetraazacyclododecane-*N,N′,N″,N‴*-tetraacetic acid)-d-Phe^{1},Tyr^{3}-octreotate (DOTATATE) labeled with a generator-derived positron-emitting isotope Gallium-68 (^{68}Ga) selectively binds to somatostatin receptor 2 (SSTR2). ^{68}Ga-DOTATATE is routinely used for staging and restaging of neuroendocrine tumors (109)，and often followed by peptide receptor radionuclide therapy (PRRT) with ^{177}Lu-DOTATATE (110,111). Importantly, SSTR-2 was also

found specifically expressed and upregulated on human macrophages (112-114), suggesting that SSTR-2 could be an important target for molecular imaging and therapy in atherosclerosis. For several reasons, assessment of the up-regulated somatostatin receptors in vascular inflammation using specific somatostatin receptor radiotracers such as ^{68}Ga-DOTATATE, ^{68}Ga-DOTATOC or ^{68}Ga-DOTANOC may be superior to established ^{18}F-FDG for atherosclerosis imaging: There are more specific for inflammation, and lacks myocardial uptake making it better suited for visualizing coronary arteries. Recently, ^{68}Ga-DOTATATE-PET was proven to be a more specific alternative to the assessment of macrophages with PET/CT has been published (115,116).

Imaging of P-selectin

P-selectin is an adhesion molecule, which is highly expressed on the surface of active endothelium and platelets. It plays a pivotal role in recruiting leukocytes to the sites of injury (34,117,118). This interaction is mediated by P-selectin glycoprotein ligand 1 (PSGL-1), expressed by monocytes, neutrophils and platelets (119,120). Most active atherosclerotic lesions remain undetected until plaque rupture and thrombosis occur. A previous study found that inflamed atherosclerotic plaques have a strong expression of P-selectin on the overlying endothelium, but much less in normal arterial endothelium or in endothelium overlying inactive fibrous plaques (121). Consequently, P-selectin is thought to be an effective biomarker for assessing the bioactivity of active plaques.

Fucoidan is a synthetic Sialyl-LewisX (sLe^X) mimic, which is the natural ligand of P-selectin and is found on leukocytes (122,123). It is mainly derived from brown seaweed with an efficient binding of P-selectin as well (124). In previous studies, a high specific affinity of fucoidan for P-selectin was confirmed (124). Since fucoidan exhibits a great potential as a targeting probe, and PET with ability to do absolute quantitation possesses more investigative significance as compared to SPECT (Fig. 5) (125).

3. BACKGROUND AND AIM OF THE PHD-THESIS

Cardiovascular diseases remain the leading cause of mortality and morbidity worldwide. Rupture of atherosclerotic plaque accounts for approximately 70% of fatal acute myocardial infarction and sudden heart deaths.

Noninvasive diagnosis of vulnerable plaque still remains a great challenge and a huge research prospect, which triggered us to investigate the feasibility of PET imaging on the evaluation of atherosclerosis. Molecular imaging of inflammation in atherosclerosis could provide a promising diagnostic tool for identifying vulnerable atherosclerotic plaque or early detection of inflammatory endothelium at risk in vivo. However, a specific imaging tracer for clinical applications has not been developed at yet. The aim of this work, was to assess the potential of novel PET imaging probes associated with intra-plaque inflammation on animal models and in human respectively.

In our retrospective studies, we try to evaluate inflammation in the plaques. Both animal and translated human studies were performed.

The purpose of animal study was to assess ^{68}Ga-DOTATATE and ^{68}Ga-Fucoidan on ApoE-/- mice with severe plaques. ^{68}Ga-DOTATATE micro-PET was performed to detect infiltrated macrophage within the plaques. And ^{68}Ga-Fucoidan micro-PET was performed to present P-selectin expression on the endothelium overlying the plaques, in order to evaluate inflammatory activation on the plaques.

The purpose of our human study was to evaluate inflammatory activity within the atherosclerotic plaques by ^{68}Ga-DOTATATE PET imaging. The relationship of focal vascular ^{68}Ga-DOTATATE uptake to commonly known risk factors for cardiovascular disease and calcification were correlated. ^{18}F-FDG, as most commonly used radiotracer, has already been assessed by several groups (57,105,126). We also validate the correlation to vascular ^{18}F-FDG uptake and compared with ^{68}Ga-DOTATATE, We collected initial evidence from a retrospective analysis to characterize and modulate atherosclerotic plaque biology of oncology patients.

4. ANIMAL STUDIES

Evaluation of ^{68}Ga-DOTATATE and ^{68}Ga-Fucoidan on Apoliprotein E knockout mice with atherosclerosis.

4.1 Materials and Methods

Animal models and preparation

Animal care and experiments were in compliance with the German animal protection law and were approved by the local district government of Unterfranken (AZ: 55.2-2531.01-19/07). Female apolipoprotein E (ApoE)-/- mice (n=8) were studied at the age of 50 weeks. Mice were fed high-cholesterol diet from age of 8 weeks, which is known to result in severe atherosclerotic plaques. The experiments were conducted at room temperature (RT). Mice were anesthetized during all procedures (isoflurane 2% to 2.5%, Baxter). Advanced atherosclerotic plaques were confirmed by histology. Non-atherosclerotic C57 mice (n=3) were studied as control group.

Cell culture

Murine macrophages/monocytes digested from fiv=\e mice spleen and lymph node maintained in RPMI 1649 medium supplemented with 10% heat-inactivated FCS, non-essential amino acids, 1mM sodium pyruvate, 100 U/ml and 100 µg/ml streptomycin, 2 mM L-glutamine and 30 µM mercaptoethanol (all from Gibco). Cells were incubated overnight at 37°C and 5% CO_2 in the presence and absence of 10 ng/mL LPS (Sigma). Upregulation of IL-6 protein level in culture supernatants was confirmed by Enzyme-linked immunosorbent assay (ELISA) at time point of 50h after LPS stimulation (supplementary Fig. 1). In order to prove SSTR-2 expression on endothelium, the murine endothelial cell line b.END.3 was purchased from American type Culture Collection. The adherently growing cells were cultivated under standard condition at 37°C in a humidified 95% air/ 5% CO_2 incubator, maintained in the complete growth medium. It mainly including Dulbecco's Modified Eagle's Medium (DMEM) (Gibco), supplemented with 10% fetal calf serum (Gibco), 100 U/ml penicillin and 100 µg/ml streptomycin. The b.End.3 cells were used at passages 25 to 30 for ^{68}Ga-Fucoidan study. To activate inflammation, bEnd.3 cells were treated with 1 µg/ml of LPS (E. coli. 026:B6, Sigma) for 48 hours1. Subsequently, stimulated and non-stimulated b.End 3 cells were lysed for westernblot analysis.

Western blot analysis for the expression of SSTR-2 and P-selectin

For analyzing of SSTR-2 expression, stimulated and non-stimulated macrophage were lysed in 100 µL ice-cold lysis buffer, the lysates were centrifuged at 12,000g at 4°C for 5 min to remove cellular debris. The supernatant was collected. 40 µL of supernatant containing the cell total proteins was separated by 10% sodium dodecyl sulfate polyacrylamide gel electrophoresis (SDS-PAGE) and transferred to nitrocellulose membrane (semidry western blot). After blocking with TBST containing 5% nonfat dry milk for 1h, the membrane was further incubated with 5ml TBST/5% nonfat dry milk solution containing 5 µL rat anti mouse SSTR-2 primary antibody (ab9550, Abcam) for 24h at 4°C. After washing three times, the membranes was incubated with 5mL TBST solution containing 5 µL HRP-labeled goat anti rat IgG secondary antibody (Santa Cruz) for 1h.

For P-selectin expression analysis, stimulated and non-stimulated b.End 3 endothelial cell were lysed in 100 µL ice-cold protein extraction reagent type 4 lysis buffer (Sigma-Aldrich), the lysates were centrifuged at 12,000g at 4°C for 5 minutes to remove cellular debris. The supernatant was collected. 40 µL of supernatant containing the total cell proteins was separated by 10% sodium dodecyl sulfate polyacrylamide gel electrophoresis (SDS-PAGE) and transferred to nitrocellulose membrane (semidry western blot). After blocking with TBST containing 5% nonfat dry milk for 1h, the membrane was further incubated with 5ml TBST/5% nonfat dry milk solution containing 5 µL rat anti mouse P-selectin primary antibody (antibody online) for 24h at 4°C. After washing three times, the membranes were incubated with 5mL TBST solution containing 5 µL HRP-labeled ECL anti-mouse IgG secondary antibody (GE Healthcare) for 1h. The immunoblot were developed using the ECL detection system (GE Healthcare).

Histology and immunochemistry

In ^{68}Ga-DOTATATE study, for immunofluorescence staining 8 µm aortal sections were dried at room temperature and fixed in ice-cold acetone, washed in PBS buffer and incubated with 3% goat serum to avoid unspecific binding. Rat anti mouse CD68 monoclonal antibody (MCA1957, 1:75, AbD Serotec) was given for 90 min visualized by goat anti rat biotinylated secondary antibody (BA 9400, (1:300) Vector Laboratories, Burlingame, UK) for 30 min and Streptavidin–FITC (SA-5001, (1:100) Vector) for 30 min in green. After blocking with Avidin/Biotin blocking Kit (SP-2001, Vector) primary antibody against SSTR-2, rabbit anti-mouse (ab9550, Abcam) in dilution of 1:100 was incubated over night at 4°C. Biotinylated goat anti rabbit (BA-1000, (1:300) Vector) and Streptavidin Alexa Fluor 546 (S11225, (1:100), Invitrogen) showed red colour of the somatostatin receptor. DAPI (1:1000, Merck) was used to

stain nuclei in blue. All images were conducted using a conventional fluorescence microscope (Zeiss Axiovision, Zeiss, Oberkochen, Germany).

For immunohistology the sections were fixed in ice-cold acetone followed by 20 min treatment with 0.3% hydrogen peroxide/methanol to inhibit endogenous peroxidase. Subsequently, sections were blocked with Avidin/Biotin Blocking Kit (Vector S 2000, Vector Laboratories, Burlingame, UK) in rabbit serum and incubated with the primary antibody CD68 (rat anti mouse, 1:75, AbD Serotec) at 4°C over night. After washing with PBS, the sections were incubated with the biotinylated secondary antibody (rabbit anti rat, BA-4001, Vector) for 1 hour, washed in PBS and stained with ABC KIT (Vectastain, PK-6100) for 30 min. Visualization was performed with Diaminobenzidine (DAB) (abcam, ab675) for 5 minutes. The reaction was blocked with water; slides were counterstained with Hematoxylin, dehydrated in ethanol/xylene and mounted with Entellan Mounting Medium (Merck). For the demonstration of the plaque morphology we used haemalaun & eosin (H&E) staining according to Mayer.

In ^{68}Ga-Fucoidan study, after ^{68}Ga-Fucoidan PET, Aortas were excised and frozen in Tissue-Tek O.C.T Compound (Sakura Finetek Europe B.V., Alphen aan den Rijn, The Netherlands) on dry ice, sliced in sequential longitudinal sections (n=300) and transverse sections (n=200) of 8 µm and 20 µm at -22°C (Leica Cryotome CM1850, Leica Microsystems) and mounted onto microscope slides. The 20 µm sections underwent autoradiography and were apposed to an imaging plate over night for autoradiography. Autoradiographic images of longitudinal sections mainly included descending aorta, abdominal aorta, they were obtained in order to compare the uptake of activated and in inactive plaques. Transverse sections mainly include right and left subclavian artery, brachiocephalic artery, ascending aorta arch of aorta and part of descending aorta, Autoradiographic images of these arteries were used to correlate tracer's uptake with anatomic MR imaging. The 8 µm sections were used for staining with H&E to demonstrate morphology and for immunohistology. P-Selectin primary antibody (ABIN670131, Antibodies online, Aachen, Germany), was used for visualization of early atherosclerosis, followed by a biotinylated secondary antibody (BA-1000, Vector Laboratories, Burlingame, UK) and streptavidin (ABC KIT, PK-6100, Vector Laboratories, Burlingame, UK) and stained with Diaminobenzidine (DAB substrate KIT, abcam ab94665, Cambridge, U.K.). The sections were counterstained with Hematoxylin, dehydrated in Ethanol and Xylene and mounted with Entellan (Merck 1.07960, Darmstadt, Germany). For immunofluorescence double staining the sections were incubated with primary antibody against P-selectin (ABIN670131, rabbit anti mouse, Antibodies online, Aachen, Germany), and vWF (ab11713, sheep anti mouse, Abcam, Cambridge, U.K.) or CD68 (MCA1957, rat anti mouse, AbDSerotec , Düsseldorf, Germany) as secondary primary antibody. After a two step staining procedure with biotinylated secondary antibody (BA-1000 against P-selectin, BA-6000 against

vWF, and BA-9400 against macrophages, all Vector Laboratories, Burlingame, UK) and streptavidin in two different fluorescent colours, Alexa Fluor 546 (S11225, invitrogen, Karlsruhe, Germany) and (Streptavidin-FITC, SA-5001 Vector Laboratories), 4',6-diamidino-2-phenylindole (DAPI) was used for nuclear staining. Images were taken with a Zeiss Axioskop 2 plus Fluorescence Microscope.

For Sudan IV staining, aortae were fixed in 4% formaldehyde. The aortae were opened longitudinally, from the aortic arch to the iliac arteries. The primary incision followed the inner curvature of the arch. To obtain a flat imaging, an incision was made along the outer curvature of the arch. The aortae were then pinned on a black wax surface using stainless steel pins 0.25 mm in diameter. After being rinsed with water, the aorta was exposed to isopropanol (60%) for 2 min, followed by 35 minutes of staining with a Sudan IV solution, which contained 5 grams of Sudan IV, dissolve into 500mL acetone & 500mL 70% EtOH. The excess stain was removed with 80% EtOH and running water subsequently. Whole aortas were imaged using a microscope with a digital camera (Leica).

Statistical analysis

Statistical Package for Social Sciences (SPSS version 11.0; SPSS Inc.) was used for statistical analyses. Continuous variables with a normal distribution were recorded as mean ± standard deviation (SD). Group comparisons were made using two-tailed T-test, P-value of less than 0.05 was considered statistically significant.

4.1.1 ANIMAL STUDY I: Macrophage characterization of atherosclerosis: ^{68}Ga-DOTATATE ex-vivo detection in mice

Preparation of ^{68}Ga-DOTATATE

Preparation of ^{68}Ga-DOTATATE has been established in the department of nuclear medicine for clinical applications. ^{68}Ga-DOTATATE used in the present study was synthesized on a computer-assisted synthesis-module (Scintomics, Fürstenfeldbruck, Germany). ^{68}Ga for radiolabeling was eluted in form of $^{68}GaCl_3$ with 0.1 M HCl from a ^{68}Ge/^{68}Ga-generator (Obninsk, Russia) into a reactivial (Thermo Scientific, Langenselbold, Germany), containing 10 µg of DOTATATE and HEPES-buffer. After 10 min at 95 °C, the crude product was separated via a Waters-Sep-Pak-C18 cartridge (Waters, Eschborn, Germany), diluted with 0,9 % NaCl and filtrated through a 0.22 µm sterile filter (Millipore, Cork, Ireland) into a sterile vial (IBA, Berlin, Germany) for biological evaluation.

Radiochemical purity, as assessed by gradient HPLC (eluent A: 0.1 % TFA in H_2O, eluent B: 0.1 % TFA in acetonitrile, flow rate: 0.7 ml/min, column: Nucleosil 100-5 C18 125x4.6 mm, gradient: nonlinear 0 % to 100 % solvent B in 15 min; Scintomics, Fürstenfeldbruck, Germany) and TLC (eluent: 0.1 M citric acid, stationary phase: ITLC-SG stripes (Varian, Lake Forest, USA); measurement time: 1 min; miniGITA, raytest, Straubenhardt, Germany) was >99%. The specific activity of the injection solution amounted 50 MBq/µg.

Purification of monocytes/macrophages

Erythrocyte-depleted spleen cells were stained in fully-supplemented RPMI medium with anti-CD11b-PE (clone M1/70, BD Biosciences), anti-Ly-6G (clone 1A8, Biolegend) and anti-CD11c-eFluor 450 (clone N418, eBioscience). After a final washing step, cells were resuspended in RPMI medium and sorted with FACSAria III cell sorter (BD Biosciences). Monocytic cells were defined as CD11b^{high}, Ly-6G^{-}, CD11c^{-}.

FACS analyze of SSTR-2 expression on leukocytes, endothelial cells and platelets.

We used flow cytometry to measure SSTR-2 expression within the arterial wall. Since cluster of differentiation 31 (CD31) is platelet endothelial cell adhesion molecule (PECAM), murine endothelial cells line (b End.3) was confirmed by flow cytometry separately. Samples of the

aorta (n=3) were dissected under a microscope. Digestion: collagenase type 2 and protease type XIV (0.895 mg/ml and 0.5 mg/ml respectively) in PBS the aorta was incubated for 1 h at 37°C. blood were collected as well. Cells were pre-blocked with anti-Fcγ receptor III/II monoclonal antibody (mAb) (clone 2.4G2) and 5% rabbit serum for 15 minutes at 4°C for 15 minutes and subsequently stained with anti-CD41(biolegend), anti-CD3ε(biolegend), anti-CD11b (ebioscience), anti-Ly-6G (biolegend) and anti-SSTR-2 (Abcam). To examine the SSTR-2 expression on endothelial cell, b.End.3 cells were stained with anti-CD31 (biolegend), after washing, cells were blocked with 5% goat serum and anti-SSTR-2 mAB was detected via polyclonal biotinylated goat anti-rabbit mAB. At the end, we added Streptavidin-FITC (dilution 1:500). The cells were washed in FACS buffer between every step three times. Every incubation step took 15 minutes. Measurements were performed on LSRII (BD biosciences). For plots FloJo software (treestar) was used.

Autoradiographic analysis

ApoE-/- mice (n=5) were sacrificed one hour after injection (15±1.5 MBq); accumulation of ^{68}Ga-DOTATATE in the aorta was assessed using 20 µm sections (n=100) of sample tissues with a digital autoradiography system (CR 35 BIO, Buerr Medical, Bietigheim Bissingen, Germany). Region of interests (ROI) analysis of images was performed to determine activity ratios for the plaque area relative to the non-plaque area. Aorta sections (n=60) from non-atherosclerotic C57 mice (n=3) were also assessed as well, In order to evaluate specificity of ^{68}Ga-DOTATATE uptake, sections from non-injected ApoE-/- mice were incubated with antibody against SSTR-2 for 2 hours before incubating with ^{68}Ga-DOTATATE *in vitro* at room temperature. All images were processed by two-Dimensional median filtering algorithm (Matlab 7.0, Mathworks Massachusetts, U.S) before analysis.

4.1.2 ANIMAL STUDY II: Targeting P-selectin by Gallium-68 labeled Fucoidan PET for non-invasive characterization of vulnerable plaques: Correlation with in vivo 17.6T MRI

Preparation of ^{68}Ga-Fucoidan

Fucoidan was purchased commercially from Sigma-Aldrich (Deisenhofen, Germany) and was used without further purification for radiolabeling. The synthesis of ^{68}Ga-Fucoidan was carried out in the in-house radiopharmacy using a computer-assisted synthesis-module (Scintomics, Fürstenfeldbruck, Germany). ^{68}Ga for radiolabeling was eluted with 0.1M HCl in form of $^{68}GaCl_3$ from a ^{68}Ge/^{68}Ga-generator (Obninsk, Russia). The labeling procedure was optimized concerning the amount of Fucoidan, reaction time and reaction temperature. Optimization led to the following standard labeling protocol: $^{68}GaCl_3$ (typically 500- 750 MBq) was eluted with 0.7 mL of 0.1 M HCl directly in a reaction vial (Thermo Scientific, Germany) containing 300 µL of 0.1 M acetate buffer (pH = 4.8) and 50 µg (50 µl) of Fucoidan from a solution consisting of 1.0 mg Fucoidan/1mL saline). The solution was allowed to react for 10 min at 90°C, following by a purification of the crude product on a Waters-Sep-Pak-C18 cartridge (Eschborn, Germany), diluted with PBS (pH 7.0; Braun) and filtrated through a 0.22µm sterile filter (Millipore, Cork, Ireland) into a sterile vial (IBA, Berlin, Germany) for biological evaluations.

Quality control and in vitro stability were determined by HPLC (Shimadzu, Duisburg, Germany) using 0.01 M aqueous NaOH/acetonitile (9:1) at flow rate of 1.0 ml/min as mobile phase on a column (Dionex CarboPak-PA10, 250x4.5 mm, 10 µm) as stationary phase. Additionally, a thin-layer chromatography (TLC) was performed, applying the analyte to an ITLC-SG strip (Varian, Lake Forest, USA) using 0.1M sodium citrate as mobile phase. A TLC-scanner (mini-GITA®, Raytest, Straubenhardt, Germany) was used to image the TLC strips.

Cell uptake of ^{68}Ga-Fucoidan

The cellular uptake of ^{68}Ga-Fucoidan was tested on bEnd.3 endothelial cells with and without LPS stimulation. Radioactive substances which were diluted to $1.5*10^6$ counts per minute (cpm) / 1mL culture medium were added to the $1*10^6$ attached cells and incubation in a humidified 95% air/ 5% CO2 incubator for different time intervals (5min, 15min, 30min, 45min,) at 37°C. After incubation, interactions between cells and tracers were interrupted by placing samples on ice. Then, the cells were washed thrice with cold PBS (0.1mol/L, PH 7.4), and trypsinized in 0.5mL for measurement. Cellular uptake was measured using a high-energy gamma counter (Wallac, Rodgau, Germany).

Cell viability

To determine apoptosis induction, endothelial cells were treated with Fucoidan at concentration of 1µg/ml, 5µg/ml, 10µg/ml, 20µg/ml and 40µg/ml for 48 hours, subsequently harvested, and ready for apoptosis analysis. To determine the morphologic nuclear changes, phosphatidylserine exposure was determined using annexin V– pacific blue (BD Bioscience) in combination with 7aad (BD Bioscience). Harvested dual stained cells and subsequently analyzed by flow cytometry. The percentage of cellular apoptosis and necrosis was determined by examining 200 000 cells and counting the cells that were characterized by nuclear condensation and fragmentation. In experimental process, apoptosis induction experiments were performed in 24-well culture plates (Costar). Cultured as described above. Cells were treated with Fuciodan at concentration of 1µg/ml, 5µg/ml, 10µg/ml, 20µg/ml and 40µg/ml for 48 hours, subsequently harvested, and ready for apoptosis analysis. To determine the morphologic nuclear changes, Phosphatidylserine exposure was determined using annexin V– pacific blue (BD Bioscience) in combination with 7aad (BD Bioscience). Cells were harvested, washed, incubated with annexin V– pacific blue and 7aad for 15 minutes in the dark. As control, unstained cells, cells stained with annexin V– pacific blue (no 7aad) and cells stained with 7aad (no AnnexinV- pacific blue) were prepared to assess as well.

Animal studies

ApoE$^{-/-}$ mice were used in our experiments. In order to induce development of severe atherosclerotic plaques, ApoE$^{-/-}$ mice were fed with a high cholesterol diet (1.25% cholesterol, 7.5%cocoa butter, 7.5% casein) for 38 weeks starting at of age of 8 weeks To obtain mice with server atherosclerosis, all ApoE$^{-/-}$ mice were fed with Western diet (or 30 weeks at age of 4 weeks(127,128). As controls, C57BL/6 mice were fed with normal chow. Severe atherosclerotic plaques in ApoE$^{-/-}$ mice were confirmed by histology (H&E staining). All experimental protocols were in compliance with the German animal protection law and were approved by the local district government of Unterfranken (AZ: 55.2-2531.01-19/07).

Biodistribution of ^{68}Ga-Fucoidan in ApoE-/- mice

The biodistribution of ^{68}Ga-Fucoidan was determined in ApoE-/- mice (46 weeks old, n=3). Mice were sacrificed 60 minutes after intravenous injection of the radiotracer (4.9±0.6 MBq),

and perfused with 50 µL of saline, blood, heart, lung, kidney, brain, bone, leg skeletal muscle, fat, skin, spleen and liver were harvested and weighted. Radioactivity was subsequently measured by high-energy gamma counter (Wallac, Rodgau, Germany).

Magnetic resonance imaging

In vivo high resolution MR imaging was conducted on a 17.6 T vertical bore MR system (Bruker Biospin GmbH, Germany), using a homebuilt radiofrequency coil (birdcage design, ID: 27 mm). The images were acquired with an ECG-triggered and respiratory gated T1-weighted Multi-Slice-Multi-Spin-Echo-Sequence with following parameters: repetition time TR=1s; echo time, TE=9 milliseconds; bandwidth, 83 kHz; in-plane resolution 78µm × 78 µm; slice thickness 0.6 mm; total acquisition time= 20 minutes (129). Images were analyzed with OsiriX DICOM (Osirix) viewer software.

PET imaging

^{68}Ga-Fucoidan was administered intravenously into *ApoE*$^{-/-}$ mice (7.7±1.3 MBq) (n=10) and C57BL/6 control mice (6.5±0.8 MBq) (n=6) under anesthesia with 1.5% isoflurane post MRI scan. For the control, six C57BL/6 mice were administered intravenously with ^{68}Ga-Fucoidan (6.5±0.8 MBq). Imaging was performed from time point 50 minutes to 110 minutes (6 scans) after injection using a Siemens micro-PET system (Inveon) with a 10 minutes acquisition time. In order to better understand of influence of long blood half-life of ^{68}Ga-Fucoidan, and correct localization of aorta wall, after the first in vivo emission scan, murine (both ApoE-/- and C57BL/6 mice) liver, lung, spleen, kidney, intestines, stomach were carefully removed under the dissection microscope, then the mice were re-scanned using the same protocol as in the first time, subsequently the blood within heart and aorta were wash out by PBS buffer, and then scanned again for the third time using the same protocol. For the imaging reconstruction, OSEM2D algorithm was used. To quantify the ^{68}Ga-Fucoidan uptake, all micro-PET scans were reviewed for anatomic localization and amount of focal uptake. Representative segments of large arteries were analyzed, aortic arch, descending thoracic aorta, and abdominal aorta. Regions of interest (ROIs) were drawn around the wall of the selected aortic segments. The mean standardized uptake value (SUV) was extracted for the final calculation of target-to-background ratios (TBRs). Background was determined by the mean SUV of six different ROIs in the foreleg muscle. Transverse, coronal and sagittal views were analyzed. The relative tracer uptake is characterized as the TBR and SUV respectively. Quantitative dynamic PET studies were performed In order to understand tracer kinetics; the PET imaging data was

acquired from tracer injection to 100mins after injection. In order to estimate in vivo specificity of ^{68}Ga-Fucoidan, four apoE$^{-/-}$ mice were pre-injected of 1 mg sLe^{X} mixed in 100μL PBS respectively.

Ex vivo autoradigraphic study

All ApoE-/- mice (n=6) were sacrificed after the PET scan. Accumulation of ^{68}Ga-Fucoidan in the aorta was assessed using 20 μm sections of sample tissues with a digital autoradiography system (CR 35 BIO, Duerr Medical, Bietigheim Bissingen, Germany). Regions of interest (ROIs) were drawn to qualify activity ratios for the activated plaque areas relative to the inactivated plaque areas and the uptake ratios to the non-plaque were determined as well. In order to evaluate specificity of ^{68}Ga-Fucoidan uptake, tissue sections (n=40) from ApoE-/- mice were incubated with sLe^{x} for 24 hours before incubation with ^{68}Ga-Fucoidan *in vitro* at 4°C. Activated atherosclerosis were defined by intensive infiltration of blood-derived monocytes into arterial intima. Activated vulnerable plaques were characterized by thin fibrous cap and high-density macrophage infiltration; fibrous plaques were classified as inactivated plaque; Fatty-streak were classified as non-plaque lesions.

4.2 RESULTS

4.2.1 ANIMAL STUDY I: Macrophage characterization of atherosclerosis: ^{68}Ga-DOTATATE ex-vivo detection in mice

Flow cytometry of digested aortas & endothelial cells

Results of flow cytometry are shown in Fig. 3. Somatostatin receptor 2 was found to be expressed at significant levels the macrophage/monocyte ($CD11b^+Ly\text{-}6G^-$) (60.4%), on small part of T-cells ($CD3\varepsilon^+$)(28.3%), but no expression on neutrophils ($CD11b^+Ly\text{-}6G^+$) (0%) and platelets ($CD41^+$) (0.136%). Notably, SSTR-2 was found to be significantly expressed on bEnd.3 murine endothelial cells ($CD31^+$) (97.2%) as well.

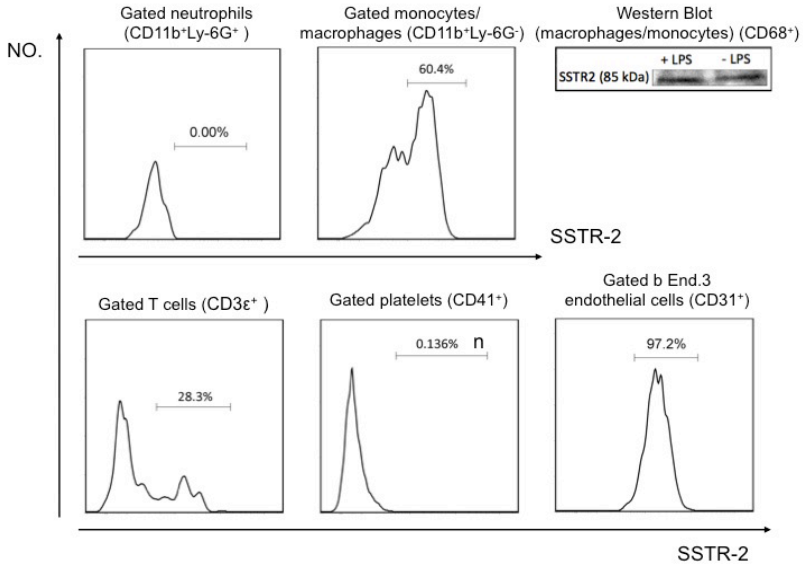

Figure 3: Flow cytometric analysis of digested aorta from ApoE-/- mice (n=3) with atherosclerotic plaque. Cells were gated by different markers, neutrophils ($CD11b^+$, $Ly\text{-}6G^+$), Macrophages and monocytes ($CD11b^+$, $Ly\text{-}6G^-$), T-cells (CD3 ε^+**)**, platelets ($CD41^+$) and b End.3 endothelial cells ($CD31^+$). Somatostatin receptors were detected expressed on most gated macrophages/monocytes (60.4 %), and part of gated T-cells (28.3%), but not detected on gated neutrophils (0%) and platelets (0.136%). Western blot analysis of SSTR-2 expression in macrophages/monocytes differentiated from mice spleen and lymph node. Cells were incubated in presence (+) or absence (−) of 10ng/ml LPS for 24h.

SSTR-2 expression on macrophages

We found significant expression of SSTR-2 in macrophages at the protein level by western blot. We also assessed the dose-dependent effect of the expression of SSTR-2 in response to the LPS stimulation. Results showed SSTR-2 was detected both in induced and non-induced macrophages. Treatment of macrophages with 10 ng/ml of LPS for 24h did not affect SSTR-2 expression (Fig. 3). As an indicator for macrophage activation, IL-6 secretion was assessed in the presence of LPS (10ng/ml) and was found to be significantly increased (Fig. 4)

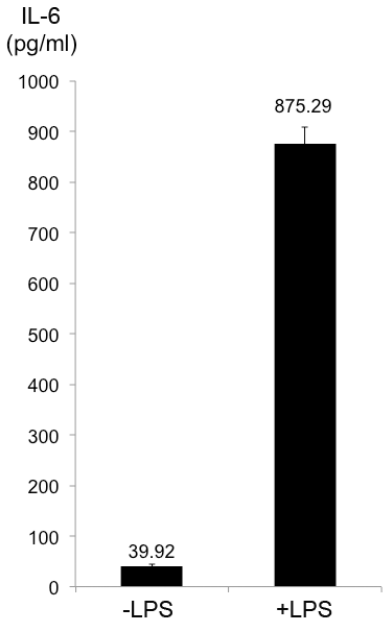

Figure 4: ELISAs were performed to determine IL-6 levels as a marker of inflammation; Equal quantities of total protein were used. Data are expressed on pg/ml of for IL-6.

Characterization of atherosclerosis

Histological experiments demonstrated that all ApoE-/- mice in our studies had severe atherosclerotic plaques. All tissue section samples showed high specific uptake of ^{68}Ga-DOTATATE into atherosclerotic lesions by autoradiography (Fig. 5A, Fig.6A) as confirmed by macrophage-specific DAB staining (Fig. 5B) and H&E histological staining (Fig. 5-6). The uptake of plaque-area from each single ApoE-/- mouse was significant higher than the non-plaque area (Fig. 5D).

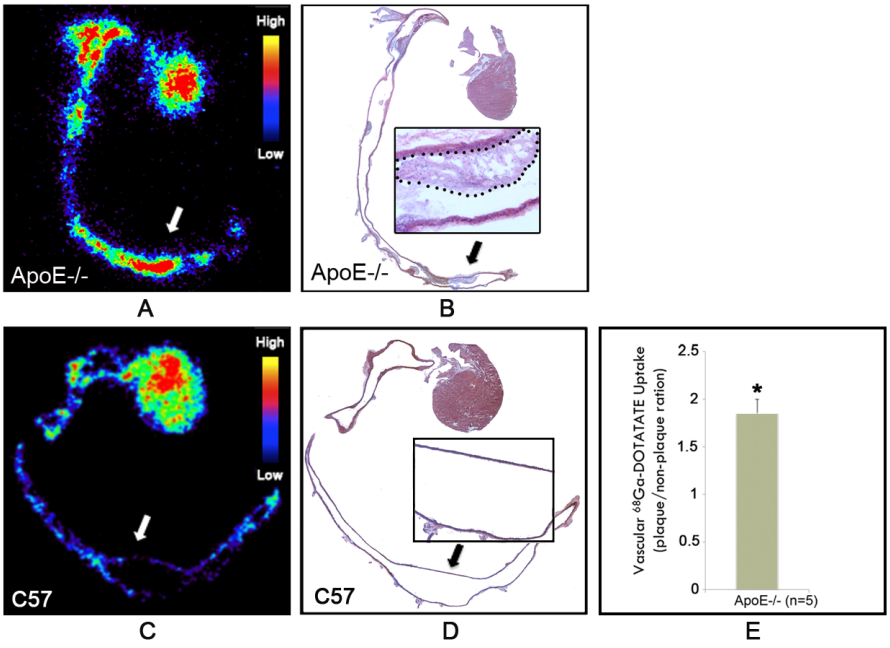

Figure 5: Ex vivo imaging of excised aortic section from atherosclerotic ApoE-/- mice (n=5). (A) Autoradiographic visualization of the ^{68}Ga-DOTATATE accumulation in aorta in an atherosclerotic plaque of an ApoE-/- mouse (section with 20 µm slice thickness); (B) H&E staining of adjacent-tissue section with 8 µm thickness. (C) Autoradiographic image and (D) H&E staining image of one negative control sample from three wild type C57 non-atherosclerotic mouse. (E) Ratio of plaque vascular uptake to non-plaque vascular uptake for ^{68}Ga-DOTATATE from five ApoE-/- mice. * $p<0.05$. Figure demonstrates that ^{68}Ga-DOTATATE accumulate in advanced atherosclerotic plaques which are marked by dotted line in H&E staining image, but few in the normal endothelium.

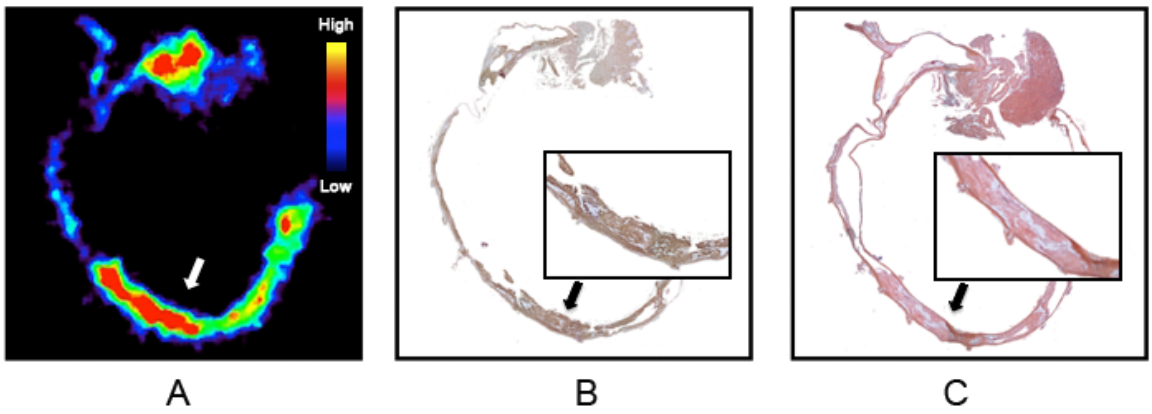

Figure 6: Representative Ex vivo Imaging of excised aortic sections from one of atherosclerotic ApoE-/- mice (n=5). (A) Autoradiographic visualization of the ^{68}Ga-DOTATATE accumulation in aorta in an atherosclerotic plaque of all mice (section with 20 µm slice thickness); (B) DAB staining and (E) H&E staining of adjacent-tissue sections with 8 µm thickness. The Fig. demonstrates that ^{68}Ga-DOTATATE accumulate in atherosclerotic plaques.

Co-localization of the SSTR-2 and macrophages in plaques was confirmed by the immunochemistry (Fig. 7). Receptor blockage using monoclonal antibodies against SSTR-2 resulted in a significant decrease of tracer accumulation in aorta, indicative of a high specificity of ^{68}Ga-DOTATATE uptake for the assessment of SSTR-2 (Fig. 8).

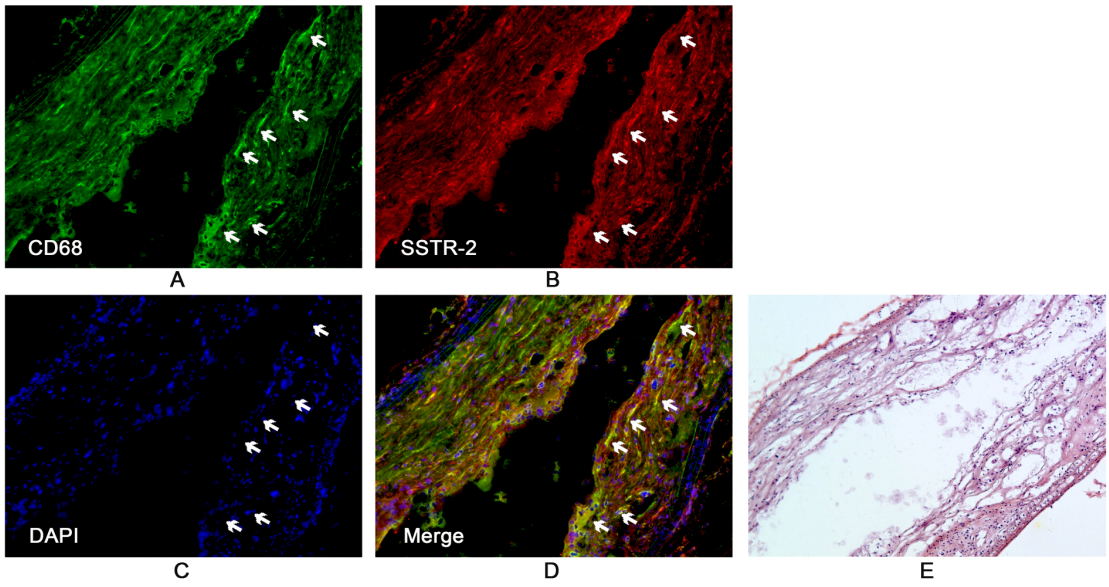

Figure 7: Representative immunohistological images from n=6 mice show the co-localization of SSTR-2 signal and macrophages. A Immunofluorescence staining of macrophage (CD68 green) in the plaque. B Anti-SSTR-2 monoclonal antibody highlights the regions with strong SSTR-2 expression (red). C Cell nuclei stained with DAPI (Blue). D Overlay of three channels (merge), image is representative for the co-locatization of macrophages and SSTR-2, supporting the notion that macrophage may be identified by ^{68}Ga-DOTATATE. Corresponding control images were shown. E Consecutive tissue sections were used for H&E staining. No SSTR-2 and CD68 expression was detected in control images (data not shown). Combined with Fig.2 this Fig. demonstrated ^{68}Ga-DOTATATE accumulates in areas of high macrophage content within atherosclerotic plaques of ApoE-/- mice.

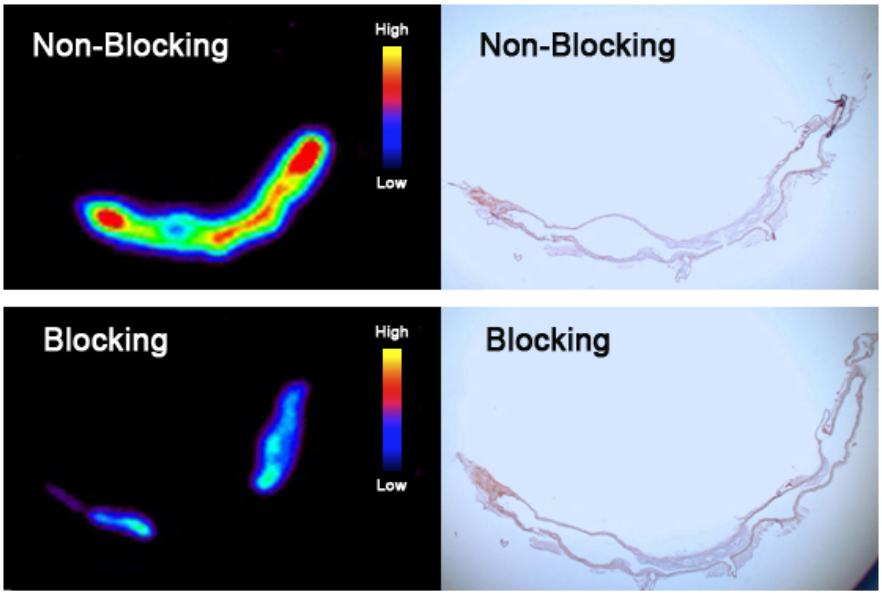

Figure 8: Pre-incubation of monoclonal antibody against SSTR-2 inhibited uptake of ^{68}Ga-DOTATATE in atherosclerosis plaque from ApoE-/- mice (n=3). (A) Autoradiography images show the lower uptake in the aorta pre-incubated with SSTR-2 targeted antibody. (B) Histology demonstrated the co-localization of atherosclerotic plaque with the area of increased ^{68}Ga-DOTATATE uptakes by H&E staining.

4.2.2 ANIMAL STUDY II: Targeting P-selectin by Gallium-68 labeled Fucoidan PET for non-invasive characterization of vulnerable plaques: Correlation with in vivo 17.6T MRI

Synthesis of ^{68}Ga-Fucoidan, in-vitro stability, and pharmacokinetics analysis

For optimization of the radiolabeling conditions varying the amounts of the Fucoidan (10 – 250 µg), reaction times (5 – 35 min) and different reaction temperatures (22 - 95°C) were tested. It was found that Fucoidan could be labeled with ^{68}Ga at 90°C within 10 min using 100 µg of Fucoidan at pH 3.4. ^{68}Ga-Fucoidan was obtained in an overall decay-corrected reaction yield of 90 ± 5% and 99% radiochemical purity. The total synthesis time including column purification on a reversed-phase cartridge and quality control were completed after 40 min. To determine the stability of ^{68}Ga-Fucoidan in injectable solution, additional TLC was performed at 1, 2, 3 and 4h after radiolabeling. The radiochemical purity was still > 98% and thus ^{68}Ga-Fucoidan showed an excellent in-vitro stability in an injection solution (PBS) for further biological investigations.

To assess the biodistribution of ^{68}Ga-Fucoidan in mice, all data were corrected for decay and residual activity at the injection sites, the tracer uptake was expressed as the percentage of initial injected dose per gram of tissue after correction for decay (Fig. 9). Biodistribution are expressed as %ID/g; kidney=5.9±1.4, heart=5.7±1.3, spleen=4.1±0.7, liver=4.7±1.2, blood=16.8±3.2, bone=1.4±0.2, lung=3.1±0.9, brain=1.2±0.2, fat=0.9±0.1, muscle=0.8±0.1, skin=0.8±0.1.

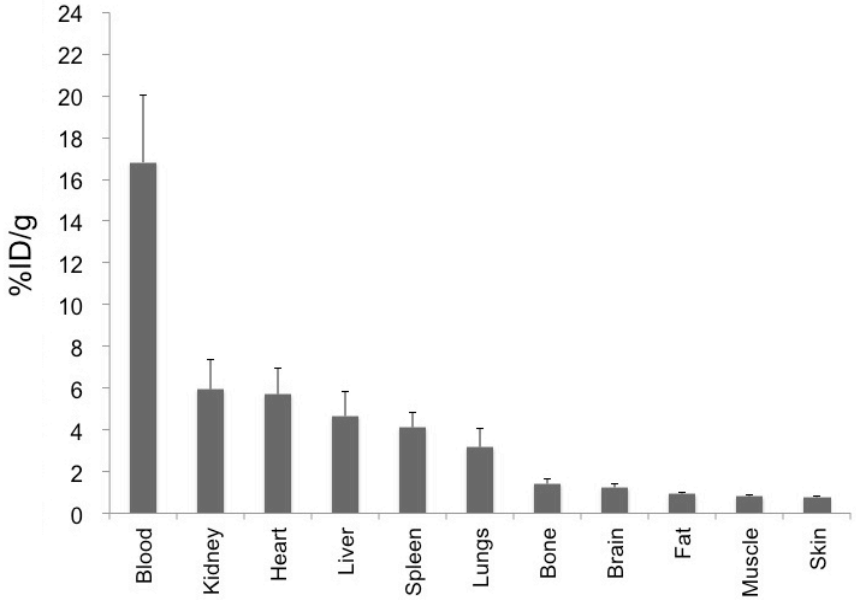

Figure 9: Biodistribution analysis of ^{68}Ga-Fucoidan in mice (n=3) was performed 60 minutes. After intravenous injection, Results are expressed as mean±SD.

LPS enhanced ^{68}Ga-Fucoidan cellular uptakes & Cell viability assessment

Incorporation of ^{68}Ga-Fucoidan into LPS-treated and non-treated bEnd.3 endothelial cells was determined using a high-energy gamma counter. Compared with non-induced endothelial cells, LPS induced cells showed an approximate 2-fold increased uptake of ^{68}Ga-Fucoidan (Fig.10A). The radioactivity incorporation in endothelial cells following a 30 minutes incubation at 37°C varied approximately 35% of the total loaded activity per 106 cells (522 - 546 cpm / 1000 cells). We examined the effect on expression of P-selectin proteins in response to the inflammation inducer LPS. Results showed detectable up-regulation of P-selectin on LPS-induced bEnd.3 cells compared with cells of untreated controls, which were confirmed by western blot (Fig. 10B).

To determine whether Fucoidan is able to induce apoptosis, early passage endothelial cells were incubated with different concentration of Fucoidan in triplicate, the cells were dual-stained with annexin-V-pacific blue and 7aad, subsequently analyzed by flow cytometry. Apoptosis as evaluated by the percentage of cells binding Annexin V and 7-AAD, dead cells ratio is 1.15% without incubation with Fucoidan while 1.73% after incubation of Fucoidan (40 µg/ml) for 48hours. No significantly diminished cell viability was observed (Fig.10 C). In order to determine toxicity of Fucoidan in vivo, we injected intramuscularly a high dose of Fucoidan (5mg/kg/d during 3 weeks) into C57BL/6 mice (n=10), and no detectable side effects were

observed. Therefore, we demonstrated no significant cytotoxic effects were observed in high doses of Fucoidan.

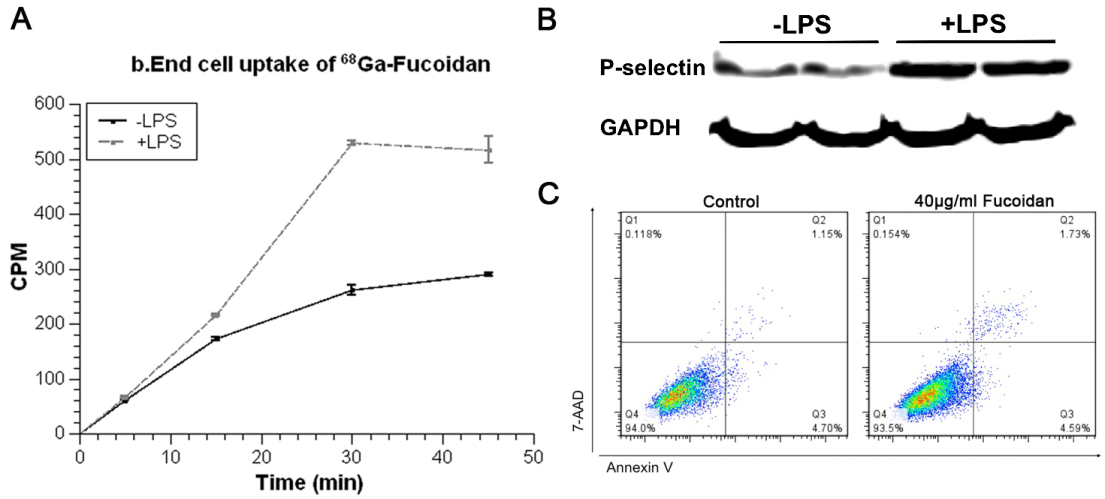

Figure 10: A, Effects of LPS on ^{68}Ga-Fucoidan uptake, ^{68}Ga-Fucoidan uptake were recorded at 5min, 15min, 30min, 45min in bEnd.3 endothelial cells treated with and without LPS (1ug/mL) for 48 hours. B, Western blot of P-selectin protein expressed in LPS-treated (+LPS) and non-LPS-treated (-LPS) cells. GAPDH was used as an internal standard. C, bEnd.3 endothelial cells were incubated with 40 μg/ml Fucoidan. At time point of 48 hours the cells were stained with 7-AAD and annexin V-pacific blue followed by flow cytometry analysis. Representative flow cytometry image of cell apoptosis analysis, 48-hour incubation with Fucoidan did not induce cellular apoptosis (Q1) and necrosis (Q3).

Ex vivo detection of P-selectin expression on atherosclerotic plaques

Pronounced uptake was observed in activated soft plaques, but less uptake in inactivated fibrous plaques, plaque morphology and activity were confirmed by H&E histological and DAB staining, representative autoradiography images are shown in Figure 11. Immunohistochemical staining of adjacent aorta sections indicated an enhanced P-selectin expression in soft atherosclerotic plaques with high-density macrophage interaction, but weaker expression in fibrotic plaques with low-density of macrophage. Enhanced expression of P-selectin and macrophage in the vulnerable soft plaque co-localized with increased uptake of ^{68}Ga-Fucoidan indicated (Fig. 11).

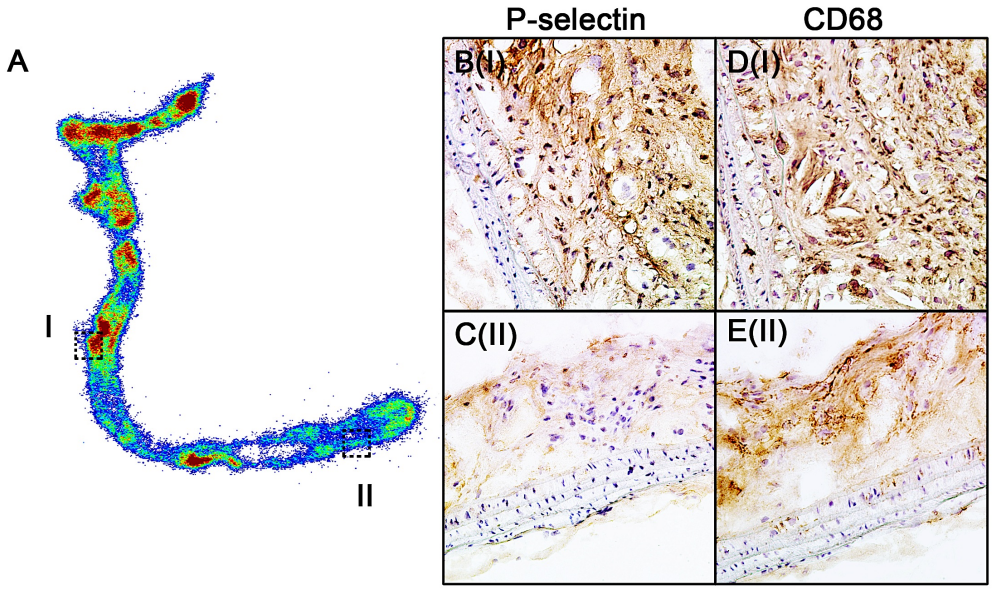

Figure 11: ^{68}Ga-Fucoidan accumulated at high P-selectin expressing and high macrophage density regions within the aorta. A, Representative autoradiographic image of the aorta of an apolipoprotein E-deficient (ApoE-/-) mouse on Western diet for 38 weeks. ROI (I) and ROI (II) were adjusted manually to obtain the SUV. B(I), C(II), DAB staining of P-selectin and D(I), E(II), DAB staining of macrophages (CD68), which are respectively corresponding to the region I and region II in autoradiography. Stronger uptake was visualized at atheromatous plaques (ROI (I)), presenting dense foam cells while weaker uptake at fibrous plaques (RIO (II)).

In the assessment of ex vivo accumulation of ^{68}Ga-Fucoidan of each mouse, 10 tissue sections were analyzed by autoradiography, We studied 280 lesions, (150 activated lipid-rich plaque segments with high-density macrophage, 80 inactivated fibrous plaque segments with lower-density macrophage and 50 non-plaque area with fatty streak or healthy endothelium) which were selected according to histological test. The tracer uptake in activated soft plaque-areas was higher than in inactivated fibrous plaque area ($R=1.73\pm0.3$, $P<0.05$) in each single ApoE-/- mouse, and also significant higher than in the non-plaque endothelial segments ($R=2.35\pm0.4$, $P<0.01$). Acute vascular inflammation model was developed, because endothelial dysfunctions are representatives of early stage and advanced stage of atherosclerosis. In brief, for acute vascular inflammation model, 1 mg/ml LPS in 100 µL PBS was intravenously injected into the C57/6 mice (40 weeks old n=6). Prior to radiotracer injection, mice were exposed to LPS for 24 hours. Ex-vivo autoradiographic assessment were performed to evaluate tarcer's uptake. Higher uptake were observed at LPS-induced mice in comparison to non-induced control mice. (Fig. 12)

Double-immunofluorescence staining revealed P-selectin expression on the endothelium overlaying soft inflamed plaques as indicated by vWF staining, and co-localization with macrophages within the activated plaque (Fig. 13).

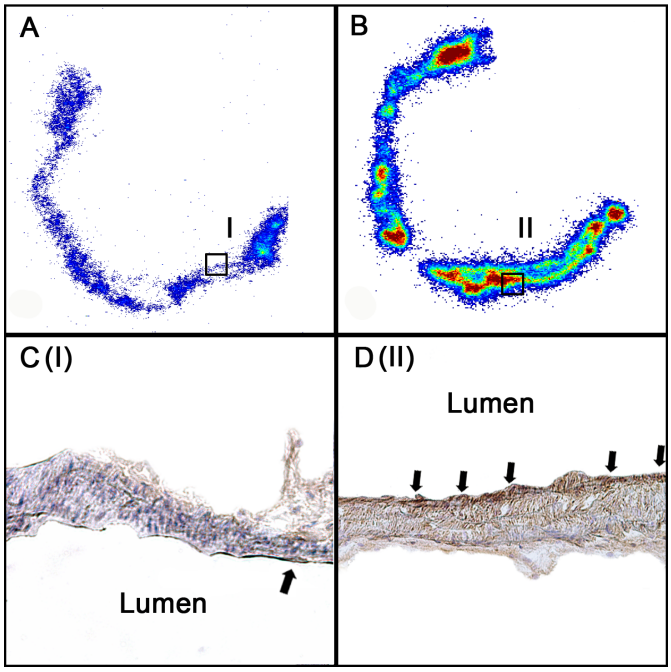

Figure. 12: Representative autoradiography imaging two aortas from non-LPS induced mouse (A) and LPS induced mouse (B). Comparison of P-selectin immunohistological staining. C, D Corresponding DAB staining of section I and section II respectively.

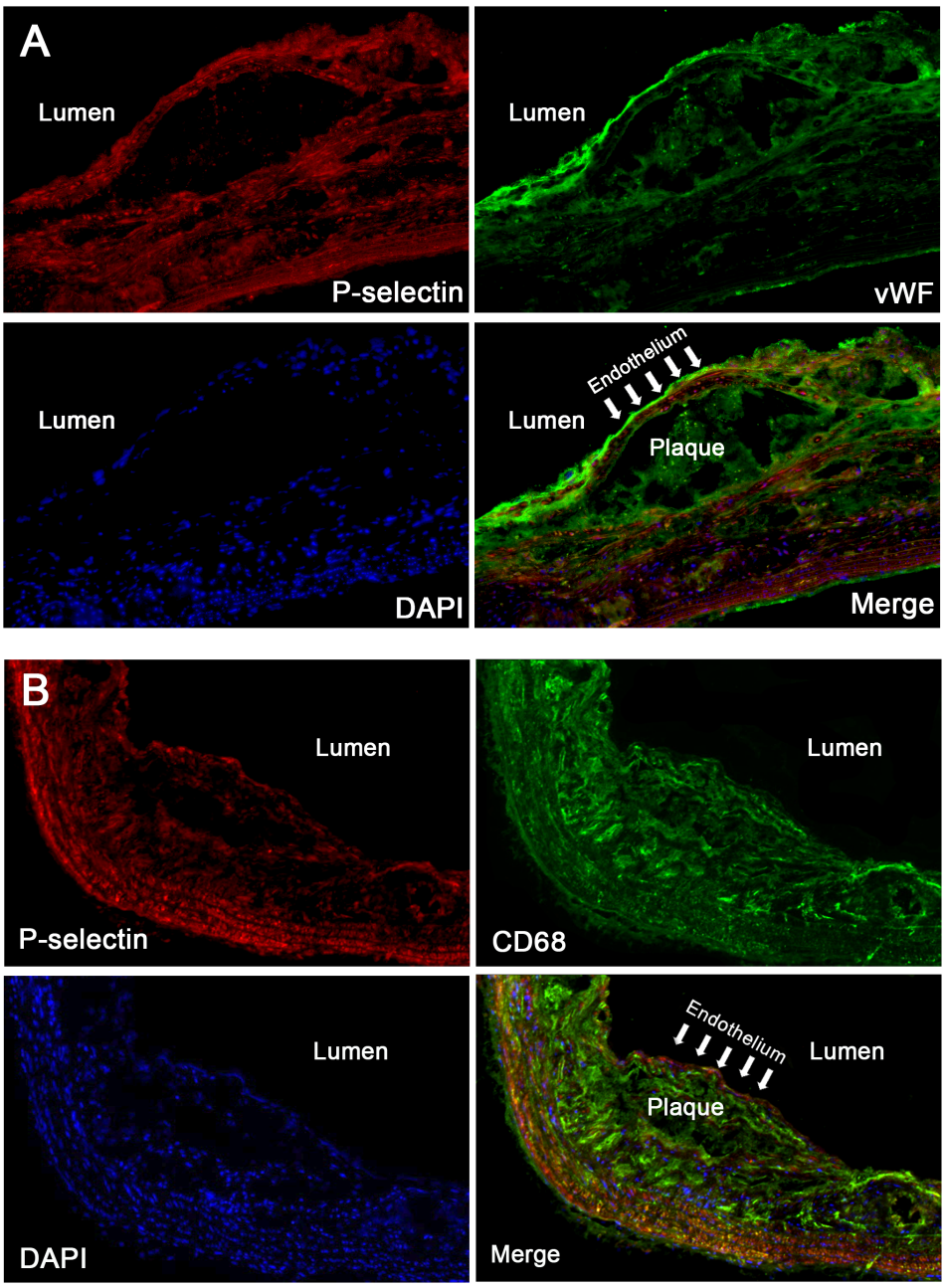

Figure 13: Double staining of a representative thin-capped fibroatheroma with large necrotic core. P-selectin (red) express in the endothelium overlying vulnerable plaque, von Willebrand factor (vWF) (Green) was used to indicate endothelium (A), CD68 staining for expression of macrophage (B); nuclear counterstain with DAPI (blue); Co-localization of P-selectin and vWF on the endothelium (A), and macrophages (CD68) were shown in merged image (B).

In vivo detection of P-selectin expression

Dynamic PET studies determined that the optimum imaging time. Because of high level of radiotracer in the blood, and difficult localization of focal uptake at early time points, PET images (n=10) were acquired by collection of six frames in duration from 50 minutes to over 100 minutes. Subsequent work showed that 60minutes to 70 minutes could be used without significant degradation of the arterial signal. Data from each of the frames is independently (Fig. 14). ROIs were assigned to the aortic arch, ascending aorta, descending aorta, and abdominal aorta on micro-PET images (n=20). Representative micro-PET images showed tracer accumulation in the atherosclerotic lesions at coronal view matching the Sudan IV staining (Fig.14).

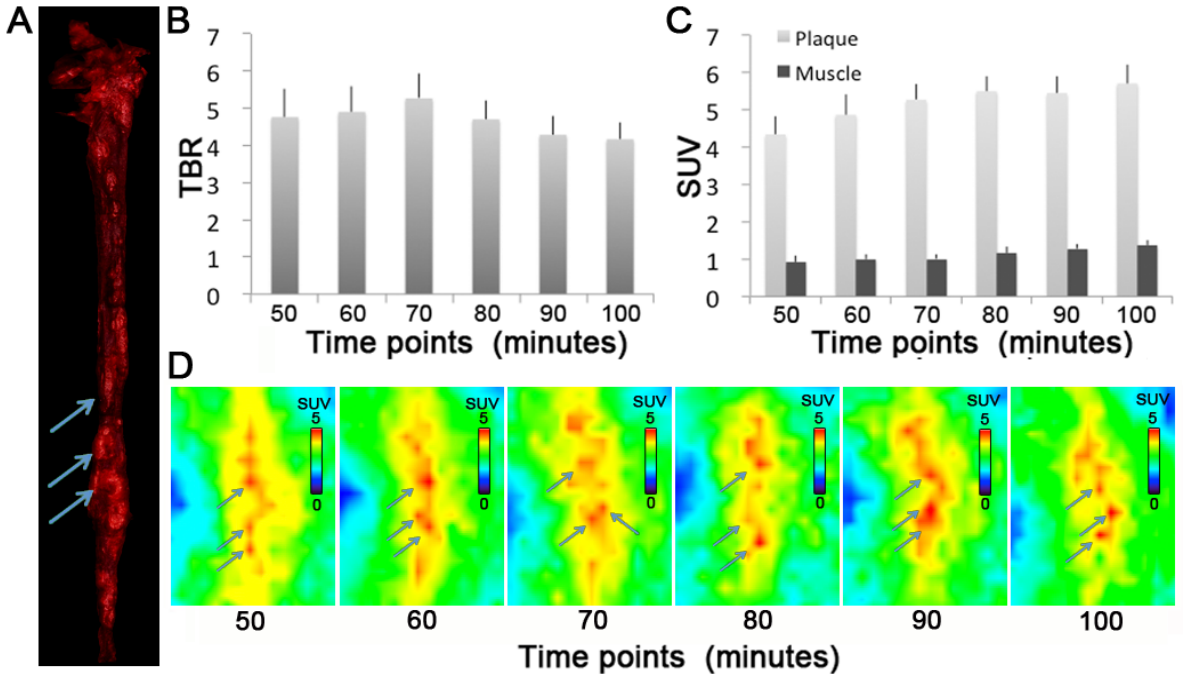

Figure 14: A, Representative atherosclerotic aorta of apoE$^{-/-}$ mouse fed with western diet for 40 weeks, micro PET images (six frames) were obtained from time points 50 minutes to 100 minutes after injection A. the presence of neutral lipid within the plaque were assessed by enfaces staining with Sudan IV. Arrows indicate neutral lipid stained plaques. B, The mean of target to background ration (TBR) value of aortal focal uptake at all time points, data are given as mean±SD. C, Mean standardized uptake value (SUV) of aortal focal uptake and leg muscle at all time points, data are given as mean±SD. D, Micro PET image shown obvious aortal uptake from time point 50 minutes to 100 minutes after injection, arrow indicate plaque and corresponding uptake of ^{68}Ga-Fucoidan. Arrow signifies the presence of accumulation of ^{68}Ga-Fucoidan at plaque.

Clear localized focal uptake of ^{68}Ga-Fucoidan at time points of 60 minutes was detected in all apoE-/- mice with SUVmean=5.1±0.5, SUVmuscle=1.0±0.2, and TBRmean =5.1±0.8. The specific accumulation of radiotracer at atherosclerotic plaques was also correlated with histological lipid staining, noninvasively with 17.6T MRI. The representative micro-PET, high-resolution MRI and autoradiography of aorta arch section showed a good agreement between uptake of ^{68}Ga-Fucoidan and plaque vulnerable morphology (Fig. 15). No specific vascular uptake was detected at control mice. Significant uptake in the myocardium was observed in all apoE-/- mice. Further representative noninvasive images of brachiocephalic artery section are given in the figure 16.

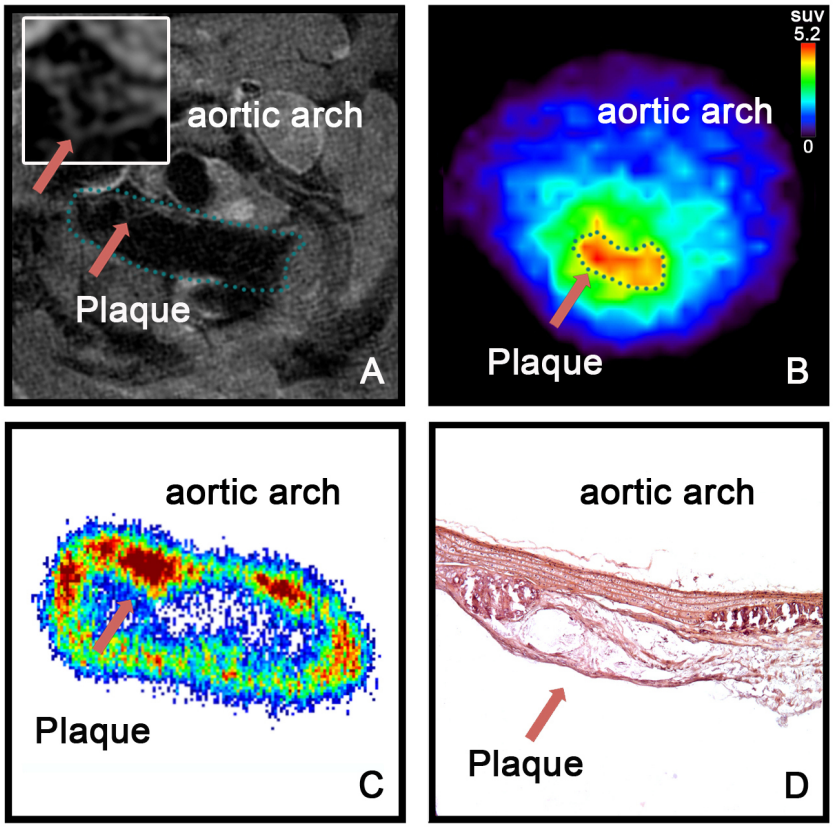

Figure 15: Representative noninvasive images, aortic arch from an ApoE$^{-/-}$ mouse on Western diet for 38 weeks. All red arrows indicate regions of interest. In vivo ultra-high-field MRI of the aortic arch using an ECG-triggered Multi-Slice-Multi-Spin-Echo sequence. Micro-PET imaging at transverse view suggesting specific uptake of ^{68}Ga-Fucoidan by the plaque. Corresponding autoradiography image of the aortic arch. H&E staining of corresponding plaque section. Thin cap (bright outer layer), large lipid core (dark inner part) and calcification (bright inner part) of plaque were characterized on MR images and histology, whereas in accordance with high uptake of ^{68}Ga-Fucoidan confirmed by micro-PET and autoradiography.

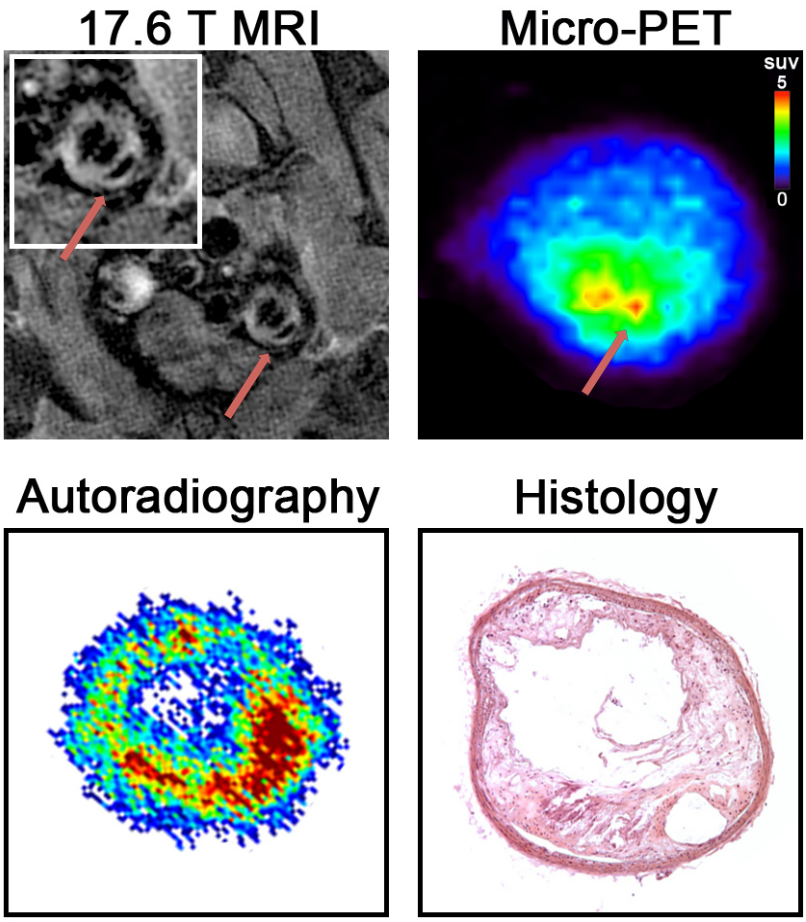

Figure 16: Representative noninvasive images, brachiocephalic trunk from an ApoE$^{-/-}$ mouse on Western diet for 38 weeks. All red arrows indicate regions of interest. A, In vivo ultra-high-field MRI of the aortic arch using an ECG-triggered Multi-Slice-Multi-Spin-Echo sequence.B, Micro-PET imaging at transverse view suggesting specific uptake of ^{68}Ga-Fucoidan by the plaque. C, Corresponding autoradiography image of the aortic arch. D, H&E staining of corresponding plaque section. Thin cap (bright outer layer), and large lipid core (dark inner part) of plaque were characterized on MR images and histology, whereas in accordance with high uptake of ^{68}Ga-Fucoidan confirmed by micro-PET and autoradiography.

In vivo and ex vivo blocking studies

Receptor blockage using sLe^x the nature ligand of P-selectin resulted in a significant decrease of tracer accumulation in aorta sections from apoE$^{-/-}$ mice, which indicated that the accumulation of the radiotracer was especially mediated by cellular P-selectin expression. The signal intensities characterized by TBR were significantly decreasing ($p < 0.01$) from 5.2 ± 0.7 with no inhibition to 2.6 ± 0.4 with inhibition. Strong decrease at plaque was observed after incubation of sLe^X on atherosclerotic aorta sections. This blocking effect was obvious on the corresponding in vivo (Fig. 17) and ex vivo images (Fig.18)

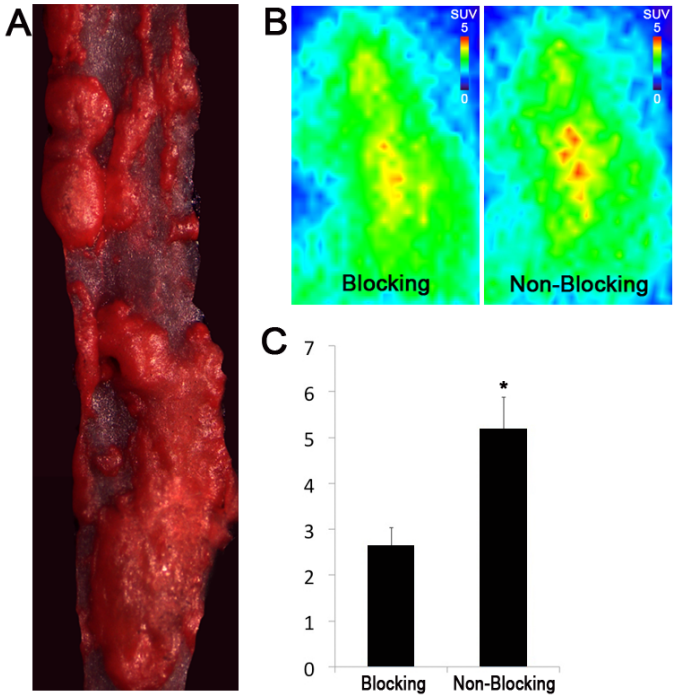

Figure 17: Representation of Monitoring P-selectin inhibition by sLe^X using 68Ga-Fucoidan. A, Sudan IV staining of aorta lesion of an ApoE-/- mouse fed with western diet for 40weeks, demonstrating plaque development along aorta. B, ^{68}Ga-Fucoidan PET image of aorta lesions from ApoE-/- with severe plaque with (left) and without (right) pre-incubation of overdose sLe^X. C, Uptake value at 60 minutes at atherosclerotic aorta with and without P-selectin inhibition. Data are given as mean±SD (n=6). *P<0.05.

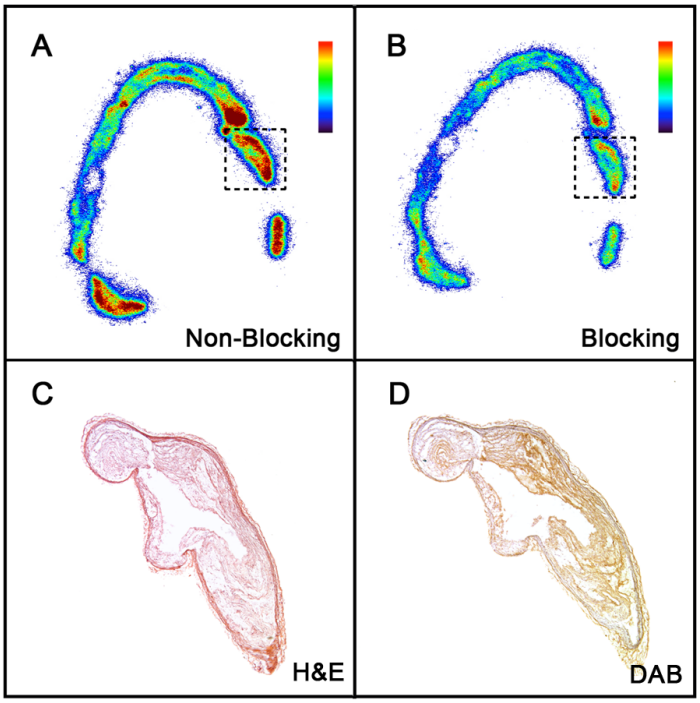

Figure 18: Pre-incubation of sLe^x target to P-selectin inhibited uptake of ^{68}Ga-Fucoidan in atherosclerostic plaques from ApoE-/- mice. A, B, Autoradiography images show the lower uptake in the

aorta pre-incubated with P-selectin targeted antibody. Histology demonstrated the co-localization of atherosclerotic plaque with the area of increased ^{68}Ga-Fucoidan uptakes by (C) H&E staining and (D) DAB staining of P-selectin.

4.3 DISCUSSION

4.3.1 ANIMAL STUDY I: Macrophage characterization of atherosclerosis: ^{68}Ga-DOTATATE ex-vivo detection in mice

Atherosclerosis is a systemic inflammatory disease, knowledge about the macrophage content on plaque is especially important to evaluate atherosclerosis. In the present investigation, we tested ^{68}Ga-DOTATATE an SSTR-affinity radiotracer in a number of *ex* and *in vitro* experiments aiming to investigate the tracer's uptake in atherosclerotic plaques on a tissue level, examining, whether this tracer is able to detect atherosclerotic lesions and determine macrophage localization. In our previous study, a stronger association of increased ^{68}Ga-DOTATATE uptakes with risk factors for cardiovascular disease as compared with ^{18}F-FDG in oncological patients suggested a potential role of ^{68}Ga-DOTATATE for plaque imaging in the large arteries (130). However, until now confirmation of a specific tracer uptake on a tissue level was lacking. Therefore, ApoE-/- mice, the most commonly used animal model of atherosclerosis were investigated. In this study, we compared the autoradiographic findings with histological and immunochemical results. We observed that the areas of high ^{68}Ga-DOTATATE uptake colocalized with atherosclerotic plaque on excised aortas. Aorta was selected but not coronary artery or aortic root, which are more hazardous and prone to develop atherosclerosis; since several unspecific myocardial uptakes were also observed, which possibly could affect imaging. The significant decrease of ^{68}Ga-DOTATATE uptakes on autoradiographic imaging after pre-incubation of the slices with an antibody against SSTR-2, is indicative if a high specificity of tracer for SSTR-2 in the vessel wall. A previous study reported that the SSTR-2-mRNAs could be detected in macrophages(114). In the current study, we found significant expression of SSTR-2 on monocyte/macrophages as well by flow cytometry. Additional, SSTR-2 were also detected on the T-cells that are nonetheless important in regulating immune response and expressed significant at atherosclerotic lesions. In addition, LPS-activated and non-activated macrophages were studied to assess the effect of an inflammatory stimulus on the expression of SSTR-2. LPS was chosen as a stimulating factor because it is a specific activating factor with immunostimulatory effect(131). When macrophages were stimulated with LPS, no different expression of SSTR-2 which is in keeping with a previous study showing that SSTR-2 mRNA of human macrophage was not up-regulated by LPS(114). Conversely, another study demonstrated that significant up-regulation of SSTR-2 in LPS-activated human macrophages (113). The cause of this inconformity is unclear, a difference in the duration of the stimulation may contribute to this discrepancy. From

this point of view, ^{68}Ga-DOTATATE PET imaging is not able to assess the activation of macrophage, but just detects their presence. However, It is also commonly known " vulnerable plaques" have a high density of macrophages; detection of those macrophages therefore may play an important role in imaging vulnerable plaques. Both a previously published study using human coronary endothelial cells and our data on murine endothelial cells demonstrated that SSTR-2 is significantly expressed on endothelial cells, however this expression is decreased by the treatment with inflammatory cytokine TNF-a, which is mainly produced and secreted by activated macrophages.(132) Additionally, in our study significant stronger uptakes at plaque area were detected than non-plaque area. We also prove, that ^{68}Ga-DOTATATE may be used to assess macrophages within arterial walls. This is the first report directly demonstrating a high affinity of ^{68}Ga-DOTATATE to macrophage-rich atherosclerotic plaques.. Therefore, ^{68}Ga-DOTATATE has the potential to evaluate vascular macrophage density by detecting SSTR-2 in humans. However, further investigations are needed to confirm the potential of ^{68}Ga-DOTATATE-PET as tool for molecular imaging of macrophage clinically.

Limitation

The in vitro results require animal PET/CT imaging to localize the plaque sites and prove the association between in vivo and in vitro study. The ^{68}Ga-DOTATATE PET seems to be an efficient modality for detecting vascular inflammation, but the uptake of radiotracer does not reflect the morphology accurately. Moreover, though the activation of the inflammation could decrease the expression of SSTR-2 on endothelial cells, that can influence accurate evaluation of vascular uptake, ^{68}Ga-DOTATATE PET could be recognized as a supplemental method for evaluation of vulnerable plaque base on the examination of plaque morphology. In our study, all mice were investigated at long-term point, In order to evaluate the sensitivity of ^{68}Ga-DOTATATE, more investigations of early-stage atherosclerosis imaging are also required to be performed. Further correlative studies need to be performed in humans. Also, in this study, female ApoE knockout mice were used, which are known to be less affected by atherosclerosis than their male littermates. However, also due to the special diet, we observed severe atherosclerotic changes also in the female animals in this study.

4.3.2 ANIMAL STUDY II: Targeting P-selectin expression in vulnerable plaques by Gallium-68 labeled Fucoidan PET: Correlation with in vivo 17.6T MRI

In spite of many efforts and great advances in technology, the detection of vulnerable plaque at risk of rupture still remains challenging. More sensitive and specific contrast agents are required for accurate diagnosis and to guide therapy. Regardless of all imaging modalities, it is important to distinguish stable plaques with a low extracellular lipid (types I–III) from vulnerable high macrophage-density plaques (types IV and Va), which are dangerous because of their high risk of rupture and risk of acute thrombosis (133,134). Increased P-selectin expression has been found in vulnerable atherosclerotic plaques; whereas fibrotic stable plaques are lacking pronounced P-selectin expression. Thus, noninvasive detection of up-regulation of P-selectin on activated endothelium could become an effective tool to evaluate the risk of atherosclerosis and thrombosis in reducing atherosclerotic lesion development and preventing acute cardiovascular events. sLe^X-like glycan, which is nature ligand of P-selectin (135) and strongly expressed in circulating leukocytes was selected as imaging probe (136). As naturally occurring mimic of sLe^X, Fucoidan holds great clinical and investigation potential with superiority of low cost.

In this study, we described for the first time to our knowledge a P-selectin affinity PET tracer, Gallium-68 labeled Fucoidan, as a promising imaging probe to visualize murine atherosclerosis. First, we established an efficient and rapid synthesis of ^{68}Ga-Fucoidan, which could be applicable for potential clinical uses. ^{68}Ga-Fucoidan was obtained in an overall decay-corrected reaction yield of 90±5% and 99% radiochemical purity in a total synthesis time of 40 min. The preparation of ^{68}Ga-Fucoidan was reproducible in providing one stable product, as shown by radio-HPLC and radio-TLC analysis up to 4h (equivalent of 3.5 x half-lifes of ^{68}Ga) after preparation.

^{68}Ga-Fucoidan was assessed *in vitro*, *ex vivo and in vivo* respectively. We found that the ^{68}Ga-Fucoidan specifically accumulates at unstable plaques with high-density macrophage infiltration, but much less at fibrous plaques with low-density macrophage presence assessed by autoradiography. In micro-PET study, high specificity and sensitivity were confirmed by strongly pronounced uptake at aortic atherosclerotic region with high target to background ratio at time point of 50 minutes post injection.

Numerous imaging technologies such as MRI and SPECT were previously developed to detect P-selectin as well. PET as a method is more suitable to detect pathologies on a

molecular basis than MRI further more, it has a superior spatial resolution as compared to SPECT. In MRI studies, imaging of atherosclerotic endothelium with low-concentrated superparamagnetic agents in a low magnetic field was found to be challenging (122). Recently, Rouzet et al. reported on a new SPECT tracer, ^{99m}Tc-Fucoidan, which was developed to detect P-selectin's upregulation in two different animal models of myocardial ischemia reperfusion injury and platelet-rich thrombus (137). In this study, a good targeting efficiency of ^{99m}Tc-Fucoidan was confirmed. Focal uptake of ^{99m}Tc-Fucoidan was found in all mice with endothelial activation with an uptake ratio of 4.1. Although ^{99m}Tc-fucoidan possesses great practical advantages because of clinical availability of SPECT scanners, due to the inherent limitation of lower spatial resolution of SPECT imaging, especially in the context of imaging small structures like atherosclerotic plaques, and another reason of current development of PET/MRI scanners and superiority of absolute quantitation, Fucoidan-based PET tracer might be able to enhance the clinical implication. Overall, ^{68}Ga-Fucoidan PET imaging holds sensitive, specific, economic capability improving its potential to be used as a clinical agent in the future.

In comparison to other potential radiotracers for the identification of plaque vulnerability, ^{68}Ga-Fucoidan might be superior; ^{18}F-FDG is the most common applied radiotracer in pre-clinical studies of atherosclerotic plaques. However, high myocardial and brain uptake of ^{18}F-FDG remains a major drawback, if coronaries or brain vessels need to be assessed (130). In our previous studies, aorta uptake of ^{68}Ga-DOTATATE, a macrophage affinity radiotracer, likely shows greater specificity to the vascular inflammation related to ^{18}F-FDG (127,130). Because P-selectin expression is closed associated with increased macrophage infiltration into plaque, further correlation between ^{68}Ga-DOTATATE PET, ^{18}F-FDG PET and ^{68}Ga-Fucoidan would be of great interest. In addition, Matrix-digesting enzyme (MMPs 2, 3, 9, etc) in the fibrous cap also play vital role in rupture of plaque, MMPs secreted by macrophages , are specific indicators of the macrophage activity rather than only macrophage density. Noninvasive quantification of MMP activity in atherosclerotic plaques by PET or SPECT has been already published in preclinical models (138,139). Massive P-selectin migrates from an inner cell to the endothelial surface in response to the inflammatory mediators inducing (140). Therefore, P-selectin and MMPs PET have specific superiority to detect inflammatory activity of plaques. In previous work, PET imaging of other adhesion molecules for atherosclerosis detection were investigated. Resembling P-selectin, VCAM-1 expresses in the early progress of atherosclerosis, and is favorably localized on endothelial cells overlying on inflamed plaque as well. Likewise, Matthias et al (141) developed a new PET tracer ^{18}F-4V for characterization of vascular cell adhesion molecule 1 (VCAM-1) on atherosclerotic apoE-/- mice and wild type mice with myocardial infarction and heart transplant rejection. In addition, they used PET/MRI to investigate signaling pathways of monocytes and their progenitors after therapy of

myocardial infraction in atherosclerotic mice with myocardial infraction. RNAi silencing therapy of the chemokine receptor CCR2, that is able to inhibit the recruitment of monocyte (56).

We analysised 10 mice dynamically 50 – 100 minutes post injection of the radiotracer and binned the data into time frames of 10 minutes each. The absolute values of tracer uptake as expressed by SUV seems to slightly increase over that time period (see new Fig 23, however, also the background slightly increased, potentially because of minor P-Selectin expression in the muscle. All in all the TBR did not change a lot over time; there was a tendency for a decrease after 70 minutes. Visually the delineation of the plaques did not improve of time (see Fig. 5). Therefore we selected 60 minutes as the time point for evaluation (also because of better count statistics and less noisy images using a tracer with a half-life of only 68 minutes). Also in later time points bad count statistics may mimic focal tracer uptake in the vessels. Our ApoE-/- model have severe atherosclerosis, with 70% or greater luminal stenosis, and due to limitation of PET imaging resolution, It become difficult to accurate localize blood pool in the lumen of the vena cava. However, the in vivo PET imaging showed corresponding strong focal uptake of advanced plaque lesions. Signals from blood pool adjunct to plaques are also positive but lower than plaque signals, due to the promising results of this study the next potential study is to move into larger animals like rabbits. Unfortunately, the relatively short half-life of 68-Galium doesn't enable delayed imaging time point for yielding better blood clearance, Should the slow blood clearance be noted again, a switch to another radionuclide like copper-64 may result in better plaque-to-blood ratios, because imaging at later time points would then be feasible.

We developed an efficient, rapid and economic synthesis strategy. The fairly easy synthesis would make it easy to apply the radiotracer clinically. The pharmacologic effect of fucoidan processing anti-inflammation and antithrombotic impact was approved (142,143). In our study, toxicity of Fucoidan extracted from algae was assessed. The specificity of ^{68}Ga-Fucoidan was confirmed by in vivo micro-PET imaging with low background signal, receptor blocking study and biodistribution analysis. The reason we used the SUV in muscle instead of blood pool to calculated TBR is because inherent limitation of long blood half-life. However, clear uptake at vascular wall was observed at many aortal segments. So far, no reliable method exists to reliably detect early inflammatory atherosclerotic lesions (type I, II, III and IV) (144). Within early atherosclerosis-prone regions of the vasculature, activated endothelial cells express P-selectin as well. It is thought to be an effective marker to assess the processes in early atherosclerotic endothelial dysfunction (120,145-148) Additionally, expression of P-selectin is increased on activated platelets during vascular thrombus formation, which is subsequent for growth and stabilization of the thrombus by forming large stable platelet-leukocyte complexes (140,148). Since P-selectin plays an important role in cardiovascular inflammation and

hemostasis, a validated ^{68}Ga-Fucoidan-PET imaging also holds promising potential in various clinical cardiovascular settings, such as thrombosis, myocardial ischemia and evaluation for ischemic injury therapies. Consequently, and early detection of the specific up-regulation of cardiovascular P-selectin could help to reduce the risk to numerous advanced events. However, imaging coronary artery atherosclerosis presents special challenges. These arteries are smaller than the PET resolution; in our study, unspecific myocardial accumulation of ^{68}Ga-Fucoidan is not confirmed, either from cardiac endothelium or coronary artery needs requires more symmetric assessments in coming studies.

Limitations

Due to high inherent sensitivity, PET imaging holds superiority in detection the diseased lesions as small as atherosclerotic plaques, but lacking of structural information. Combinations with computed tomography (CT) or MRI have a great potential to assess both the activity and the anatomic details of diseases. Therefore hybrid scanners such as PET/MRI or PET/CT, which should be used for further preclinical and clinical studies. Additionally, to adequately reflect the real situation, ApoE-/- mice at young age, which are at early stage of atherosclerosis are also significant for the study. ^{68}Ga-Fucoidan in detection of early dysfunctional endothelium needs to be investigated. Furthermore, in our study, ^{68}Ga-Fucoidan PET show promising capability helping to recognize the activated plaques in ApoE-/- mice model. Nevertheless, these plaques are not going to rupture, which can cause thrombosis. Long blood half-life of radiotracer is an inherent limitation in plaque imaging. Consequently, capability of ^{68}Ga-Fucoidan on detection of more severe cardiovascular events such as thrombosis, myocardial ischemia is holding greater promising to assess.

4.4 Conclusion

In conclusion, we evaluated two PET tracers: ^{68}Ga-DOTATATE and ^{68}Ga-Fucoidan on vascular inflammation of atherosclerosis. ^{68}Ga-DOTATATE show specific affinity to infiltrated macrophage within the plaques. ^{68}Ga-Fucoidan may hold the potential to discriminate between active and inactive atherosclerotic plaques in terms of variant accumulation on different-types of plaques.

5. PATIENT STUDY

^{68}Ga-DOTATATE PET/CT for the detection of inflammation of large arteries: correlation with ^{18}F-FDG, calcium burden and risk factors

(This patient study is based on the data analysis from routine oncology patients.)

5.1 Materials and Methods

Patients

A total of 16 patients (12 males and 4 females, age ranges from 48 to 77 years, mean age was 63.5 years) were retrospectively reviewed by two experienced nuclear medicine physicians. The patients were referred to the department of Nuclear Medicine for pre-therapeutic ^{68}Ga-DOTATATE-PET/CT diagnosis to ascertain the presence of a hypermetabolic neuroendocrine tumour prior to radionuclide therapy with ^{177}Lu-DOTATATE. Intraclass correlation coefficients, along with 95% confidence for inter- and intra reader were shown in table 4. These patients had undergone both ^{68}Ga-DOTATATE PET/CT and ^{18}F-FDG PET/CT for staging or restaging within 6 weeks (mean, 3.8 weeks; range, 0.14 to 5.9). None of these patients received steroids or had a recent history of inflammation or vasculitis.

Table 4. Intraclass correlation coefficients, along with 95% confidence for inter- and intra reader.

ICC values using the maximum TBR Measurement (^{18}F/^{68}Ga)								
Parameter	Left carotid	Right carotid	Aortic arch	Descending	Ascending	Abdominal	Left iliac	Right iliac
Inter-reader Agreement (^{18}F)	0.92 (0.90, 0.99)	0.93 (0.83, 0.98)	0.97 (0.95, 0.99)	0.9 (0.74, 0.96)	0.95 (0.94, 0.97)	0.94 (0.90, 0.97)	0.92 (0.84, 0.97)	0.89 (0.87, 0.93)
Inter-reader Agreement (^{68}Ga)	0.94 (0.88, 0.99)	0.96 (0.91, 0.99)	0.98 (0.97, 0.99)	0.95 (0.90, 0.97)	0.96 (0.93, 0.98)	0.98 (0.97, 0.99)	0.91 (0.86, 0.95)	0.91 (0.80, 0.97)
Intra-reader Agreement (^{18}F)	0.9 (0.70, 0.97)	0.82 (0.60, 0.94)	0.95 (0.86, 0.98)	0.84 (0.66, 0.95)	0.89 (0.69, 0.96)	0.97 (0.92, 0.99)	0.88 (0.67, 0.96)	0.82 (0.58, 0.93)
Intra-reader Agreement (^{68}Ga)	0.81 (0.51, 0.91)	0.89 (0.68, 0.97)	0.96 (0.87, 0.99)	0.97 (0.91, 0.99)	0.85 (0.68, 0.95)	0.9 (0.70, 0.97)	0.87 (0.63, 0.96)	0.89 (0.71, 0.96)
Data in parentheses are 95% confidence intervals								

PET/CT imaging

All patients underwent ^{18}F-FDG PET/CT and ^{68}Ga-DOTATATE PET/CT on a dedicated PET/CT scanner (Siemens Biograph ® mCT 64), consisting of a LSO full-ring PET and a 64-slice spiral CT. On the day of ^{18}F-FDG PET imaging, patients fasted for at least 6 h to assure a serum glucose level below 130 mg/dL. At the time point of intravenous injection of 4.18±0.88 MBq per kg bodyweight, patients received 10 mg of furosemide i.v.. After an uptake period of 80-90 minutes, transmission data were acquired using a low-dose CT (30 mAs, 120 kV, a 512 × 512 matrix, a 5-mm slice thickness, an increment of 30 mm/s, a rotation time of 0.5 s, and a pitch index of 0.8) extending from the base of the skull or the vertex to the proximal thighs. Consecutively, PET emission data were acquired in 3-dimensional mode with a 200 × 200 matrix with 2 minutes emission time per bed position. After decay and scatter correction, PET data were reconstructed iteratively with attenuation correction using dedicated software (HD.PET, Siemens Esoft).

For the assessment of somatostatin receptor expression, a mean dose of 1.29±0.43 MBq ^{68}Ga-DOTATATE per kg bodyweight was injected intravenously. After a period of 40-60 min, CT and PET data acquisition was started using the same parameters as mentioned above.

Image analysis

All PET/CT scans were reviewed for anatomic localization and amount of focal tracer uptake. In each patient, 8 segments of large arteries were analyzed: left carotid artery, right carotid artery, ascending thoracic aorta, aortic arch, descending thoracic aorta, abdominal aorta, left and right iliac artery.

Arterial calcifications were also assessed, vascular attenuation of >130 Hounsfield units were rated as calcification. The plaque burden was semiquantitatively determined by assessing the maximal dimensions and composition of plaque using a scoring system from “0” to “4”(Table 5).

Table 5. Calcified plaque scoring system

Score	Calcified occupation of the vessel circumference
0	0%
1	< 10%
2	10–25%
3	25–50%
4	>50%

The total calcified plaque burden for each of the eight arterial segments was defined as the sum of the individual calcified plaque scores

For PET data analysis, a ROI-based approach was chosen. Maximal “standardized uptake values” (SUVmax) for both ^{18}F-FDG and ^{68}Ga-DOTATATE uptake were calculated for all segments. Areas in proximity to tumor lesions or organs with a high physiological tracer uptake, i.e. the liver, were carefully avoided. At least three fixed-size regions of interest (ROIs) were placed to cover the lumen at each site, and the highest value was extracted for the final calculation of target-to-background ratios (TBR) Background was defined as the average blood-pool uptake as determined by the mean SUV of six different ROIs (diameter of 1 cm) within the lumen of the vena cava. The SUVmax was divided by the mean blood-pool SUV in order to obtain the TBR (149). We used TBRs of all eight arterial segments for the final analysis. To determine whether sites of increased focal uptake of ^{18}F-FDG and ^{68}Ga-

DOTATATE colocalize, the sites with the highest uptake (within about 30% of the highest uptake value) were assessed. Accordingly, arbitrary cut-off TBR values of 3.5 for ^{68}Ga-DOTATATE and 2.1 for ^{18}F-FDG were chosen, resulting in thirty-seven foci of increased ^{68}Ga-DOTATATE uptake and thirty-nine foci of increased ^{18}F-FDG uptake. Each of these foci was visually assessed for the presence of concordantly increased focal uptake of the other tracer and for presence of calcifications in the vessel wall.

We also assessed the differential vascular uptake of the two tracers in a low-risk group for CAD defined as subjects with no more than 1 cardiovascular risk factor (n=8) and a high-risk group with at least 2 cardiovascular risk factors (n=8). For ROI assignment, visualization of PET/CT images and automated coregistration of the two PET/CT datasets, dedicated software (TrueD, Siemens Healthcare) was used.

Statistical methods

Statistical Package for Social Sciences (SPSS version 11.0; SPSS Inc.) was used for statistical analyses. Continuous variables with a normal distribution were recorded as mean ± standard deviation (SD). The site-specific blood-pool activities of the two tracers were compared using ANOVA. Pearson correlation coefficients were used for the assessment association between uptake of the two tracers and presented cardiovascular risk factors: plaque burden; hypercholesterolemia; hypertension; smoking; diabetes; family history; history of cardiovascular disease; BMI; age and gender. Moreover, intra-class correlation coefficients (ICCs) with 95% confidence intervals were calculated to test interobserver and intraobserver agreement for TBR. Two-way random ICC values which are greater than 0.8 are accepted as a measure of excellent reproducibility.

5.2 Results

Patient population

Relevant baseline characteristics of the patients are reported in Table 6, In brief, 8 out of 16 patients had a history of neuroendocrine tumors, three suffered from thyroid cancer and the remaining 5 patients had different carcinomas. Systemic tumor therapy preceding imaging for less than 12 weeks was administered in four patients. Detailed information on tumor types, therapies and cardiovascular risk factors can be found in Table 7. All risk factors were recorded in Table 8.

Table 6. The total calcified plaque burden for each of the eight arterial segments was defined as the sum of the individual calcified plaque scores

Age (yrs)	63.5±8.8
Gender (M/F)	4/12
Hypercholesterolemia (%)	31.25
Hypertension (%)	56.25
Smoking (%)	25
Diabetes mellitus (%)	12.5
Family history of CAD(%)	25
History of CVD (%)	18.75
CPB	9.44±8.07
CVD cardiovascular disease; CPB calcified plaque burden	

CAD: coronary artery disease; CVD: cardiovascular disease; CPB: calcified plaque burden; F: female; M: male

Table 7. Diseases information of Patients

Nr.	Cancer type	Systemic tumor therapy within the last 3 months	Number of selected positive-uptake segements		TBR_mean	
			FDG	TATE	FDG	TATE
1	renal cell cancer	none	8	6	2.9	5.6
2	follicular thyroid cancer	TSH suppressive therapy	7	2	2.6	3.3
3	pheochromocytoma, metabolically active (normetanephrines, dopamines)	none	3	4	2.1	3.9
4	cancer of the gastric-esophageal junction	xeloda, single dose 2 days prior to ^{18}F-FDG -, 6 days prior to DOTATATE-PET	0	0	1.5	1.8
5	NET (stomach)	none	0	0	1.7	2.2
6	NET of unknown primary (liver metastases)	none	6	3	2.2	3.4
7	carcinoid (rectum)	one cycle of Lu-177-DOTATATE 8 weeks prior to ^{18}F-FDG -, 9 weeks to DOTATATE-PET	0	1	1.7	2.9
8	NET of unknown primary (liver metastases)	none	5	2	2.1	2.9
9	NET (pancreas)	one cycle of cisplatin/etoposide 1 week after ^{18}F-FDG; 4 weeks prior to DOTATATE-PET)	2	1	1.8	2.4
10	carcinoid (lung), hormonally active	none	1	2	1.7	2.6
11	NET of unknown primary (liver metastases)	Sandostatin LAR, last injection 4 weeks prior to DOTATATE-PET, then stopped	0	0	1.5	2
12	NET (ileum)	none	2	1	1.7	2.8
13	NSCLC	none	1	8	1.8	5.7
14	papillary and follicular thyroid cancer	TSH suppressive therapy	2	4	1.9	3.5
15	follicular thyroid cancer	TSH suppressive therapy	2	3	1.9	3.1
16	uterine cancer	none	0	0	1.4	1.3

NET: neuroendocrine tumor; NSCLC: non-small cell lung cancer; TSH: thyroid-stimulating hormone.

Table 8. Risk factors of patients

Patient NO.	Risk facors (Y/N)									
	PB	**Hyperchol**	**HTN**	**Smoke**	**DM**	**Fam Hist. of CVD**	**CVD**	**Age**	**Gender**	**BMI**
1	13	Y	Y	Y	Y	N	N	73	M	38.06
2	4	N	Y	N	N	N	N	63	M	19.82
3	8	N	Y	N	N	N	N	66	M	26.59
4	1	N	N	Y	N	N	N	48	M	22.15
5	0	N	N	N	N	Y	N	56	M	28.6
6	7	N	Y	N	Y	Y	Y	77	M	24.86
7	11	N	N	N	N	Y	N	58	M	21.16
8	12	N	Y	Y	N	Y	N	64	M	24.76
9	1	N	Y	N	N	N	N	51	F	20.57
10	12	Y	Y	Y	Y	N	N	52	M	28.36
11	0	N	N	N	N	N	N	71	F	20.08
12	25	N	Y	Y	N	N	Y	61	M	24.22
13	27	Y	Y	Y	N	N	Y	74	F	20.06
14	12	Y	Y	N	N	N	N	72	M	34.14
15	5	N	Y	N	Y	N	N	63	M	26.58
16	13	Y	N	N	N	N	N	67	F	16
PB: plaque burden; HTN: hypertension; Hyperchol: hypercholesterolemia; CVD: cardiovascular disease;										
BMI: body mass index. NS: no significance, DM: diabetes mellitus										

PET/CT imaging

When assessing the PET/CT image data we found colocalized uptake of both tracers (Fig. 19) as well as foci of increased uptake of only one of the tracers (Fig. 20 + 21).

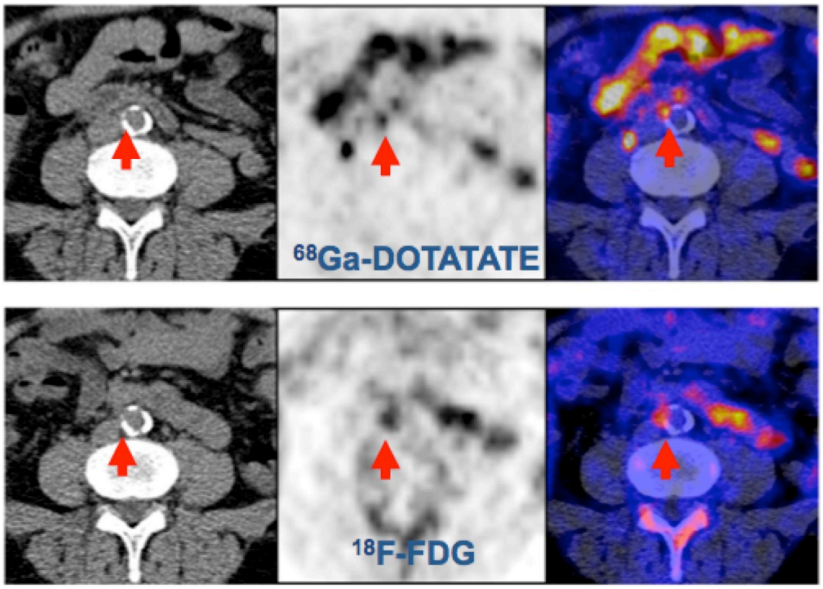

Figure 19: Colocalized focal vascular uptake of ^{18}F-FDG and ^{68}Ga-DOTATATE. Transverse views of a 61-year-old male patient with hypertension and a history of cardiovascular disease. Positive uptake is present on both ^{68}Ga-DOTATATE (upper row) and ^{18}F-FDG PET/CT (lower row) at the same location in the abdominal aorta of this patient (red circle). Also, serious calcification was detected at the same position. TBRDOTATATE was 6.18, while TRB ^{18}F-FDG was 2.42.

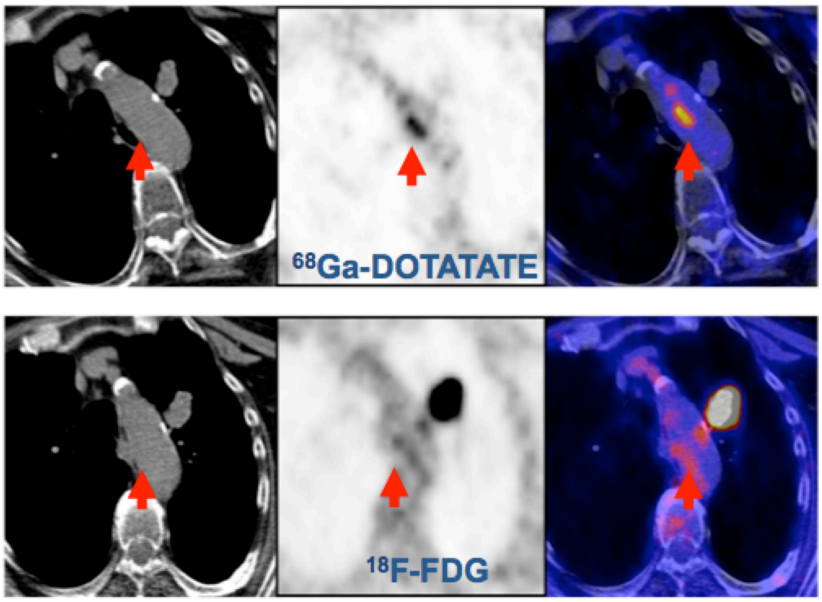

Figure 20: Focal vascular uptake of ^{68}Ga-DOTATATE without corresponding focal ^{18}F-FDG uptake. Transverse PET/CT images of a 73-year-old male patient with hypertension, hypercholesterolemia, and smoking. Intense focal uptake of ^{68}Ga-DOTATATE can be observed in the aortic arch (upper row), whereas no focally increased ^{18}F-FDG uptake was seen (lower row). TBRDOTATATE was 7.60, while TRB^{18}F-FDG was 1.74.

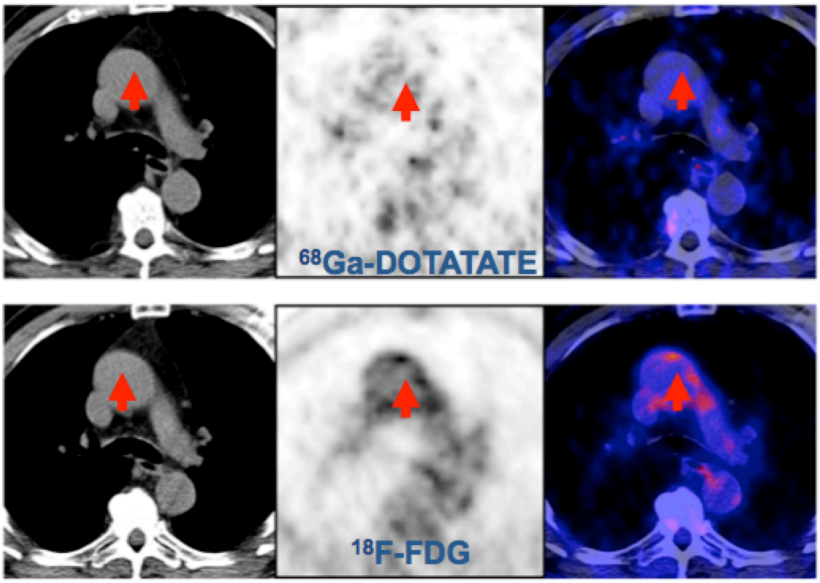

Figure 21: Focal uptake of ^{18}F-FDG but not DOTATATE in the vessel wall. Transverse PET/CT images of a 77-year-old male patient. With hypertension, hypercholesterolemia, history of coronary disease and a family history of cardiovascular disease. Intense ^{18}F-FDG uptake can be observed in the aortic arch (upper row), whereas no focally increased ^{68}Ga-DOTATATE uptake can be seen (lower row). TBRDOTATATE was 1.64, while TRB ^{18}F-FDG was 2.50.

On evaluation of the 37 sites with highest ^{68}Ga-DOTATATE TBR value, a colocalized focal increase of ^{18}F-FDG uptake was observed in 43.2% (16 sites, 10 sites with calcification, 6 sites without calcification) while 56.8% of the sites (21 sites, 6 sites with calcification, 15 sites without calcification) were negative. Of 39 sites with highest ^{18}F-FDG uptake, only 28.2% had an increased uptake of ^{68}Ga-DOTATATE (11 sites, 4 sites with calcification, 7 sites without calcification), while 71.8% of the sites (28 sites, 6 sites with calcification, 22 sites without calcification) were recorded as negative (Fig. 22).

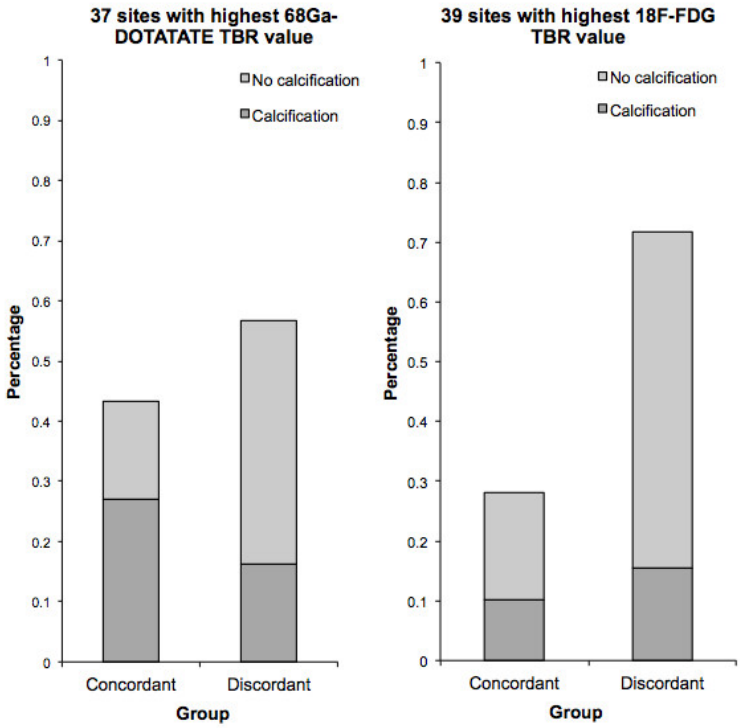

Figure 22: Colocalization of focal ^{68}Ga-DOTATATE and ^{18}F-FDG uptake. Comparison of 37 foci of increased ^{68}Ga-DOTATATE uptake (left) and 39 foci of increased ^{18}F-FDGuptake (right) with respect to colocalized focal uptake of the other radiotracer and calcification. Imaging findings were characterized as concordant when there was agreement in positive detection with both tracers, and as discordant in cases of discrepancy between the two tracers' uptake.

We compared the uptake of the two tracers in between high risk and low risk groups. We found the tendency both tracer's uptake from patients in high risk group is higher than low risk group. And the ^{68}Ga-DOTATATE show a statistical significance in more arteries than^{18}F-FDG (Fig.23). In the group internal comparison, ^{68}Ga-DOTATATE show higher TBR value in both groups, especially in high risk group, more significant high uptake were founded (Fig.24).

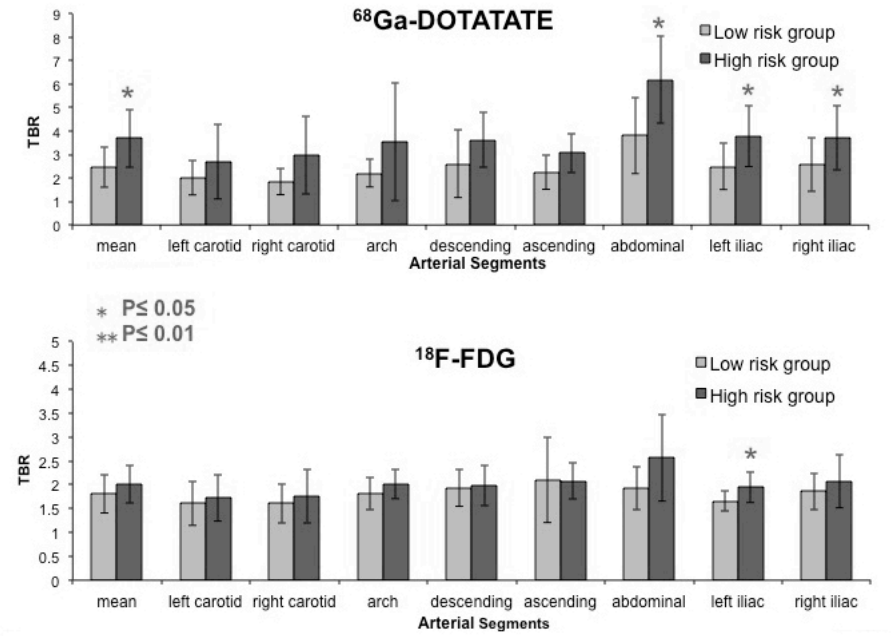

Figure 23: Comparison between high and low-risk group for cardiovascular disease, in regard to the ^{18}F-FDG and ^{68}Ga-DOTATATE uptake of big arterial vessels. * Comparison is significant at the 0.05 level (2-tailed).^{68}Ga-DOTATATE uptake in abdominal, both iliac arteries and mean TBR are significant higher in high risk group. Uptake of ^{18}F-FDG only in left iliac artery is higher in high risk group.

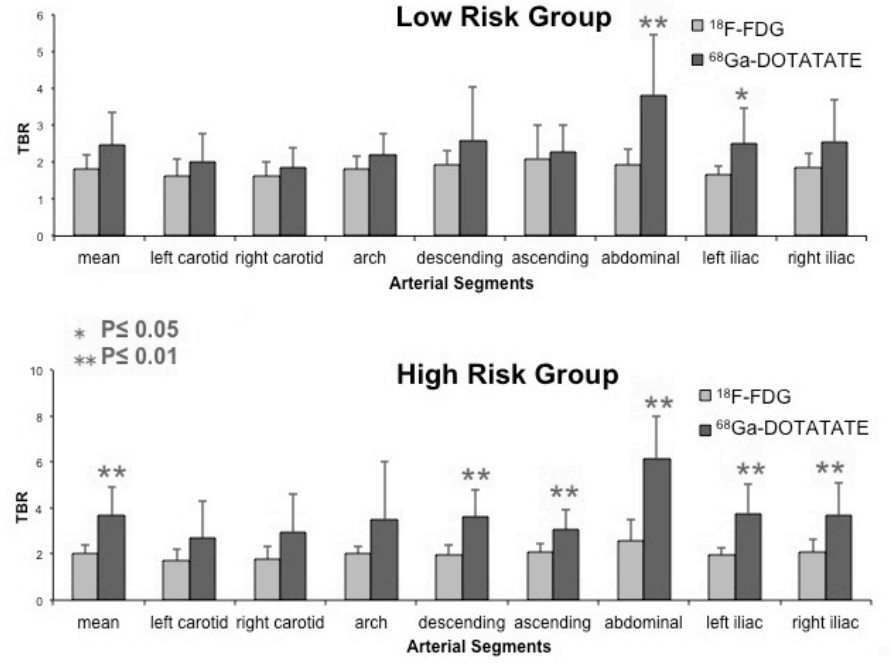

Figure 24: Comparison of ^{18}F-FDG and ^{68}Ga-DOTATATE uptake of big arterial vessels within high and low-risk group respectively. ** Comparison is significant at the 0.01 level (2-tailed); * Comparison is significant ($p < 0.05$) level . ^{68}Ga-DOTATATE show higher TBR value in both groups in comparison of ^{18}F-FDG. In low-risk group, significant higher uptakes of ^{68}Ga-DOTATATE were observed in abdominal and left iliac arteries while in high-risk group, more aorta segments such as descending, ascending, abdominal, left and right iliac arteries were found that TBR value of ^{68}Ga-DOTATATE PET is significantly higher than ^{18}F-FDG PET.

In total, 12 patients were examined to have focal increased uptakes of ^{68}Ga-DOTATATE, while 10 patients were found to have ^{18}F-FDG focal increased uptakes. As previously recommended, we also used the mean TBR, which was calculated as the mean value of TBRs from eight arterial segments for statistical analyses. Comparison of focal ^{68}Ga-DOTATATE and ^{18}F-FDG uptake in eight arterial segements were shown in Table 9.

Table 9. Comparison of focal ^{68}Ga-DOTATATE and ^{18}F-FDG uptake in eight arterial segements

Artery	Tracer	Mean±SD	95%CI for mean	P value*
Left carotid	^{18}F-FDG	1.67±0.46	1.42,1.91	< 0.05
	^{68}Ga-DOTATATE	2.37±1.26	1.70,3.04	
Right carotid	^{18}F-FDG	1.68±0.48	1.43,1.94	< 0.05
	^{68}Ga-DOTATATE	2.41±1.34	1.69,3.12	
Aortic arch	^{18}F-FDG	1.91±0.33	1.73,2.09	NS
	^{68}Ga-DOTATATE	2.86±1.89	1.86,3.87	
Descending aorta	^{18}F-FDG	1.96±0.39	1.76,2.17	< 0.01
	^{68}Ga-DOTATATE	3.12±1.38	2.38,3.85	
Ascending aorta	^{18}F-FDG	2.09±0.66	1.74,2.44	< 0.05
	^{68}Ga-DOTATATE	2.67±0.87	2.20,3.13	
Abdominal aorta	^{18}F-FDG	2.24±0.77	1.83,2.65	< 0.01
	^{68}Ga-DOTATATE	4.99±2.07	3.89,6.10	
Left iliac artery	^{18}F-FDG	1.62±0.31	1.62,1.95	< 0.01
	^{68}Ga-DOTATATE	3.13±1.26	2.44,3.82	
Right iliac artery	^{18}F-FDG	1.96±0.47	1.71,2.21	< 0.01
	^{68}Ga-DOTATATE	3.14±1.35	2.42,3.86	
Mean	^{18}F-FDG	1.91±0.40	1.70,2.13	< 0.01
	^{68}Ga-DOTATATE	3.08±1.21	2.44,3.73	

Sub-group analysis

Two risk-related groups were formed to assess the differential vascular uptake of two tracers. The summed calcification scores (CPsum) differed significantly between the two groups ($p<0.05$). TBR_{mean}, $TBR_{abdominal}$, TBR_{left_iliac} and TBR_{right_iliac} of ^{68}Ga-DOTATATE of were significant higher in the high-risk group (at least two cardiovascular risk factors) as compared to the low risk group (at most the one cardiovascular risk factor) (Fig. 23). In contrast, for ^{18}F-FDG TBR_{mean} and $TBR_{abdominal}$ only showed a tendency for a higher uptake in the high risk group; only the TBR value in the left iliac artery was found to be significantly higher ($p<0.05$).

Furthermore, in the interval comparison of two tracers within each group, there was no significant difference between the two tracers except for the abdominal aorta ($p<0.01$) and left iliac artery ($p<0.05$) in the low-risk group. However, in the high-risk group, ^{68}Ga-DOTATATE showed significantly higher values for TBR_{mean}, $TBR_{descending}$, $TBR_{ascending}$, $TBR_{abdominal}$, TBR_{left_iliac}, and TBR_{right_iliac} compared to the low risk group (Fig. 24) (Table 10) (Table 11)

Table 10. Comparison between high and low-risk group for cardiovascular disease, in regard to the ^{18}F-FDG and ^{68}Ga-DOTATATE uptake of big arterial vessels and calcified plaques

Parameters			**Risk Group** Low Risk (n=8) (95% CI for mean)	High Risk (n=8) (95% CI for mean)	Sig. (p value)
No. of risk factors			0.43	2.88	
Age			59±8.21 (48;71)	67±8.42 (52;77)	
Mean (Range)	^{18}F-FDG	TBR_{mean}	1.81±0.40 (1.48;2.14)	2.01±0.40 (1.68;2.35)	0.315
	^{68}Ga-DOTATATE	TBR_{mean}	2.47±0.86 (1.76;3.19)	3.70±1.24 (2.66;4.74)	0.038
	CP sum		4.75±5.23 (0.38;9.12)	14.12±7.86 (7.55;20.7)	0.014
TBR (Range)	^{18}F-FDG	$TBR_{left\ carotid}$	1.61±0.46 (1.22;1.99)	1.73±0.49 (1.31;2.14)	0.626
		$TBR_{right\ carotid}$	1.61±0.41 (1.27;1.96)	1.76±0.56 (1.29;2.22)	0.565
		TBR_{arch}	1.81±0.34 (1.52;2.10)	2.01±0.30 (1.76;2.27)	0.227
		$TBR_{descending}$	1.94±0.39 (1.62;2.27)	1.98±0.42 (1.64;2.33)	0.835
		$TBR_{ascending}$	2.10±0.89 (1.36;2.85)	2.08±0.38 (1.76;2.40)	0.948
		$TBR_{abdominal}$	1.92±0.45 (1.54;2.29)	2.57±0.91 (1.81;3.32)	0.092
		TBR_{left_iliac}	1.66±0.22 (1.43;1.81)	1.95±0.32 (1.68;2.21)	0.03
		TBR_{right_iliac}	1.86±0.39 (1.53;2.19)	2.07±0.55 (1.61;2.52)	0.403
	^{68}Ga-DOTATATE	$TBR_{left\ carotid}$	2.02±0.74 (1.41;2.64)	2.71±1.60 (1.37;4.05)	0.29
		$TBR_{right\ carotid}$	1.84±0.55 (1.38;2.30)	2.97±1.67 (1.57;4.38)	0.089
		TBR_{arch}	2.20±0.58 (1.71;2.68)	3.53±2.51 (1.44;5.63)	0.164
		$TBR_{descending}$	2.60±1.43 (1.40;3.80)	3.63±1.19 (2.63;4.63)	0.139
		$TBR_{ascending}$	2.26±0.74 (1.64;2.87)	3.07±0.84 (2.38;3.77)	0.057
		$TBR_{abdominal}$	3.82±1.63 (2.45;5.18)	6.17±1.85 (4.62;7.71)	0.017
		TBR_{left_iliac}	2.49±0.98 (1.67;3.31)	3.78±1.29 (2.70;4.86)	0.041
		TBR_{right_iliac}	2.56±1.13 (1.62;3.50)	3.71±1.37 (2.56;4.86)	0.048

Table 11. Comparison between ^{18}F-FDG and ^{68}Ga-DOTATATE uptake of big arterial vessels within high and low-risk group respectively

		^{18}F-FDG (95% CI for mean)	^{68}Ga-DOTATATE (95% CI for mean)	Sig. (p value)
Low Risk (n=8)	TBR_{mean}	1.81±0.40 (1.48;2.14)	2.47±0.86 (1.76;3.19)	0.067
	$TBR_{left\ carotid}$	1.61±0.46 (1.22;1.99)	2.02±0.74 (1.41;2.64)	0.195
	$TBR_{right\ carotid}$	1.61±0.41 (1.27;1.96)	1.84±0.55 (1.38;2.30)	0.369
	TBR_{arch}	1.81±0.34 (1.52;2.10)	2.20±0.58 (1.71;2.68)	0.126
	$TBR_{descending}$	1.94±0.39 (1.62;2.27)	2.60±1.43 (1.40;3.80)	0.231
	$TBR_{ascending}$	2.10±0.89 (1.36;2.85)	2.26±0.74 (1.64;2.87)	0.713
	$TBR_{abdominal}$	1.92±0.45 (1.54;2.29)	3.82±1.63 (2.45;5.18)	0.007
	TBR_{left_iliac}	1.66±0.22 (1.43;1.81)	2.49±0.98 (1.67;3.31)	0.049
	TBR_{right_iliac}	1.86±0.39 (1.53;2.19)	2.56±1.13 (1.62;3.50)	0.118
High Risk (n=8)	TBR_{mean}	2.01±0.40 (1.67;2.88)	3.70±1.24 (2.58;5.69)	0.003
	$TBR_{left\ carotid}$	1.73±0.49 (1.31;2.14)	2.71±1.60 (1.37;4.05)	0.119
	$TBR_{right\ carotid}$	1.76±0.56 (1.29;2.22)	2.97±1.67 (1.57;4.38)	0.071
	TBR_{arch}	2.01±0.30 (1.76;2.27)	3.53±2.51 (1.44;5.63)	0.111
	$TBR_{descending}$	1.98±0.42 (1.64;2.33)	3.63±1.19 (2.63;4.63)	0.002
	$TBR_{ascending}$	2.08±0.38 (1.76;2.40)	3.07±0.84 (2.38;3.77)	0.008
	$TBR_{abdominal}$	2.57±0.91 (1.81;3.32)	6.17±1.85 (4.62;7.71)	0.001
	TBR_{left_iliac}	1.95±0.32 (1.68;2.21)	3.78±1.29 (2.70;4.86)	0.002
	TBR_{right_iliac}	2.07±0.55 (1.61;2.52)	3.71±1.37 (2.56;4.86)	0.007

Correlation with risk factors

Table 12 shows a correlation of ^{18}F-FDG and ^{68}Ga-DOTATATE mean TBR values with clinical baseline characteristics. Hypertension significantly correlated with ^{18}F-FDG (R=0.58, P<0.05) and also with ^{68}Ga-DOTATATE uptake (R=0.60, p<0.01). The ^{68}Ga-DOTATATE TBR_{mean} also showed a significant correlation with plaque burden (R=0.52, P<0.05); hypertension (R=0.60, P<0.05) and age (R=0.56, P<0.05). In addition, plaque burden was also significant correlated with smoking (R=0.55, P<0.05) and a history of cardiovascular disease (R=0.63, P<0.01). There was a significant correlation between the two tracer's uptake (R=0.64, P<0.05).

Table 12. Correlation of ^{18}F-FDG TBR_{mean} and ^{68}Ga-DOTATATE TBR_{mean} of eight arterial segments to the baseline characteristics

	Pearson's correlation coefficients for the correlation between risk factors and imaging results											
	Mean ^{18}F-FDG	Mean ^{68}Ga-DOTATATE	PB	Hyper chol	HTN	Smoker	DM	Family history of CAD	CVD	Age	Gender	BMI
Mean ^{18}F-FDG	1	0.64[a]	NS	NS	0.58[b]	NS	NS	NS	NS	NS	NS	NS
Mean ^{68}Ga-DOTATE	0.64[a]	1	0.52[b]	NS	0.60[b]	NS	NS	NS	NS	0.56[b]	NS	NS
PB	NS	0.52[b]	1	NS	NS	0.55[b]	NS	NS	0.63[a]	NS	NS	NS

[a]Correlation is significant at the 0.01 level (two-tailed). [b]Correlation is significant at the 0.05 level (two-tailed). BMI, body mass index; CAD, coronary artery disease ; CVD, cardiovascular disease; DM, diabetes mellitus; HTN, hypertension; Hyperchol, hypercholesterolemia; NS, no significance; PB, plaque burden

5.3 Discussion

Our study was aimed to investigate the potential of ^{68}Ga-DOTATATE PET/CT to detect macrophage density at inflammatory lesions of large arteries. In addition, we compared the tracer uptake with that of ^{18}F-FDG regarding colocalization and intensity of the uptake in correlation to commonly accepted risk factors for cardiovascular disease. To our knowledge, this is the first investigation to compare ^{18}F-FDG and ^{68}Ga-DOTATATE in atherosclerosis imaging.

^{18}F-FDG has already been established as a useful tool to identify inflammatory processes e.g. in large arteries (57,79,105,126,149,150). In general, it is taken up by cells in proportion to their metabolic activity. Rudd and Tawakol 's group reported that carotid atherosclerotic plaques with high ^{18}F-FDG uptake have a high macrophage density (79,150), indicating that ^{18}F-FDG might be a useful tool to detect inflammatory plaques. ^{68}Ga-DOTATATE has also been demonstrated to detect activated macrophages (115) due to a specific overexpression of the somatostatin receptor 2 (SSTR2), the specific molecular target of ^{68}Ga-DOTATATE, on the cell surface of activated macrophages.

Although the potential for macrophage detection has been demonstrated for both ^{18}F-FDG and ^{68}Ga-DOTATATE, a concordant focally increased uptake was only found in the minority of cases in this study.

When comparing patients with and without risk factors for cardiovascular disease, many sites of tracer uptake could be detected both in high-risk and low-risk patients with ^{18}F-FDG. In most arterial segments (apart from the ascending aorta), maximum TBR values of the high-risk group were higher than those of the low-risk group. However, this difference did not reach statistical significance except for the left iliac artery.

There were few significant differences between the two tracers in the low-risk group. In the high-risk group however, TBR for ^{68}Ga-DOTATATE showed significantly higher values than for ^{18}F-FDG.

Additionally, significant correlations between the mean uptake of both tracers and the patients´ score of risk factors were found. In the literature, several studies reported significant correlations between focally increased ^{18}F-FDG uptake in the walls of large arteries and presence of cardiovascular risk factors, such as hypercholesterolemia, hypertension, age and diabetes (151). Other study groups found associations between the plaque burden of the left anterior descending coronary artery and cardiovascular risk factors (84,149). In our study, only a significant correlation between the mean TBR in the abdominal aorta with hypertension was

found. The lack of further correlations might be due to the small size of our sample. However, we found that age significantly correlates with ^{18}F-FDGuptake in three vessel segments. This is in line with previous studies, which demonstrated that the prevalence of visible ^{18}F-FDG positive arterial segments increases with age (80,152). For ^{68}Ga-DOTATATE, tracer uptake correlated significantly with hypertension, age and the presence of calcifications.

^{18}F-FDG uptake in inflammatory cells is influenced by macrophage differentiation and cell activation (91) since immune cell activation is associated with increased oxidative metabolism and consequently, increased use of glucose (105). In our investigation, we found many ^{18}F-FDG positive sites both in the low- as well as the high-risk group, whereas very few ^{68}Ga-DOTATATE positive foci could be found in low-risk individuals. This raises doubt whether all accumulations of ^{18}F-FDG within the arteries are due to macrophage-mediated inflammatory activity.

In contrast to ^{18}F-FDG, ^{68}Ga-DOTATATE visualizes the distribution of SSTR-2. As mentioned above, specific expression of SSTR-2 on the surface of macrophages as well as significant upregulation of this receptor upon stimulation (e.g. with lipopolysaccharide [LPS]) have been reported (113). Furthermore, another research group observed that the expression of SSTR-2 in human coronary endothelial cells is decreased by treatment with the inflammatory cytokine TNF-α, which is mainly produced and secreted by activated macrophages (132). Therefore, in the pro-inflammatory setting, SSTR-2 expression is upregulated for macrophages whereas, on the other hand, it is downregulated in endothelial cells. In coronary heart disease, this idea could support the use of ^{68}Ga-DOTATATE for the detection of vulnerable plaques.

SSTR-2 also plays another role in atherosclerotic plaques. Adams et al. demonstrated increased expression of SSTR-2 when human umbilical vein endothelial cells (HUVECs) are proliferating, thereby suggesting its active role in angiogenesis, which has been described in the context of unstable plaques. Consequently, ^{68}Ga-DOTATATE-PET could be used to visualize unstable plaques in two different ways; detection of activated macrophages as well as angiogenesis within the atherosclerotic lesion (153,154). Our results indicate that ^{68}Ga-DOTATATE-PET detects a higher number of increased focal uptakes in patients with high cardiovascular risk; this may be used as a complementary imaging modality in the detection of inflammatory plaque by identifying somatostatin receptor-positive sites within the arteries.

In this study risk factors for CAD correlated less strongly with foci of increased ^{18}F-FDG uptake as compared to ^{68}Ga-DOTATATE. This might be interpreted as an indication for better specificity of ^{68}Ga-DOTATATE for the inflamed plaque. However, due to the small sample size of our investigation, it is difficult to draw firm conclusions. For example, another reason for the

observed difference between the two tracers could be tracer kinetics. DOTATATE binds to the SSTR-2 and, thus, the uptake is potentially is limited by the number of saturated SSTR2 receptors. This is not the case with ^{18}F-FDG, which is continuously metabolized by activated macrophages. Otherwise, ^{18}F-FDG as the smaller molecule is potentially more vulnerable to unspecific uptake mechanisms like increased vascular permeability due to inflammation. So, in theory, ^{18}F-FDG should be more sensitive than DOTATATE, but potentially less specific, which could explain the better correlation with different risk groups. Another important limitation is the lack of histological validation of ^{68}Ga-DOTATATE uptake.

Due to the retrospective design a selection bias cannot be excluded. Also, this study was performed in cancer patients; therefore our findings may be not generalizable to studies in vascular disease. Especially, we cannot exclude the influence of anticancer therapies or hormone action of neuroendocrine tumors. So far, no influence of TSH-suppressive therapy or peptide receptor radionuclide therapy (PRRT) on atherosclerosis has been published. In the only patient with PRRT the interval to the PET scans was at least 8 weeks, so we do not expect any interference. Also, none of the two patients on chemotherapy was immunodeficient according to white blood cell count. However, further prospective studies in a higher number of non-oncological patients are warranted. In this series of cancer patients, we found a stronger association of increased ^{68}Ga-DOTATATE uptakewith known risk factors of cardiovascular disease as compared to ^{18}F-FDG, suggesting a potential role for plaqueimaging in large arteries. Strikingly, we found that focal uptake of ^{68}Ga-DOTATATE and ^{18}F-FDG does not colocalizein a significant number of lesions

5.4 Conclusion

In this series of cancer patients, we found a stronger association of increased ^{68}Ga-DOTATATE uptake with known risk factors of cardiovascular disease as compared to ^{18}F-FDG, suggesting a potential role for plaque imaging in large arteries. Strikingly, we found that focal uptake of ^{68}Ga-DOTATATE and ^{18}F-FDG does not colocalize in a significant number of lesions

6. ADDITIONAL STUDY

Endothelial CD81 is a biomarker of early atherosclerotic plaques for molecular imaging_Targeted superparamagnetic iron oxide (SPIO) study

In our study, we investigate the feasibility for molecular imaging of endothelial CD81 expression in vitro using the CD81-targeted superparamagnetic iron oxides (SPIO). Cluster designation 81 (CD81), a member of the tetraspanin superfamily of cell-surface proteins, tends to associate with integrins, with other tetraspanins and with lineage-specific molecules in the immune system and participates in diverse biologic activities including cell proliferation (155), differentiation(156), adhesion (157) and motility (158,159). Recently, through genetic screens, the tetraspanin CD81 was demonstrated to be a marker of early human atherosclerotic plaques (160). In their study, CD81 was significantly and specifically upregulated in endothelial cells of atherosclerotic plaques and played a crucial role in the initial stages of atherosclerotic plaque formation. These data indicate that the expression of CD81 proteins in endothelial cells is crucial for genesis and progress of atherosclerosis. In this context, the ability to visualize noninvasively the expression of the marker molecule would be very useful both in preclinical research and in the clinical setting. Here, we report on the use of antibody-coated SPIO to target the CD81 in murine endothelial cells that were treated with the phenazine methosulfate (PMS) in vitro.

6.1 Materials and Methods

Cell culture and in vitro induction of CD81 proteins

The murine bEnd.3 endothelial cells (1×10^5 cells/well) were cultured in plates as monolayer in Dulbecco's modified eagles medium (DMEM), supplemented with 10% fetal calf serum and 1% penicillin-streptomycin solution (1% v/v penicillin-streptomycin solution containing 5000 units penicillin and 5 mg streptomycin per mL) and maintained in a humidified atmosphere containing 5% CO_2 at 37°C. To induce expression of CD81 proteins, cells were seeded in 6-well plates overnight to allow cell adhesion. 0, 5, 10 or 20 µL 1 mM of PMS was added into the 1 mL of media (the final concentration is 0, 5, 10 or 20 µM, respectively) and further incubated for 16 h. Cells were collected for Western blot analysis.

Western blot analysis for the expression of CD81 proteins

Stress induced and non-stress induced bEnd.3 cells were lysed in 100 μL ice-cold lysis buffer (Radio-immunoprecipitation assay (RIPA). The lysates were centrifuged at 12,000 g at 4°C for 5 min and the supernatant was collected. 20 μL of supernatant containing the cell total proteins was separated by 12% sodium dodecyl sulfate polyacrylamide gel electrophoresis (SDS-PAGE) and transferred to polyvinylidene difluouride (PVDF) membranes (Amersham Biosciences, Freiburg, Germany). The PVDF membrane was further incubated with 2 mL PBS solution containing 4 μL Armenian hamster-anti-mouse CD81 primary antibody (0.5 mg/mL, 1:500 dilution; BD Biosciences) and was then incubated with 5 mL PBS solution containing 5 μL goat anti-Armenian hamster IgG HRP-labeled secondary antibody (0.2 mg/mL, 1:1000 dilution; BD Biosciences). The immunoblot was detected using the enhanced chemiluminescence system SuperSignal West Pico Chemiluminescent Substrate (Pierce, IL, USA). Quantization of CD81 proteins was carried out using Quanti-One software (BioRad, Hercules, CA, USA).

Labeling of targeted SPIO particles

Targeting moiety was conjugated to the SPIO surface via streptavidin-biotin bridging chemistry. Three types of target SPIO were produced.3×1ml Streptavidin-coated SPIO with 20 nm (5mg nanomag®-D-spio, Micromod GmbH, Rostock, Germany) was used to combine with biotinylated antibody/peptide respectively. CD81-targeted SPIOs ($SPIO_{cd81}$) were fabricated by incubated with biotinylated monoclonal rat anti-mouse-CD81 antibody (100 μg, Clone YN1/1.7.4, eBioscience). The mixtures were stirred overnight for at room temperature and then dialyzed for 48h to remove unbinding antibody (cut-off membrane 300KD). Plain SPIOs ($SPIO_{plain}$) also were used as control.

Animal

As for the stimulated group, to induce expression of CD81 proteins on vascular endothelium, a group of C57 mice (n = 5) were injected by tail vein injection of a dose of 0.25 mg PMS mixed in 100 μL saline per 1 kg body weight before killed. As for control group, C57 mice (n = 5) were not stimulated by tail vein injection of 100 μL saline. The aorta from all animals were obtained for 73russian blue staining and histology.

Cell culture and stimulation of PMS

The murine endothelial cell line b.END.3 was purchased from American type Culture Collection. The adherently growing cells were cultivated under standard condition at 37°C in a humidified 95% air/ 5% CO_2 incubator, maintained in the complete growth medium. It mainly including Dulbecco's Modified Eagle's Medium (DMEM) (Gibco), supplemented with 10% fetal calf serum (Gibco), 100 U/ml penicillin and 100 µg ml−1 streptomycin (Gibco). The bEnd.3 cells were used at passages 25 to 30. To induce expression of endothelial CD81, endothelial cells were seeds into 8-wells cell-culture plates, further 20µM PMS in the media was incubated with cells for 16h (71).

In vitro cellular affinity assay

After inducing of CD81 protein, the binding performance of targeted SPIO was determined. In brief, bEnd.3 cells were incubated with $SPIO_{CD81}$ and $SPIO_{plain}$ at particle concentration of 10^7/ml in culture medium for different time interval (10 min, 30 min, 1h and 3h) respectively. The whole incubation experiments were conducted with gentle sway. After incubation, the free contrast agents within culture medium was removed; and the cells were ready for Prussian blue staining after washing thrice with PBS (0.1mol/L. PH 7.4). To evaluate the specificity of $SPIO_{CD81}$, CD81-antibody was pre-incubated with induced cells for 2hs before incubation of $SPIO_{CD81}$.

In vitro vascular affinity assay

To determine the interaction between $SPIO_{CD81}$ and the ligand CD81 protein in atherosclerotic lesion, *ex vivo* binding experiments were conducted on the section of murine aortic plaque tissue. All of the tissues were obtained from four ApoE-/- mice (30weeks old), and three PMS-induced C57/6 mice as acute vascular inflammation model. Were The endothelial CD81 protein expression was assessed by Immunohistochemistry method. To evaluate the static binding efficiency of $SPIO_{CD81}$ to the initial and advanced atherosclerotic lesion, $SPIO_{CD81}$ (0.1mg/ml) were add to incubate with tissue on the section for 2h respectively at 37 °C. After incubation, non-binding USPIO was wash out by PBS.

Prussian blue staining

For Prussian blue staining, bEND.3 endothelial cells and tissue section from ApoE-/- mice were washed thrice with PBS and subsequently fixed with methanol and acetone (-20°C). For Prussian blue staining, the fixed cells were incubated with 10% potassium ferrocyanide for 5 min and 10% potassium ferrocyanide in 20% hydrochloric acid for 30 min, and counterstained with nuclear fast red.

Immunohistochemistry

Immediately following final imaging, the carotid artery samples were dissected for histologic phenotyping, covered with Tissue-Tek (Sakura, Torrance, CA, USA), and then frozen in liquid nitrogen vapor. The carotid artery sections (6 μm thick) were cut with a cryostat microtome (CM1950; Leica, Heidelberg, Germany). Double immunostaining was done using 1 μL Armenian hamster anti-mouse CD81 antibody (0.5 mg/mL, 1:50 dilution in PBS; BD Biosciences) and 1 μL secondary antibody, FITC-labeled rabbit anti-Armenian hamster IgG (0.1 mg/mL 1:100 dilution in PBS; BD Biosciences). Cell nuclei were counterstained by 4',6-diamidino-2-phenylindole (1:100 dilution in PBS; Invitrogen). Tissue fluorescence sections were viewed under a confocal microscope. The mean fluorescent intensity of veins was quantitatively evaluated by Image J software (National Institutes of Health, Bethesda, MD, USA).

.

6.2 Results

CD81 expression detection

Rohlena et al. (2009) (160)reported that CD81 proteins can be induced by phenazine methosulfate (PMS) and resulted in up-regulation of CD81 expression on the mRNA, as well as the protein level. We next examined the dose effect on expression of CD81 proteins in response to the oxidative stress inducer PMS. Results showed CD81 was only faintly detected in Western blots in non-stress induced bEnd.3 cells. In contrast, incubation of bEnd.3 with 5, 10 and 20 μM of PMS for 16 h caused a dose-dependent increase in CD81 expression (Fig. 25a). Quantization of CD81 proteins is shown in Fig. 25b. There were, respectively, 1.56, 1.94 and 2.71-fold increases in CD81 expression following the corresponding 5, 10 and 20 μM of PMS treatments, compared with those of untreated controls ($p < 0.01$).

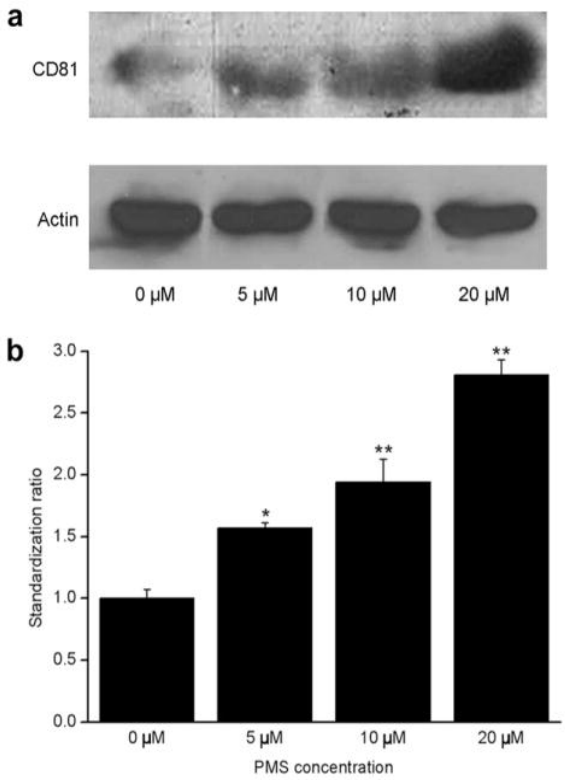

Figure 25: Immunoblotting for CD81 expression in bEnd.3 cells. (a) Immunoblotting assay for CD81 proteins extracted from bEnd.3 cells, which were incubated with 0, 5, 10 and 20 μM of phenazine methosulfate (PMS) for 16 h and from untreated control. The top row stands for CD81 proteins, indicating a gradual increasing trend with the increase of PMS concentrations. The bottom row stands for beta-actins that served here as a loading control and were kept constantly. (b) Quantitative assay of CD81 proteins through Quanti-One software. ** $p < 0.01$ ($n = 3$).

Examination of CD81-targeted SPIO binding affinity to bEnd.3 cells

To examine binding affinity and specificity, CD81-targeted SPIO and non-targeted SPIO were incubated with PMS-stress induced bEnd.3 cells. Results showed there was rarely binding of non-targeted SPIO to stress induced bEnd.3 cells. In contrast, a large number of CD81-targeted SPIO were found to be bound to the surface of stress induced bEnd.3 (Fig. 26)

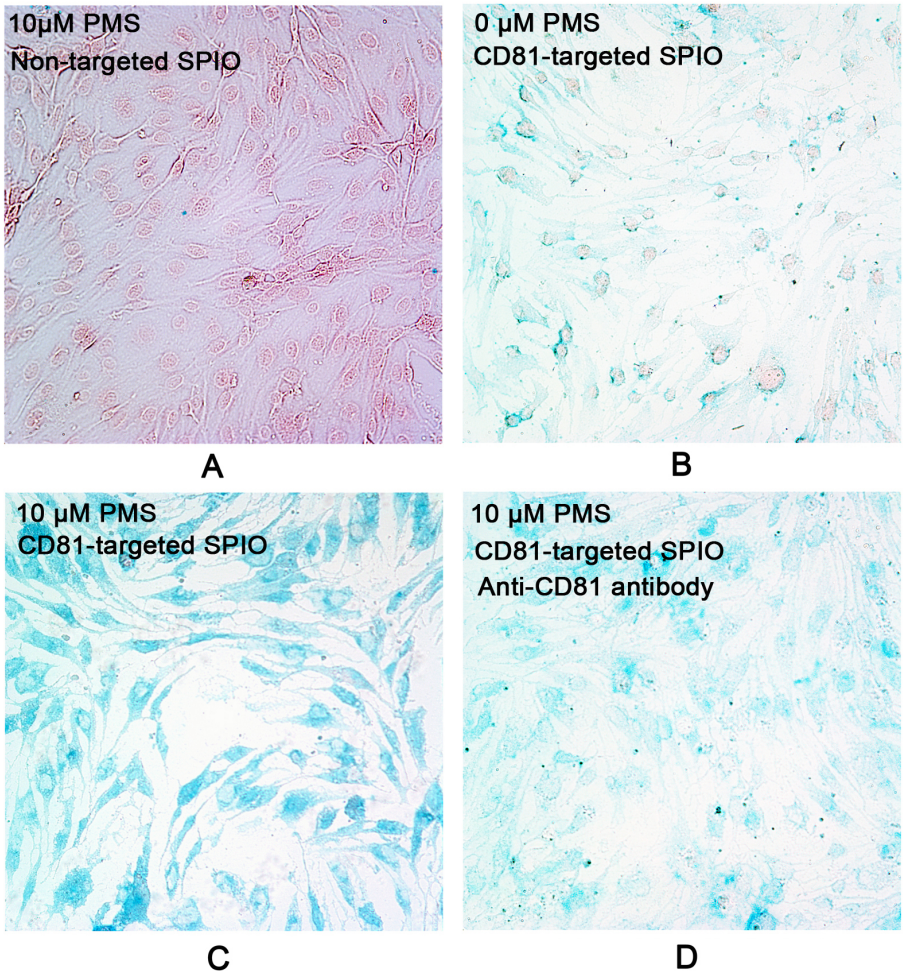

Figure 26: CD81-targeted superparamagnetic iron oxide (SPIO) binding to cultured bEnd.3 cells. Representative micrograph for CD81-targeted SPIO or non-targeted SPIO adhered to cells stimulated with 10 ithphenazine methosulfate (PMS). Non binding bettwen Non-targeted SPIO and PMS (10 μM) - induced cells were observed (A). Just a few CD81-targeted SPIO was able to bind to the cells without PMS stimulation (B). Greatly Increased uptake of CD81-targeted SPIO were observed at PMS (10 ed SPIO werethout PMS stimulation (B). G1 μg/mL free anti-CD81 antibodies with 10 t PMS stimulation (B). Greatly Increased uptake of CD81-targeted SPId uptake of CD81-targe

In vitro assessment of CD81 targeted SPIO to murine aorta

In vitro binding affinity of $SPIO_{plain}$ and $SPIO_{CD81}$ to atherosclerotic aorta, were assessed histologically by Prussian blue staining (Fig.27, Fig.28). High-number targeted SPIO accumulated at inflammatory aorta wall and atherosclerotic plaque segments, in comparison of no binding of non-targeted SPIO were founded at adjacent sections. Corresponding immunohistochemistry examinations were performed to confirm increased CD81 expression at PMS-induced aorta and advanced atherosclerotic plaque segment (Fig.27C and Fig.28C).

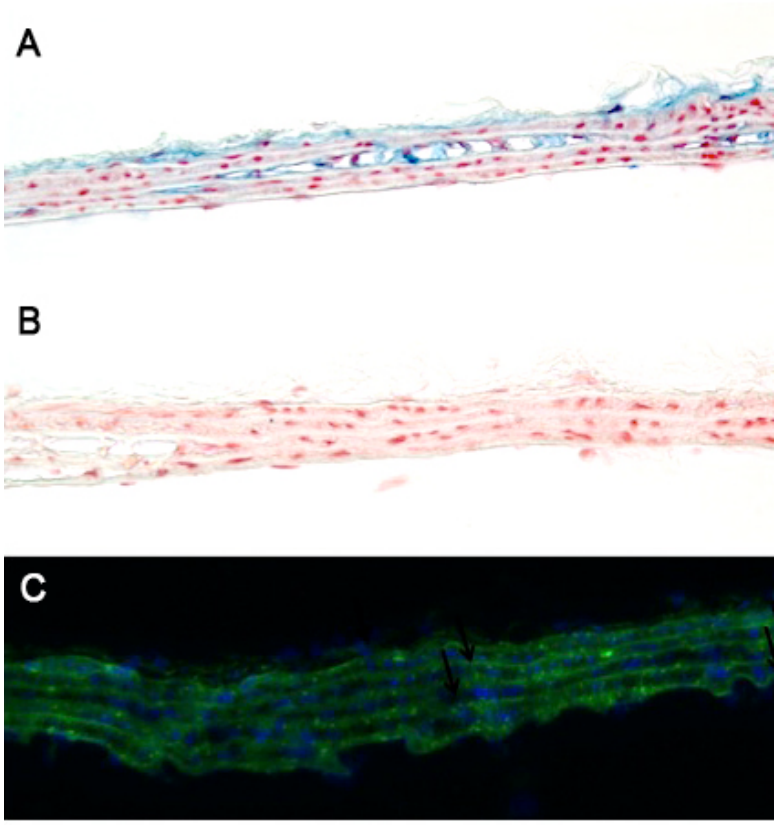

Figure 27: Assessment of targeted-CD81 SPIO and non-targeted SPIO in vitro binding to PMS stress induced murine endothelium. A. Strong uptake of targeted-CD81 SPIO at PMS-induced aorta segement were observed; B. Non detectable uptake of non-targeted SPIO at induced aorta segement were observed. C, Immunofluorescence assay for CD81 expression on the aorta section.

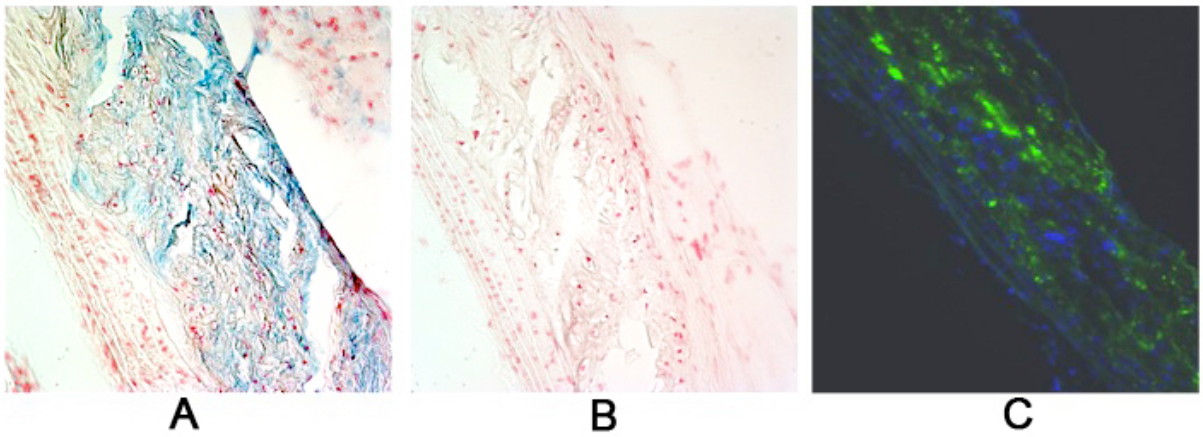

Figure 28. Assessment of targeted-CD81 SPIO and non-targeted SPIO in vitro binding to AopE-/- mice with advanced plaque. A. Strong uptake of targeted-CD81 SPIO at atherosclerotic segment was observed; B. Non detectable uptake of non-targeted SPIO at atherosclerotic segment was observed. C, Immunofluorescence assay for CD81 expression on the adjacent section

6.3 Discussion

Given the fact that atherosclerosis is a complex, chronic disorder involving inflammatory and proliferative signaling pathways, it is especially important to identify and quantify the specific molecular markers of atherosclerosis to provide diagnostic and prognostic information and to establish a basis for early atherosclerosis treatment response evaluation.(34,161).

Numerous molecules unregulated in activated endothelium of vascular disease providing potential markers for functional molecular imaging and targeted therapeutics. In previous investigation, vascular inflammatory biomarkers have been recognized to reflect essential features in the progression of atherosclerosis at early stage. But oxidative stress, another important event in formation of atherosclerosis, has less been considered as imaging target to evaluate. According to the Rohlena's finding, the expression pattern of endothelial cell CD81 is an ideal molecular marker for evaluating the atherosclerosis prior to the full-blown inflammatory response, which triggered us to investigate the feasibility for visualizing noninvasively the expression of the marker molecule using targeted MRI contrast agents.

Phenazine methosulphate (PMS) is a strong oxidant that induces reactive oxygen species (ROS) formation in cells. In the vasculature, increased ROS production has been associated with endothelial dysfunction, an early pathogenic event in atherosclerosis (162). In our study, it has been shown that a dose-dependent manner of CD81 expression after PMS treatment, which agrees with Rohlena's results.

Western blotting and immunocytochemistry staining are the most popular approaches to detect expression of proteins in the preclinical animals or clinic patients. Both need to collect ex vivo samples from animals or patients. Usually, invasive surgeries have to be performed and a set of experiment procedures has to be followed. In some cases, it is difficult to collect samples, particularly for patients with cardiovascular disease.

High-resolution MRI has emerged as potential promising noninvasive imaging modalities for the characterization of atherosclerotic plaques in vivo as it can provide anatomical, structural and functional data on the arterial wall. And one crucial challenge for molecular imaging is to design a potent contrast agent in sufficient quantity under conditions of shear stress.

In comparison, although MRI with SPIO still has room to improve, it has some advantages in preclinical applications, such as that it is readily available, easy to use and has the fast response-time to provide real-time imaging. More importantly, MRI uses contrast agents that remain exclusively intravascular, minimizing nonspecific signals from extravasated contrast material. Our results indicated that the intensity CD81-targeted SPIO correlates well with

relative expression of CD81 by immunoblotting or immunocytochemistry. Although these data may not be directly comparable, these findings are especially valuable since imaging can provide an alternative strategy for evaluating early response to oxidant stress stimulation in terms of spatial extent and amount of endothelial CD81 proteins in a noninvasive or minimal-invasive manner. In fact, numerous investigators have adopted approaches in which molecular imaging has been attained through the use of targeted molecular imaging modalities and many proteins related to atherosclerosis such as ICAM-1 (163) VCAM-1 (164) P-selectin (74) von Willebrand factor (165) (vWF) and integrins (166), have been imaged.

In this work, avidin-biotin adhesion was employed between anti-CD81 antibodies and contrast agents, given the fact that the strongest known non-covalent interaction between a protein and a ligand with an affinity of 10^{15} M^{-1} at pH 5. It was found by (167) that by using (strept) avidin bridge, both microbubble and SPIO can be easily decorated with a wide variety of ligands or combinations of ligands.

Although targeting with targeted contrast agents for molecular imaging of large arteries is still a challenge due to the high shear stress, our results has shown anti-CD81-coated contrast agents enables molecular imaging of CD81 expression on vascular endothelium. Our success maybe contributes to the relatively small size of SPIO (about 20 nm with centered diameter distribution) and high-level expression of CD81 proteins with four transmembrane (TM) helices. Indeed, it was demonstrated that a small size favors attachment of targeted contrast agents at high shear stresses. With decreasing diameter, the shear stress required to set a particle in motion becomes higher (168). Moreover, CD81 is an expressed cell-surface protein, which plays in an important role in adhesion (157). The crystal structure of human CD81 large cysteine-rich extracellular domain demonstrated each subunit within the homodimeric protein displays a mushroom-like structure, composed of five-helices arranged in “stalk” and “head” subdomains. These structural characteristics make it more easily form firm adhesion with anti-CD81 antibodies (169-171).

Consequently, CD81 also play an important role in cellular adhesive interactions in the immune system. And the co-localization of CD81 and inflammation-associated biomarkers further confirmed its role in the initial stages of atherosclerotic lesion formation. Here we develop a novel CD81 ligand-targeting strategy combined with MR techniques to evaluate the oxidative stress within the artery.

Limitation

There are several limitations of this study. For MRI molecular imaging, high dose SPIO is required to obtain efficient binding in the in vivo study. In addition, it cannot be assumed that

the models we used to test the feasibility of CD81-targeted SPIO are identical to disease-related CD81 expression. In the clinical setting, more complex factors such as disease-related inducers, individual differences and intricate signal pathway are often involved into the regulation of CD81 expression. Although there is still a long way to translate this technique from the animal model to the clinical situation, it is eventually desirable to couple the level of video-intensity signal from the targeted molecular imaging to the stage of the disease and to the risk assessment of atherosclerosis. Due to there is high patient to patient variation, it will be necessary to image besides the effected carotid artery or a control artery, in which the expression of CD81 must be less. Furthermore, the accuracy of CD81 quantification using the targeted contrast agents may be limited by some degree of nonspecific binding due to the wide and overlapping expression of CD81 by the vascular endothelium. Therefore, future studies including examination of the feasibility for assessing atherosclerosis and optimization of relative parameters using the CD81-targeted SPIO are required.

6.4 Conclusion

This study has shown that CD81-targeted SPIO may enable expression on vascular endothelium in vitro CD81.This oxidative stress associated MRI contrast agent may provide reference values of relative expression of CD81.

7. CONCLUSION

In conclusion, the ^{68}Ga-DOTATATE studies demonstrated the capability of SSTR-2 targeted radiotracer ^{68}Ga-DOTATATE to detect macrophage in atherosclerotic plaque. Accumulation of ^{68}Ga-DOTATATE co-localized with the atherosclerotic macrophage-rich plaques suggests that ^{68}Ga-DOTATATE may a suitable tracer for the evaluation of inflammatory activity in unstable macrophage rich plaques. And data of pilot patient study demonstrated a stronger association between an increased ^{68}Ga-DOTATATE uptake with known risk factors of cardiovascular disease as compared to ^{18}F-FDGin a limited number of oncological patients, suggesting a potential role of this tracer for plaque imaging in the large arteries and coronaries. Strikingly, we found that the focal uptake of ^{68}Ga-DOTATATE and ^{18}F-FDG does not co-localize in a significant percentage of lesions. This warrants further investigation on the distribution of the two tracers within atherosclerotic plaques

The P-selectin affinity PET tracer, Gallium-68 labeled Fucoidan, according to this preclinical validation study, may hold the potential to discriminate between active and inactive atherosclerotic plaques. However, further studies are necessary to elucidate the role of ^{68}Ga-Fucoidan for atherosclerotic plaque imaging.

We developed CD81-targeted SPIO to evaluate the oxidative stress in the plaque in terms of alternative expression of CD81 proteins stress. Our initial experience using the CD81-targeted SPIO has shown that it may enable expression on vascular endothelium in vitro CD81.This oxidative stress associated MRI contrast agent may provide reference values of relative expression of CD81 and information likely to be very useful to address the detection, prognosis, vulnerable potential of atherosclerosis or susceptibility to anti-atherosclerosis drugs.

8. REFERENCE

1. Myerburg RJ, Interian A, Jr., Mitrani RM, Kessler KM, Castellanos A. Frequency of sudden cardiac death and profiles of risk. The American journal of cardiology 1997;80:10F-19F.
2. Murray CJ, Lopez AD. Global mortality, disability, and the contribution of risk factors: Global Burden of Disease Study. Lancet 1997;349:1436-42.
3. Casscells W, Naghavi M, Willerson JT. Vulnerable atherosclerotic plaque: a multifocal disease. Circulation 2003;107:2072-5.
4. Naghavi M, Libby P, Falk E et al. From vulnerable plaque to vulnerable patient: a call for new definitions and risk assessment strategies: Part II. Circulation 2003;108:1772-8.
5. Naghavi M, Libby P, Falk E et al. From vulnerable plaque to vulnerable patient: a call for new definitions and risk assessment strategies: Part I. Circulation 2003;108:1664-72.
6. Falk E. Plaque rupture with severe pre-existing stenosis precipitating coronary thrombosis. Characteristics of coronary atherosclerotic plaques underlying fatal occlusive thrombi. British heart journal 1983;50:127-34.
7. Friedman M, Van den Bovenkamp GJ. Role of thrombus in plaque formation in the human diseased coronary artery. British journal of experimental pathology 1966;47:550-7.
8. Constantinides P. Pathogenesis of cerebral artery thrombosis in man. Archives of pathology 1967;83:422-8.
9. Davies MJ, Thomas AC. Plaque fissuring--the cause of acute myocardial infarction, sudden ischaemic death, and crescendo angina. British heart journal 1985;53:363-73.
10. Ross R, Glomset JA. Atherosclerosis and the arterial smooth muscle cell: Proliferation of smooth muscle is a key event in the genesis of the lesions of atherosclerosis. Science 1973;180:1332-9.
11. Ross R. Atherosclerosis--an inflammatory disease. The New England journal of medicine 1999;340:115-26.
12. Danesh J, Wheeler JG, Hirschfield GM et al. C-reactive protein and other circulating markers of inflammation in the prediction of coronary heart disease. The New England journal of medicine 2004;350:1387-97.
13. Libby P. Inflammation in atherosclerosis. Nature 2002;420:868-74.
14. Weber C, Zernecke A, Libby P. The multifaceted contributions of leukocyte subsets to atherosclerosis: lessons from mouse models. Nature reviews Immunology 2008;8:802-15.

15. Leonard EJ, Yoshimura T. Human monocyte chemoattractant protein-1 (MCP-1). Immunology today 1990;11:97-101.
16. Quehenberger O. Thematic review series: the immune system and atherogenesis. Molecular mechanisms regulating monocyte recruitment in atherosclerosis. Journal of lipid research 2005;46:1582-90.
17. Stemme S, Hansson GK. Immune mechanisms in atherosclerosis. Coronary artery disease 1994;5:216-22.
18. Hansson GK. Regulation of immune mechanisms in atherosclerosis. Annals of the New York Academy of Sciences 2001;947:157-65; discussion 165-6.
19. Hansson GK. Immune mechanisms in atherosclerosis. Arteriosclerosis, thrombosis, and vascular biology 2001;21:1876-90.
20. Napoli C, D'Armiento FP, Mancini FP et al. Fatty streak formation occurs in human fetal aortas and is greatly enhanced by maternal hypercholesterolemia. Intimal accumulation of low density lipoprotein and its oxidation precede monocyte recruitment into early atherosclerotic lesions. The Journal of clinical investigation 1997;100:2680-90.
21. Stary HC, Chandler AB, Glagov S et al. A definition of initial, fatty streak, and intermediate lesions of atherosclerosis. A report from the Committee on Vascular Lesions of the Council on Arteriosclerosis, American Heart Association. Circulation 1994;89:2462-78.
22. Foteinos G, Xu Q. Immune-mediated mechanisms of endothelial damage in atherosclerosis. Autoimmunity 2009;42:627-33.
23. Galkina E, Ley K. Immune and inflammatory mechanisms of atherosclerosis (*). Annual review of immunology 2009;27:165-97.
24. Chow WS, Xu A, Woo YC et al. Serum fibroblast growth factor-21 levels are associated with carotid atherosclerosis independent of established cardiovascular risk factors. Arteriosclerosis, thrombosis, and vascular biology 2013;33:2454-9.
25. Kimura K, Hashiguchi T, Deguchi T et al. Serum VEGF--as a prognostic factor of atherosclerosis. Atherosclerosis 2007;194:182-8.
26. Winnik S, Lohmann C, Siciliani G et al. Systemic VEGF inhibition accelerates experimental atherosclerosis and disrupts endothelial homeostasis--implications for cardiovascular safety. International journal of cardiology 2013;168:2453-61.
27. Inoue M, Itoh H, Ueda M et al. Vascular endothelial growth factor (VEGF) expression in human coronary atherosclerotic lesions: possible pathophysiological significance of VEGF in progression of atherosclerosis. Circulation 1998;98:2108-16.
28. Howell WM, Ali S, Rose-Zerilli MJ, Ye S. VEGF polymorphisms and severity of atherosclerosis. Journal of medical genetics 2005;42:485-90.

29. Ramos MA, Kuzuya M, Esaki T et al. Induction of macrophage VEGF in response to oxidized LDL and VEGF accumulation in human atherosclerotic lesions. Arteriosclerosis, thrombosis, and vascular biology 1998;18:1188-96.
30. Celletti FL, Waugh JM, Amabile PG, Brendolan A, Hilfiker PR, Dake MD. Vascular endothelial growth factor enhances atherosclerotic plaque progression. Nature medicine 2001;7:425-9.
31. Stary HC, Chandler AB, Dinsmore RE et al. A definition of advanced types of atherosclerotic lesions and a histological classification of atherosclerosis. A report from the Committee on Vascular Lesions of the Council on Arteriosclerosis, American Heart Association. Circulation 1995;92:1355-74.
32. Pearson TA, Wang BA, Solez K, Heptinstall RH. Clonal characteristics of fibrous plaques and fatty streaks from human aortas. The American journal of pathology 1975;81:379-87.
33. Masuda J, Ross R. Atherogenesis during low level hypercholesterolemia in the nonhuman primate. II. Fatty streak conversion to fibrous plaque. Arteriosclerosis 1990;10:178-87.
34. Lusis AJ. Atherosclerosis. Nature 2000;407:233-41.
35. Antoniades C, Tousoulis D, Tentolouris C, Toutouzas P, Stefanadis C. Oxidative stress, antioxidant vitamins, and atherosclerosis. From basic research to clinical practice. Herz 2003;28:628-38.
36. Harrison D, Griendling KK, Landmesser U, Hornig B, Drexler H. Role of oxidative stress in atherosclerosis. The American journal of cardiology 2003;91:7A-11A.
37. Madamanchi NR, Vendrov A, Runge MS. Oxidative stress and vascular disease. Arteriosclerosis, thrombosis, and vascular biology 2005;25:29-38.
38. Hinagata J, Kakutani M, Fujii T et al. Oxidized LDL receptor LOX-1 is involved in neointimal hyperplasia after balloon arterial injury in a rat model. Cardiovascular research 2006;69:263-71.
39. Wagenaar DJ, Weissleder R, Hengerer A. Glossary of molecular imaging terminology. Academic radiology 2001;8:409-20.
40. Weissleder R, Mahmood U. Molecular imaging. Radiology 2001;219:316-33.
41. Blasberg RG, Tjuvajev JG. Molecular-genetic imaging: current and future perspectives. The Journal of clinical investigation 2003;111:1620-9.
42. Lucignani G, Jereczek-Fossa BA, Orecchia R. The role of molecular imaging in precision radiation therapy for target definition, treatment planning optimisation and quality control. European journal of nuclear medicine and molecular imaging 2004;31:1059-63.

43. Nahrendorf M, Weissleder R. [Advances in cardiovascular medicine through molecular imaging]. Der Radiologe 2007;47:18-24.
44. Ransohoff KJ, Wu JC. Advances in cardiovascular molecular imaging for tracking stem cell therapy. Thrombosis and haemostasis 2010;104:13-22.
45. Phinikaridou A, Andia ME, Shah AM, Botnar RM. Advances in molecular imaging of atherosclerosis and myocardial infarction: shedding new light on in vivo cardiovascular biology. American journal of physiology Heart and circulatory physiology 2012;303:H1397-410.
46. Davies MJ, Gordon JL, Gearing AJ et al. The expression of the adhesion molecules ICAM-1, VCAM-1, PECAM, and E-selectin in human atherosclerosis. The Journal of pathology 1993;171:223-9.
47. Kerwin W, Hooker A, Spilker M et al. Quantitative magnetic resonance imaging analysis of neovasculature volume in carotid atherosclerotic plaque. Circulation 2003;107:851-6.
48. Nahrendorf M, Jaffer FA, Kelly KA et al. Noninvasive vascular cell adhesion molecule-1 imaging identifies inflammatory activation of cells in atherosclerosis. Circulation 2006;114:1504-11.
49. Swirski FK, Libby P, Aikawa E et al. Ly-6Chi monocytes dominate hypercholesterolemia-associated monocytosis and give rise to macrophages in atheromata. The Journal of clinical investigation 2007;117:195-205.
50. Tsimikas S, Shaw PX. Non-invasive imaging of vulnerable plaques by molecular targeting of oxidized LDL with tagged oxidation-specific antibodies. Journal of cellular biochemistry Supplement 2002;39:138-46.
51. Torzewski M, Shaw PX, Han KR et al. Reduced in vivo aortic uptake of radiolabeled oxidation-specific antibodies reflects changes in plaque composition consistent with plaque stabilization. Arteriosclerosis, thrombosis, and vascular biology 2004;24:2307-12.
52. Briley-Saebo KC, Shaw PX, Mulder WJ et al. Targeted molecular probes for imaging atherosclerotic lesions with magnetic resonance using antibodies that recognize oxidation-specific epitopes. Circulation 2008;117:3206-15.
53. Rudd JH, Narula J, Strauss HW et al. Imaging atherosclerotic plaque inflammation by fluorodeoxyglucose with positron emission tomography: ready for prime time? Journal of the American College of Cardiology 2010;55:2527-35.
54. Rudd JH, Myers KS, Bansilal S et al. (18)Fluorodeoxyglucose positron emission tomography imaging of atherosclerotic plaque inflammation is highly reproducible: implications for atherosclerosis therapy trials. Journal of the American College of Cardiology 2007;50:892-6.

55. Rudd JH, Warburton EA, Fryer TD et al. Imaging atherosclerotic plaque inflammation with [18F]-fluorodeoxyglucose positron emission tomography. Circulation 2002;105:2708-11.
56. Majmudar MD, Keliher EJ, Heidt T et al. Monocyte-directed RNAi targeting CCR2 improves infarct healing in atherosclerosis-prone mice. Circulation 2013;127:2038-46.
57. Wu YW, Kao HL, Chen MF et al. Characterization of plaques using ^{18}F-FDG PET/CT in patients with carotid atherosclerosis and correlation with matrix metalloproteinase-1. Journal of nuclear medicine : official publication, Society of Nuclear Medicine 2007;48:227-33.
58. Li D, Liu L, Chen H, Sawamura T, Ranganathan S, Mehta JL. LOX-1 mediates oxidized low-density lipoprotein-induced expression of matrix metalloproteinases in human coronary artery endothelial cells. Circulation 2003;107:612-7.
59. Galis ZS, Sukhova GK, Lark MW, Libby P. Increased expression of matrix metalloproteinases and matrix degrading activity in vulnerable regions of human atherosclerotic plaques. The Journal of clinical investigation 1994;94:2493-503.
60. Zhang W, Li P, Yang F et al. Dynamic and reversible fluorescence imaging of superoxide anion fluctuations in live cells and in vivo. Journal of the American Chemical Society 2013;135:14956-9.
61. Laitinen I, Saraste A, Weidl E et al. Evaluation of alphavbeta3 integrin-targeted positron emission tomography tracer 18F-galacto-RGD for imaging of vascular inflammation in atherosclerotic mice. Circulation Cardiovascular imaging 2009;2:331-8.
62. Levin M, Bjornheden T, Evaldsson M, Walenta S, Wiklund O. A bioluminescence method for the mapping of local ATP concentrations within the arterial wall, with potential to assess the in vivo situation. Arteriosclerosis, thrombosis, and vascular biology 1999;19:950-8.
63. Leppanen O, Ekstrand M, Brasen JH, Levin M. Bioluminescence imaging of energy depletion in vascular pathology: patent ductus arteriosus and atherosclerosis. Journal of biophotonics 2012;5:336-44.
64. Terashima M, Ehara S, Yang E et al. In vivo bioluminescence imaging of inducible nitric oxide synthase gene expression in vascular inflammation. Molecular imaging and biology : MIB : the official publication of the Academy of Molecular Imaging 2011;13:1061-6.
65. Abdelhalim MA, Moussa SA, Al-Mohy YH. Ultraviolet-visible and fluorescence spectroscopy techniques are important diagnostic tools during the progression of atherosclerosis: diet zinc supplementation retarded or delayed atherosclerosis. BioMed research international 2013;2013:652604.

66. Thukkani AK, Jaffer FA. Intravascular near-infrared fluorescence molecular imaging of atherosclerosis. American journal of nuclear medicine and molecular imaging 2013;3:217-31.
67. Bruckman M, Jiang K, Simpson EJ et al. Dual-modal magnetic resonance and fluorescence imaging of atherosclerotic plaques in vivo using VCAM-1 targeted tobacco mosaic virus. Nano letters 2014.
68. Gessner R, Dayton PA. Advances in molecular imaging with ultrasound. Molecular imaging 2010;9:117-27.
69. Kiessling F, Fokong S, Bzyl J, Lederle W, Palmowski M, Lammers T. Recent advances in molecular, multimodal and theranostic ultrasound imaging. Advanced drug delivery reviews 2013.
70. Yan F, Li X, Jiang C et al. A novel microfluidic chip for assessing dynamic adhesion behavior of cell-targeting microbubbles. Ultrasound in medicine & biology 2014;40:148-57.
71. Yan F, Li X, Jin Q et al. Ultrasonic imaging of endothelial CD81 expression using CD81-targeted contrast agents in in vitro and in vivo studies. Ultrasound in medicine & biology 2012;38:670-80.
72. Yan F, Li X, Jin Q et al. Therapeutic ultrasonic microbubbles carrying paclitaxel and LyP-1 peptide: preparation, characterization and application to ultrasound-assisted chemotherapy in breast cancer cells. Ultrasound in medicine & biology 2011;37:768-79.
73. Li X, Jin Q, Chen T et al. LyP-1 ultrasonic microbubbles targeting to cancer cell as tumor bio-acoustics markers or drug carriers: targeting efficiency evaluation in, microfluidic channels. Conference proceedings : Annual International Conference of the IEEE Engineering in Medicine and Biology Society IEEE Engineering in Medicine and Biology Society Conference 2009;2009:463-6.
74. Lindner JR, Song J, Christiansen J, Klibanov AL, Xu F, Ley K. Ultrasound assessment of inflammation and renal tissue injury with microbubbles targeted to P-selectin. Circulation 2001;104:2107-12.
75. Zhao Y, Kuge Y, Zhao S, Strauss HW, Blankenberg FG, Tamaki N. Prolonged high-fat feeding enhances aortic 18F-FDG and 99mTc-annexin A5 uptake in apolipoprotein E-deficient and wild-type C57BL/6J mice. Journal of nuclear medicine : official publication, Society of Nuclear Medicine 2008;49:1707-14.
76. Leuschner F, Nahrendorf M. Molecular imaging of coronary atherosclerosis and myocardial infarction: considerations for the bench and perspectives for the clinic. Circulation research 2011;108:593-606.

77. Lee WW, Marinelli B, van der Laan AM et al. PET/MRI of inflammation in myocardial infarction. Journal of the American College of Cardiology 2012;59:153-63.
78. Okane K, Ibaraki M, Toyoshima H et al. 18F-FDG accumulation in atherosclerosis: use of CT and MR co-registration of thoracic and carotid arteries. European journal of nuclear medicine and molecular imaging 2006;33:589-94.
79. Tawakol A, Migrino RQ, Bashian GG et al. In vivo 18F-fluorodeoxyglucose positron emission tomography imaging provides a noninvasive measure of carotid plaque inflammation in patients. Journal of the American College of Cardiology 2006;48:1818-24.
80. Bural GG, Torigian DA, Chamroonrat W et al. 18F-FDG-PET is an effective imaging modality to detect and quantify age-related atherosclerosis in large arteries. European journal of nuclear medicine and molecular imaging 2008;35:562-9.
81. Paulmier B, Duet M, Khayat R et al. Arterial wall uptake of fluorodeoxyglucose on PET imaging in stable cancer disease patients indicates higher risk for cardiovascular events. Journal of nuclear cardiology : official publication of the American Society of Nuclear Cardiology 2008;15:209-17.
82. Rudd JH, Myers KS, Bansilal S et al. Atherosclerosis inflammation imaging with 18F-FDG PET: carotid, iliac, and femoral uptake reproducibility, quantification methods, and recommendations. Journal of nuclear medicine : official publication, Society of Nuclear Medicine 2008;49:871-8.
83. Chen W, Bural GG, Torigian DA, Rader DJ, Alavi A. Emerging role of 18F-FDG-PET/CT in assessing atherosclerosis in large arteries. European journal of nuclear medicine and molecular imaging 2009;36:144-51.
84. Rominger A, Saam T, Wolpers S et al. 18F-FDG PET/CT identifies patients at risk for future vascular events in an otherwise asymptomatic cohort with neoplastic disease. Journal of nuclear medicine : official publication, Society of Nuclear Medicine 2009;50:1611-20.
85. Wasselius JA, Larsson SA, Jacobsson H. 18F-FDG-accumulating atherosclerotic plaques identified with 18F-FDG-PET/CT in 141 patients. Molecular imaging and biology : MIB : the official publication of the Academy of Molecular Imaging 2009;11:455-9.
86. Wykrzykowska J, Lehman S, Williams G et al. Imaging of inflamed and vulnerable plaque in coronary arteries with 18F-FDG PET/CT in patients with suppression of myocardial uptake using a low-carbohydrate, high-fat preparation. Journal of nuclear medicine : official publication, Society of Nuclear Medicine 2009;50:563-8.

87. Forster S, Rominger A, Saam T et al. 18F-fluoroethylcholine uptake in arterial vessel walls and cardiovascular risk factors: correlation in a PET-CT study. Nuklearmedizin Nuclear medicine 2010;49:148-53.
88. Leppanen O, Bjornheden T, Evaldsson M, Boren J, Wiklund O, Levin M. ATP depletion in macrophages in the core of advanced rabbit atherosclerotic plaques in vivo. Atherosclerosis 2006;188:323-30.
89. Sluimer JC, Daemen MJ. Novel concepts in atherogenesis: angiogenesis and hypoxia in atherosclerosis. The Journal of pathology 2009;218:7-29.
90. Newsholme P, Curi R, Gordon S, Newsholme EA. Metabolism of glucose, glutamine, long-chain fatty acids and ketone bodies by murine macrophages. The Biochemical journal 1986;239:121-5.
91. Deichen JT, Prante O, Gack M, Schmiedehausen K, Kuwert T. Uptake of [18F]fluorodeoxyglucose in human monocyte-macrophages in vitro. European journal of nuclear medicine and molecular imaging 2003;30:267-73.
92. Taneja N, Coy PE, Lee I, Bryson JM, Robey RB. Proinflammatory interleukin-1 cytokines increase mesangial cell hexokinase activity and hexokinase II isoform abundance. American journal of physiology Cell physiology 2004;287:C548-57.
93. Mamede M, Higashi T, Kitaichi M et al. [18F]18F-FDG uptake and PCNA, Glut-1, and Hexokinase-II expressions in cancers and inflammatory lesions of the lung. Neoplasia 2005;7:369-79.
94. Maschauer S, Prante O, Hoffmann M, Deichen JT, Kuwert T. Characterization of 18F-FDG uptake in human endothelial cells in vitro. Journal of nuclear medicine : official publication, Society of Nuclear Medicine 2004;45:455-60.
95. Silvola JM, Saraste A, Laitinen I et al. Effects of age, diet, and type 2 diabetes on the development and 18F-FDG uptake of atherosclerotic plaques. JACC Cardiovascular imaging 2011;4:1294-301.
96. Zhao S, Kuge Y, Tsukamoto E et al. Fluorodeoxyglucose uptake and glucose transporter expression in experimental inflammatory lesions and malignant tumours: effects of insulin and glucose loading. Nuclear medicine communications 2002;23:545-50.
97. Zhuang HM, Cortes-Blanco A, Pourdehnad M et al. Do high glucose levels have differential effect on 18F-FDG uptake in inflammatory and malignant disorders? Nuclear medicine communications 2001;22:1123-8.
98. Tawakol A, Migrino RQ, Hoffmann U et al. Noninvasive in vivo measurement of vascular inflammation with F-18 fluorodeoxyglucose positron emission tomography. Journal of nuclear cardiology : official publication of the American Society of Nuclear Cardiology 2005;12:294-301.

99. Laitinen I, Marjamaki P, Haaparanta M et al. Non-specific binding of [18F]18F-FDG to calcifications in atherosclerotic plaques: experimental study of mouse and human arteries. European journal of nuclear medicine and molecular imaging 2006;33:1461-7.
100. Matter CM, Wyss MT, Meier P et al. 18F-choline images murine atherosclerotic plaques ex vivo. Arteriosclerosis, thrombosis, and vascular biology 2006;26:584-9.
101. Ivan E, Khatri JJ, Johnson C et al. Expansive arterial remodeling is associated with increased neointimal macrophage foam cell content: the murine model of macrophage-rich carotid artery lesions. Circulation 2002;105:2686-91.
102. Davies JR, Rudd JH, Fryer TD et al. Identification of culprit lesions after transient ischemic attack by combined 18F fluorodeoxyglucose positron-emission tomography and high-resolution magnetic resonance imaging. Stroke; a journal of cerebral circulation 2005;36:2642-7.
103. Dunphy MP, Schoder H, Strauss HW. Radionuclide techniques for identifying vulnerable plaque. Journal of nuclear medicine : official publication, Society of Nuclear Medicine 2007;48:1753-5.
104. Basu S, Zhuang H, Alavi A. Imaging of lower extremity artery atherosclerosis in diabetic foot: 18F-FDG-PET imaging and histopathological correlates. Clinical nuclear medicine 2007;32:567-8.
105. Dunphy MP, Freiman A, Larson SM, Strauss HW. Association of vascular 18F-FDG uptake with vascular calcification. Journal of nuclear medicine : official publication, Society of Nuclear Medicine 2005;46:1278-84.
106. Alexanderson E, Slomka P, Cheng V et al. Fusion of positron emission tomography and coronary computed tomographic angiography identifies fluorine 18 fluorodeoxyglucose uptake in the left main coronary artery soft plaque. Journal of nuclear cardiology : official publication of the American Society of Nuclear Cardiology 2008;15:841-3.
107. Williams G, Kolodny GM. Retrospective study of coronary uptake of 18F-fluorodeoxyglucose in association with calcification and coronary artery disease: a preliminary study. Nuclear medicine communications 2009;30:287-91.
108. Fox JJ, Strauss HW. One step closer to imaging vulnerable plaque in the coronary arteries. Journal of nuclear medicine : official publication, Society of Nuclear Medicine 2009;50:497-500.
109. Haug AR, Cindea-Drimus R, Auernhammer CJ et al. Neuroendocrine tumor recurrence: diagnosis with 68Ga-DOTATATE PET/CT. Radiology 2014;270:517-25.
110. Sansovini M, Severi S, Ambrosetti A et al. Treatment with the radiolabelled somatostatin analog Lu-DOTATATE for advanced pancreatic neuroendocrine tumors. Neuroendocrinology 2013;97:347-54.

111. Jois B, Asopa R, Basu S. Somatostatin receptor imaging in non-(131)I-avid metastatic differentiated thyroid carcinoma for determining the feasibility of peptide receptor radionuclide therapy with (177)Lu-DOTATATE: low fraction of patients suitable for peptide receptor radionuclide therapy and evidence of chromogranin A level-positive neuroendocrine differentiation. Clinical nuclear medicine 2014;39:505-10.
112. Krantic S. Peptides as regulators of the immune system: emphasis on somatostatin. Peptides 2000;21:1941-64.
113. Dalm VA, van Hagen PM, van Koetsveld PM et al. Expression of somatostatin, cortistatin, and somatostatin receptors in human monocytes, macrophages, and dendritic cells. American journal of physiology Endocrinology and metabolism 2003;285:E344-53.
114. Armani C, Catalani E, Balbarini A, Bagnoli P, Cervia D. Expression, pharmacology, and functional role of somatostatin receptor subtypes 1 and 2 in human macrophages. Journal of leukocyte biology 2007;81:845-55.
115. Rominger A, Saam T, Vogl E et al. In vivo imaging of macrophage activity in the coronary arteries using 68Ga-DOTATATE PET/CT: correlation with coronary calcium burden and risk factors. Journal of nuclear medicine : official publication, Society of Nuclear Medicine 2010;51:193-7.
116. Schatka I, Wollenweber T, Haense C, Brunz F, Gratz KF, Bengel FM. Peptide receptor-targeted radionuclide therapy alters inflammation in atherosclerotic plaques. Journal of the American College of Cardiology 2013;62:2344-5.
117. Galkina E, Ley K. Vascular adhesion molecules in atherosclerosis. Arteriosclerosis, thrombosis, and vascular biology 2007;27:2292-301.
118. Somers WS, Tang J, Shaw GD, Camphausen RT. Insights into the molecular basis of leukocyte tethering and rolling revealed by structures of P- and E-selectin bound to SLe(X) and PSGL-1. Cell 2000;103:467-79.
119. Frenette PS, Denis CV, Weiss L et al. P-Selectin glycoprotein ligand 1 (PSGL-1) is expressed on platelets and can mediate platelet-endothelial interactions in vivo. The Journal of experimental medicine 2000;191:1413-22.
120. Furie B, Furie BC. Role of platelet P-selectin and microparticle PSGL-1 in thrombus formation. Trends in molecular medicine 2004;10:171-8.
121. Johnson-Tidey RR, McGregor JL, Taylor PR, Poston RN. Increase in the adhesion molecule P-selectin in endothelium overlying atherosclerotic plaques. Coexpression with intercellular adhesion molecule-1. The American journal of pathology 1994;144:952-61.

122. Jacobin-Valat MJ, Deramchia K, Mornet S et al. MRI of inducible P-selectin expression in human activated platelets involved in the early stages of atherosclerosis. NMR in biomedicine 2011;24:413-24.
123. Varki A. Selectin ligands. Proceedings of the National Academy of Sciences of the United States of America 1994;91:7390-7.
124. Bachelet L, Bertholon I, Lavigne D et al. Affinity of low molecular weight fucoidan for P-selectin triggers its binding to activated human platelets. Biochimica et biophysica acta 2009;1790:141-6.
125. Rahmim A, Zaidi H. PET versus SPECT: strengths, limitations and challenges. Nuclear medicine communications 2008;29:193-207.
126. Ben-Haim S, Kupzov E, Tamir A, Israel O. Evaluation of 18F-FDG uptake and arterial wall calcifications using 18F-FDG PET/CT. Journal of nuclear medicine : official publication, Society of Nuclear Medicine 2004;45:1816-21.
127. Li X, Bauer W, Kreissl MC et al. Specific somatostatin receptor II expression in arterial plaque: (68)Ga-DOTATATE autoradiographic, immunohistochemical and flow cytometric studies in apoE-deficient mice. Atherosclerosis 2013;230:33-9.
128. Nakashima Y, Plump AS, Raines EW, Breslow JL, Ross R. ApoE-deficient mice develop lesions of all phases of atherosclerosis throughout the arterial tree. Arteriosclerosis and thrombosis : a journal of vascular biology / American Heart Association 1994;14:133-40.
129. Herold V, Wellen J, Ziener CH et al. In vivo comparison of atherosclerotic plaque progression with vessel wall strain and blood flow velocity in apoE(-/-) mice with MR microscopy at 17.6 T. MAGMA 2009;22:159-66.
130. Li X, Samnick S, Lapa C et al. 68Ga-DOTATATE PET/CT for the detection of inflammation of large arteries: correlation with18F-FDG, calcium burden and risk factors. EJNMMI research 2012;2:52.
131. Bruley-Rosset M, Florentin I, Mathe G. In vivo and in vitro macrophage activation by systemic adjuvants. Agents and actions 1976;6:251-5.
132. Yan S, Li M, Chai H et al. TNF-alpha decreases expression of somatostatin, somatostatin receptors, and cortistatin in human coronary endothelial cells. The Journal of surgical research 2005;123:294-301.
133. Fuster V, Badimon JJ. Regression or stabilization of atherosclerosis means regression or stabilization of what we don't see in the arteriogram. European heart journal 1995;16 Suppl E:6-12.
134. Mann JM, Davies MJ. Vulnerable plaque. Relation of characteristics to degree of stenosis in human coronary arteries. Circulation 1996;94:928-31.

135. Revelle BM, Scott D, Kogan TP, Zheng J, Beck PJ. Structure-function analysis of P-selectin-sialyl LewisX binding interactions. Mutagenic alteration of ligand binding specificity. The Journal of biological chemistry 1996;271:4289-97.
136. Leung K. Sialy Lewisx mimetic conjugated to ultrasmall superparamagnetic iron oxide nanoparticles. Molecular Imaging and Contrast Agent Database (MICAD). Bethesda (MD), 2004.
137. Rouzet F, Bachelet-Violette L, Alsac JM et al. Radiolabeled fucoidan as a p-selectin targeting agent for in vivo imaging of platelet-rich thrombus and endothelial activation. Journal of nuclear medicine : official publication, Society of Nuclear Medicine 2011;52:1433-40.
138. Schafers M, Riemann B, Kopka K et al. Scintigraphic imaging of matrix metalloproteinase activity in the arterial wall in vivo. Circulation 2004;109:2554-9.
139. Fujimoto S, Hartung D, Ohshima S et al. Molecular imaging of matrix metalloproteinase in atherosclerotic lesions: resolution with dietary modification and statin therapy. Journal of the American College of Cardiology 2008;52:1847-57.
140. Gotsch U, Jager U, Dominis M, Vestweber D. Expression of P-selectin on endothelial cells is upregulated by LPS and TNF-alpha in vivo. Cell adhesion and communication 1994;2:7-14.
141. Nahrendorf M, Keliher E, Panizzi P et al. 18F-4V for PET-CT imaging of VCAM-1 expression in atherosclerosis. JACC Cardiovascular imaging 2009;2:1213-22.
142. Cumashi A, Ushakova NA, Preobrazhenskaya ME et al. A comparative study of the anti-inflammatory, anticoagulant, antiangiogenic, and antiadhesive activities of nine different fucoidans from brown seaweeds. Glycobiology 2007;17:541-52.
143. Fitton JH. Therapies from fucoidan; multifunctional marine polymers. Marine drugs 2011;9:1731-60.
144. Stary HC, Chandler AB, Dinsmore RE et al. A definition of advanced types of atherosclerotic lesions and a histological classification of atherosclerosis. A report from the Committee on Vascular Lesions of the Council on Arteriosclerosis, American Heart Association. Arteriosclerosis, thrombosis, and vascular biology 1995;15:1512-31.
145. Lutgens E, van Suylen RJ, Faber BC et al. Atherosclerotic plaque rupture: local or systemic process? Arteriosclerosis, thrombosis, and vascular biology 2003;23:2123-30.
146. Blann AD, Nadar SK, Lip GY. The adhesion molecule P-selectin and cardiovascular disease. European heart journal 2003;24:2166-79.
147. Downing LJ, Wakefield TW, Strieter RM et al. Anti-P-selectin antibody decreases inflammation and thrombus formation in venous thrombosis. Journal of vascular surgery : official publication, the Society for Vascular Surgery [and] International

Society for Cardiovascular Surgery, North American Chapter 1997;25:816-27; discussion 828.

148. Yokoyama S, Ikeda H, Haramaki N, Yasukawa H, Murohara T, Imaizumi T. Platelet P-selectin plays an important role in arterial thrombogenesis by forming large stable platelet-leukocyte aggregates. Journal of the American College of Cardiology 2005;45:1280-6.
149. Saam T, Rominger A, Wolpers S et al. Association of inflammation of the left anterior descending coronary artery with cardiovascular risk factors, plaque burden and pericardial fat volume: a PET/CT study. European journal of nuclear medicine and molecular imaging 2010;37:1203-12.
150. Rudd JHF. Imaging Atherosclerotic Plaque Inflammation With [18F]-Fluorodeoxyglucose Positron Emission Tomography. Circulation 2002;105:2708-2711.
151. Yun M, Jang S, Cucchiara A, Newberg AB, Alavi A. 18F 18F-FDG uptake in the large arteries: a correlation study with the atherogenic risk factors. Seminars in nuclear medicine 2002;32:70-6.
152. Yun M, Yeh D, Araujo LI, Jang S, Newberg A, Alavi A. F-18 18F-FDG uptake in the large arteries: a new observation. Clinical nuclear medicine 2001;26:314-9.
153. McCarthy MJ, Loftus IM, Thompson MM et al. Angiogenesis and the atherosclerotic carotid plaque: an association between symptomatology and plaque morphology. Journal of vascular surgery : official publication, the Society for Vascular Surgery [and] International Society for Cardiovascular Surgery, North American Chapter 1999;30:261-8.
154. Mofidi R, Crotty TB, McCarthy P, Sheehan SJ, Mehigan D, Keaveny TV. Association between plaque instability, angiogenesis and symptomatic carotid occlusive disease. The British journal of surgery 2001;88:945-50.
155. Ma J, Liu R, Peng H, Zhou J, Li H. CD81 inhibits the proliferation of astrocytes by inducing G(0)/G (1) arrest in vitro. Journal of Huazhong University of Science and Technology Medical sciences = Hua zhong ke ji da xue xue bao Yi xue Ying De wen ban = Huazhong keji daxue xuebao Yixue Yingdewen ban 2010;30:201-5.
156. Boismenu R, Rhein M, Fischer WH, Havran WL. A role for CD81 in early T cell development. Science 1996;271:198-200.
157. Levy S, Todd SC, Maecker HT. CD81 (TAPA-1): a molecule involved in signal transduction and cell adhesion in the immune system. Annual review of immunology 1998;16:89-109.
158. Chambrion C, Le Naour F. The tetraspanins CD9 and CD81 regulate CD9P1-induced effects on cell migration. PloS one 2010;5:e11219.

159. Yanez-Mo M, Alfranca A, Cabanas C et al. Regulation of endothelial cell motility by complexes of tetraspan molecules CD81/TAPA-1 and CD151/PETA-3 with alpha3 beta1 integrin localized at endothelial lateral junctions. The Journal of cell biology 1998;141:791-804.
160. Rohlena J, Volger OL, van Buul JD et al. Endothelial CD81 is a marker of early human atherosclerotic plaques and facilitates monocyte adhesion. Cardiovascular research 2009;81:187-96.
161. Davies JR, Rudd JH, Weissberg PL. Molecular and metabolic imaging of atherosclerosis. Journal of nuclear medicine : official publication, Society of Nuclear Medicine 2004;45:1898-907.
162. Wang W, Wang S, Yan L et al. Superoxide production and reactive oxygen species signaling by endothelial nitric-oxide synthase. The Journal of biological chemistry 2000;275:16899-903.
163. Demos SM, Alkan-Onyuksel H, Kane BJ et al. In vivo targeting of acoustically reflective liposomes for intravascular and transvascular ultrasonic enhancement. Journal of the American College of Cardiology 1999;33:867-75.
164. Hamilton AJ, Huang SL, Warnick D et al. Intravascular ultrasound molecular imaging of atheroma components in vivo. Journal of the American College of Cardiology 2004;43:453-60.
165. McCarty OJ, Conley RB, Shentu W et al. Molecular imaging of activated von Willebrand factor to detect high-risk atherosclerotic phenotype. JACC Cardiovascular imaging 2010;3:947-55.
166. Leong-Poi H, Christiansen J, Klibanov AL, Kaul S, Lindner JR. Noninvasive assessment of angiogenesis by ultrasound and microbubbles targeted to alpha(v)-integrins. Circulation 2003;107:455-60.
167. Kheirolomoom A, Dayton PA, Lum AF et al. Acoustically-active microbubbles conjugated to liposomes: characterization of a proposed drug delivery vehicle. Journal of controlled release : official journal of the Controlled Release Society 2007;118:275-84.
168. Shinde Patil VR, Campbell CJ, Yun YH, Slack SM, Goetz DJ. Particle diameter influences adhesion under flow. Biophysical journal 2001;80:1733-43.
169. Higginbottom A, Quinn ER, Kuo CC et al. Identification of amino acid residues in CD81 critical for interaction with hepatitis C virus envelope glycoprotein E2. Journal of virology 2000;74:3642-9.
170. Petracca R, Falugi F, Galli G et al. Structure-function analysis of hepatitis C virus envelope-CD81 binding. Journal of virology 2000;74:4824-30.

171. Kitadokoro K, Bordo D, Galli G et al. CD81 extracellular domain 3D structure: insight into the tetraspanin superfamily structural motifs. The EMBO journal 2001;20:12-8.

9 APPENDIX

9.1 Abbreviation

Acute coronary syndrome (ACS)
Apolipoprotein E (ApoE-/-)
Bioluminescence imaging (BLI)
Cardiovascular disease (CVD)
Cell adhesion molecule (CAM)
Computed tomography (CT)
C-reactive protein (CRP)
DOTA-(Tyr3)-octreotate (DOTATATE)
Fluorescence imaging (FI)
Fluorescence reflectance imaging (FRI)
Fluorescence molecular tomography (FMT)
Fluorodeoxyglucose (FDG)
Interleukin (IL)
Intercellular adhesion molecule 1 (ICAM-1)
Lipopolysaccharide (LPS)
Low-density lipoprotein (LDL)
Magnetic resonance imaging (MRI)
Molecular imaging (MI)
Monocyte chemo attractant protein (MCP-1)
Neuroendocrine tumor (NET)
Optical imaging (OI)
Phenazine methosulfate (PMS)
Positron emission tomography (PET)
Reactive oxygen species (ROS)
Single photon emission computed tomography (SPECT)
Somatostatin receptor (SSTR)
Scavenger receptor A (SRA)
Superparamagnetic iron oxide (SPIO)
Target-to-background ratio (TBR)
Tumor necrosis factor alpha (TNF-α),
Ultrasmall superparamagnetic iron oxide (USPIO)
Vascular cell adhesion molecule 1 (VCAM-1)
Vascular endothelial growth factor (VEGF)

9.2 Acknowledgement

First, I want to thank my supervisors Prof. Wolfgang Bauer and Prof. Samuel Samnick for giving me the chance to accomplish my PhD thesis in the laboratory for Experimental Nuclear Medicine. Your motivation and valuable suggestions groomed me into a researcher with good scientific skills. To be the part of your laboratory was a wonderful experience, which was a remarkable moment in my life. Thank you for keeping faith and trust in me. Your unconditional and unlimited support helped me in finishing my project successfully.

Secondly, I want to thank my other two supervisors Prof. Peter Jakob and and Prof. Andreas Buck whose input helped my project to be in flow. Their diverse and intense knowledge helped me to lay the foundation of my study. And also, their inputs helped me to shape my project from elementary stage till last stage of my thesis submission.

Thirdly, I want to thank my colleagues and friends Dr. Ina Israel, Dr. Michael Kreissl, Mrs Elisabeth Bauer, Dominik Richter, Dr. Volker Herold, who motivated me all the time and taught me about German culture and traditions. I want to say thanks a lot all those social gathering in which you all invited me. It was a wonderful experience to be part of the gossips teasing each other and pulling legs. I am specifically thankful to Dr. Michael. Kreissl and Elisabeth Bauer, who helped me with the experiment design. Furthermore, I would also like to thank Ina Israel, Johannes Weirather, Dominik Richter, without their friendship I would not have enjoyed the time in Wuerzburg.

My greatest gratitude is going to my family, especially to my wife, not only give me the best present, our baby Theresa, but also supporting, encouraging me the entire time. Also my mother and father, you always believe me. I’m so proud of being your son.

Finally, I want to thank all staffs of the department of nuclear medicine, and the comprehensive heart failure center.

9.3 Affidavit

I hereby confirm that my thesis entitled " Molecular imaging of inflammation in atherosclerosis: Preclinical study in Apolipoprotein E-Deficient Mice and preliminary evaluation in human using positron emission tomography" is the results of my own work. I did not receive any help or support from commercial consultants. All sources and/or materials applied are listed and specified in the thesis.

Furthermore, I confirm that this thesis has not been submitted as part of another examination process neither in identical nor in similar form.

Würzburg, August 2014 _____

Eidesstattliche Erklärung

Hiermit erkläre ich an Eides statt, die Dissertation "Molekulare Bildgebung inflammatorischer Prozesse bei Atherosklerose: Präklinische Studie in Apolipoprotein-E Knockout-Mäusen sowie erste Evaluation humaner PET-Studien." eigenständig, d.h. insbesondere selbständig und ohne Hilfe eines kommerziellen Promotionsberaters, angefertigt und keine anderen als die von mir angegebenen Quellen und Hilfsmittel verwendet zu haben.

Ich erkläre außerdem, dass die Dissertation weder in gleicher noch in ähnlicher Form bereits in einem anderen Prüfungsverfahren vorgelegen hat.

Würzburg, August 2014 _____

9.4 Publications list

- **Li X, Bauer W, Israel I, et al. Targeting P-selectin by Gallium-68 labelled Fucoidan PET for non-invasive characterization of vulnerable plaques: Correlation with in vivo 17.6T MRI. Arterioscler Thromb Vasc Biol. 2014, 34(8):1661-1667.**
- **Li X, Bauer W, Kreissl MC et al. Specific somatostatin receptor II expression in arterial plaque: (68)Ga-DOTATATE autoradiographic, immunohistochemical and flow cytometric studies in apoE-deficient mice. Atherosclerosis. 2013 , 230(1):33-39.**
- **Li X, Samnick S, Lapa C, et al. 68Ga-DOTATATE PET/CT for the detection of inflammation of large arteries: correlation with 18F-FDG, calcium burden and risk factors. EJNMMI research, 2012, 2(1): 1-10.**
- **Li X, Jin Q, Chen T, et al. LyP-1 ultrasonic microbubbles targeting to cancer cell as tumor bio-acoustics markers or drug carriers: targeting efficiency evaluation in, microfluidic channels. Conf Proc IEEE Eng Med Biol Soc ; 2009: 463-466 .**
- **Yan F, Li X, Jiang C, et al. "A Novel Microfluidic Chip for Assessing Dynamic Adhesion Behavior of Cell-Targeting Microbubbles" Ultrasound Med Biol. 2014; 40(1):148-157.**
- **Yan F, Li X, Jin QF, et al. "Ultrasonic imaging of endothelial CD81 expression using CD81-targeted contrast agents in in vitro and in vivo studies." Ultrasound Med Biol. 2012; 28(4): 670-680.**
- **Yan F, Li X, Jin QF, et al "Therapeutic Ultrasound Microbubbles Carrying Paclitaxel and LyP-1 Peptide: Preparation, Characterization and Application to Ultrasonic Assisted Chemotherapy in Breast Cancer Cells". Ultrasound Med Biol, 2011; 37(5): 768-779 .**
- **Jiang CX, Li X, Yan F, et al. Microfluidic-assisted formation of multifunctional monodisperse microbubbles for diagnostics and therapeutics. Micro & Nano Letters, 2011; 6(6): 417–421.**

9.5 Curriculum Vitae

Xiang Li

Department of nuclear medicine,
Comprehensive heart failure center
University Hospital of Wuerzburg
Oberduerrbacher str. 6
97080 Wuerzburg,
Germany.
Phone: +49-017691448058, +49-931-201 35020
Email: E_Li_X@ukw.de

EDUCATION

Currently pursuing Doctoral ship (PhD.)

March.2011 - Now
Major: Nuclear Medicine
Nuclear Medicine Department
Comprehensive Heart Failure Center
Graduate School of Life Science
University Hospital of Wuerzburg, Germany

Masters of Science (Msc.)

September.2011 - May.2014
Major: Biomedical Engineering, Medical Imaging
Medical School
The Chinese University of Hong Kong
Hong Kong, China

Bachelors of Science (Bsc.)

September.2004 - July.2007
Major: Biomedical Science, Biochemistry and Biotechnology
Department of Life Science
University of Zhengzhou
Zhengzhou, China

PROFESSIONAL EXPERIENCES

- PhD, Wuerzburg University, Nuclear Medicine Department & Comprehensive Heart Failure Center.
  - Cardiovascular nuclear medical imaging (MicroPET, PET/CT, autoradiography)
  - High-resolution MRI

- Assistant researcher, Paul .C. Lauterbur Research Centre for Biomedical Imaging, Chinese Academic of Science. (5.2009-1.2011)
  - Specialize in development of in vivo molecular imaging technologies (3 T human MRI and High resolution animal ultrasound)
  - Animal modeling with tumor
  - Target Contrast Agent Design and fabrication (Microbubble and Superparamagnetic Iron Oxide_SPIO)
  - Pathology of cancer, atherosclerosis and relevant specific molecular probe investigation

- Master studies, Medical school & Department of engineering
  - Bio-MEMS application on assessment of imaging tracer
  - Molecular imaging techniques, especially on design and fabrication microbubble and USPIO for ultrasound and MR molecular imaging
  - Drug delivery, and multi-functional imaging contrast agents base on targeted microbubble and focal ultrasound transducer strategy

- Bachelor research internship, Medical school of Zhengzhou university
  - Cell culture
  - Tumor targeted therapy

GRANT PROGRAM

- National 973 Basic Research Program of China (No.2010CB732600) (Fundamental research of high-resolution imaging of cardiovascular and cerebral vascular vulnerable plague and risk assessment warning system) (Core Member).
- National Nature Science Foundation of China (No. 10904094) (Fundamental research of sensitive ultrasound molecular imaging) (Core Member)
- Bundes ministerium for fildung and Forschung (BMBF01EO1004)
- Sonderforschungsbereich 688: Molecular and functional imaging of cardiovascular cell-cell interactions. (Z2 & B5 project)

RESEARCH SKILLS

- ***Imaging:*** Micro-PET, PET/CT, autoradiography, MRI, Ultrasound.
- ***Imaging tracer/contrast agents:*** Ultrasound contrast agent (Microbubble), MRI contrast agent (SPIO, USPIO) fabrication. And concept of design of radiotracer.
- ***Biotechnologies:*** PCR, RT-PCR, Western Blot, FACS, Cell/Tissue culture, Animal manipulation, cell biology.
- ***Animal handling:*** Animal surgery and modeling (tumor and cardiovascular disease)
- ***Bio-MEMS:*** Design and fabrication of Microfluidic chip.
- ***Statistical Packages:*** SPSS, STATS, CurveExpert1.3

ADDITIONAL INFORMATION

Nationality: China
Marital status: Married
Date of birth: July.7, 1984